ANALYSIS OF BIO-OPTICAL PROPERTIES IN ESTUARINE AND COASTAL WATERS - STUDY THROUGH IN-SITU AND REMOTE SENSING OBSERVATIONS

A THESIS SUBMITTED IN PARTIAL FULFILLMENT FOR THE DEGREE

OF

DOCTOR OF PHILOSOPHY

IN **MARINE SCIENCES**

IN THE SCHOOL OF EARTH, OCEAN AND ATMOSPHERIC SCIENCES

GOA UNIVERSITY

By

PARTHA A. PATIL

SCHOOL OF EARTH, OCEAN AND ATMOSPHERIC SCIENCES

Goa University

Taleigao Plateau - 403206, Goa, India

June 2025

DECLARATION

I, Partha A. Patil, hereby declare that this thesis represents work which has been carried out by me and that it has not been submitted, either in part or full, to any other University or Institution for the award of any research degree.

Place : Goa University, Goa, India
Date : Partha A. Patil

CERTIFICATE

I hereby certify that the above Declaration of the candidate, Partha A. Patil, is true, and the work was carried out under my supervision.

Professor (HAG) Harilal B. Menon
Research Supervisor
Goa University
Taleigao Plateau-403206, Goa, India.

Dedicated to my family

My mom, for her unwavering belief in me.
My sister, for her steadfast support.
My dad and my granddad, for nurturing my curiosity.

"The first principle is that you must not fool yourself
- and you are the easiest person to fool"

Richard Feynman

ACKNOWLEDGEMENTS

It is with deepest gratitude that I acknowledge the people who made this Ph.D. possible. First and foremost, I am deeply indebted to my supervising guide, Prof. (HAG) Harilal. B. Menon, for mentoring me with the utmost patience and kindness. His constant encouragement, insightful feedback and the opportunities facilitated have helped shape my critical thinking and sharpened my research ambitions. I shall always strive to emulate his ethos of working relentlessly for the betterment of society in my research career. His hard-working nature and big-picture thinking have set high standards for me regarding what it means to be a researcher and an educator.

I must also thank the esteemed members of the doctoral research committee, Dr. M. Ravichandran (Secretary, Ministry of Earth Sciences), Dr. Sanil Kumar (Chief Scientist, National Institute of Oceanography), Prof. V.M. Matta (Retired Professor, Goa University) and Dr. Anthony A.A. Viegas (Vice Dean of School of Earth, Oceans and Atmospheric Sciences, Goa University). Their invaluable comments and experienced perspectives provided during the review sessions have greatly enriched my research.

I am immensely grateful to the Department of Science and Technology for allowing me to be in their INSPIRE fellowship programme. I also wish to acknowledge the funding and support by the Naval Research Board (Defence Research and Development Organisation) and the Indian National Centre for Ocean Information Services in conducting the numerous field trips and research cruises in the estuarine and coastal waters along the west shore of India. The assistance provided by Mark Pinto, Nidhi Johri, Shruti Salgaonkar, Diksha Gaonkar, and Nupur Phadte, as well as the operational knowledge and manpower shared by the crew of the research vessels, was crucial for the proper scientific operations. I must also thank the technical and administrative staff of the School of Earth, Ocean and Atmospheric Sciences, Goa University, for their logistical assistance and the Vice Chancellor of Goa University for the instruments and facilities to conduct the research work. I am also grateful for the online public ocean data and satellite data product repositories maintained by the National Aeronautics and Space Administration of the United States of America and the European Space Agency.

I cherish the time spent in the laboratory in the company of Dr. Arjun Adhikari, Dr. Atiba Shaikh, and Dr. Avirup Sen. Their constant encouragement, timely discussions, and monumental help have strengthened my research aptitude and tenacity. Arjun has played an instrumental role in improving my science communication.

I will be eternally grateful to my close friends Jonathan Dias, Anil George, Garima Rathore, Abhyuday Sabharwal, Nandini Mehrotra, Nikhil Eapen, Julian Mathias, Divya Sahasrabuddhe, Aditya Prabhu, Mithila Bhat along with my nature explorers and friends from the various sports communities for their support, encouragement and for celebrating every small victory with me. A special mention to Ms. Janhavi Kangane for being with me every step of the way.

However, without my family, I would not have embarked on this venture, let alone complete it. My mom, Archana Patil, believed in my potential even in my lowest moment, and has enabled me to face the opportunities and challenges head-on. My dad Ashis Patil and my grand-dad Padmanath Patil have inculcated an inquisitive outlook to search for a deeper understanding of the world around me, which has become an instrumental aspect of my personality. My sister, Aishwarya, with her ever-supportive shoulder and practical advice, has propelled me a lot through the trials and tribulations of the PhD. I am grateful for their love and support and appreciate the sacrifices made for me to achieve my long-time goal.

Partha A. Patil

Abstract

Estuarine and coastal waters are characterised by highly variable and optically complex conditions resulting from spatially and temporally heterogeneous distributions of optically active constituents (OACs), notably phytoplankton pigments, total suspended matter (TSM), and chromophoric dissolved organic matter (CDOM). These aquatic environments, generally classified as Case II waters, challenge conventional remote sensing methodologies due to the non-linear and spectrally overlapping contributions of absorption and scattering processes governed by these constituents. This thesis presents a comprehensive investigation of the bio-optical dynamics of estuarine and coastal ecosystems through an integrative approach combining multi-seasonal *in-situ* radiometric, spectrophotometric, and remote sensing observations with satellite-derived ocean colour products. The research specifically emphasizes the quantification and remote sensing of CDOM and its implications for radiative transfer processes and coastal ecosystem functioning. A semi-analytical retrieval algorithm was developed for the robust estimation of CDOM absorption at 440 nm (a^{440}_{CDOM}) across diverse optical regimes by isolating the CDOM signal influencing the spectral reflectance and minimising the attenuation by the other OACs. The developed algorithm was of the form, $a^{440}_{cdom} = -0.01368x^2 + 0.102x + 0.02295$, with the three wavelength index given as $x = (\frac{1}{R^{412}_{rs}} - \frac{1}{R^{490}_{rs}}) \times R^{560}_{rs}$. This algorithm was formulated and validated using an extensive global dataset of *in-situ* measurements comprising absorption and attenuation coefficients, water-leaving radiance, and CDOM spectral slopes, acquired from estuarine and nearshore coastal zones. Comparative evaluation against widely adopted empirical and semi-analytical algorithms demonstrated superior performance of the proposed model, yielding the highest coefficient of determination ($r^2 = 0.64$) and the lowest error metrics ($rmse$ = 0.1039, mae = 0.064, $mape$ = 51.96%). Notably, its accuracy improved under conditions where CDOM exerted a dominant influence on the total absorption budget. The validation using satellite-derived data from MODIS-Aqua and Sentinel-3 OLCI further substantiated the algorithm's applicability across a spectrum of Case II waters.

Application of this algorithm facilitated, for the first time, the annual mapping of CDOM distribution in the Mandovi–Zuari Estuarine (MZE) system. The results captured seasonal plume dynamics during post-monsoonal discharge events and delineated zones of freshwater–seawater mixing. The analysis also revealed distinct shifts in CDOM source regimes from terrestrially derived material in the upper estuary to in-situ production in the mesohaline transition zone.

To elucidate the broader relevance of CDOM variability, this study analysed contrasting estuarine systems with differing CDOM influence, i.e., the MZE (India) and the Chesapeake–Delaware Bay system (USA). In the latter, the spatial gradients in retrieved CDOM highlighted riverine input from the Potomac, Rappahannock, York, and James Rivers, with downstream photobleaching and microbial degradation signatures evident along the salinity gradient. Additionally, CDOM enrichment zones associated with wetland-derived leachates were mapped, underlining the terrestrial-marine coupling in biogeochemical fluxes. A secondary objective of the thesis involved quantifying the influence of bio-optical complexity on radiative heating in the upper ocean. A bio-optical classification scheme was established for the eastern Arabian Sea using reflectance ratios ($R_{rs}^{412}/R_{rs}^{443}$ and $R_{rs}^{488}/R_{rs}^{547}$) to distinguish absorption- from scattering-dominated waters and to infer the dominant absorbing species (i.e., chlorophyll-a vs. CDOM/TSM). The resulting optical water types (O_1^T to O_4^T) revealed a gradient from optically clear offshore waters to highly complex nearshore regions proximal to river mouths. Radiant heating rate (RHR) analysis indicated a pronounced increase in surface heating with increasing bio-optical complexity. Although surface RHR varied significantly across optical types, vertically integrated heating within the euphotic layer remained relatively uniform. A targeted case study of water columns exhibiting identical net surface heat fluxes but divergent optical classifications demonstrated that differences in OAC composition and inherent optical properties (IOPs) can substantially modulate remote sensing reflectance and, consequently, vertical heat distribution. These findings suggest that bio-optical feedbacks may exert a first-order control on local air–sea interactions and should be integrated into coupled ocean–atmosphere models for improved regional climate projections.

In summary, this thesis delivers a novel methodological framework for remote sensing of CDOM in optically complex aquatic systems and advances the understanding of bio-optical variability in modulating radiative and biogeochemical processes. The developed tools and insights contribute to more accurate characterisation of estuarine–coastal exchanges, with significant implications for water quality monitoring, ecosystem modelling, and climate impact assessments.

LIST OF PUBLICATIONS

Published Manuscripts

1. Patil, P. A., Adhikari, A., & Menon, H. B. (2023). Bio-optical complexity and radiant heating rates in the coastal waters of eastern Arabian Sea. ***Science of the Total Environment***, 884, 163838.

2. Patil, P. A., Adhikari, A., & Menon, H. B. (2025). Analysis of seasonal distribution of chromophoric dissolved organic matter in turbid estuaries applying a novel semi-analytical algorithm. ***ISPRS Journal of Photogrammetry and Remote Sensing***, 229, 336-350.

LIST OF CONFERENCES

Conferences Attended

1. Patil, P. A., Adhikari, A., & Menon, H. B. (2021, August 12-14). *Spatio-temporal Variability of Bio-optical Properties and Radiant Heating Rate in the Eastern Arabian Sea*. [Poster Presentation]. 7th National Conference of the Ocean Society of India (OSICON-21), National Centre for Polar and Ocean Research (NCPOR - online), India.

2. Patil, P. A., Adhikari, A., & Menon, H. B. (2023, April 22-23). *Semi-Analytical Algorithm for the Estimation of Absorption by Chromophoric Dissolved Organic Matter in Estuarine and Coastal Waters*. [Poster Presentation]. National Conference on Scientific Advancement for Sustainable Environment, Herbal Medicines and Impact on Health: An Earth Day Celebration (SASE). Banaras Hindu University, Varanasi, India.

3. Patil, P. A., Adhikari, A., & Menon, H. B. (2023, August 23-25). *Monitoring River Plumes of Goa Using a Novel Algorithm for Estimating Chromophoric Dissolved Organic Matter in Estuarine and Coastal Waters*. [Oral Presentation]. 8th National Conference of the Ocean Society of India (OSICON-23), Indian National Centre for Ocean Information Services (INCOIS), Hyderabad, India.

4. Patil, P. A., Adhikari, A., & Menon, H. B. (2024, February 26-March 1). *An Improved Algorithm for the Space-based Estimation of Chromophoric Dissolved Organic Matter in Turbid Estuaries and Coastal Waters*. [Poster Presentation]. 22nd National Space Science Symposium (NSSS-2024), Goa University, Goa, India.

Contents

1 Introduction **1**

1.1 Coastal Bio-Optics and Remote Sensing 4
1.2 Rationale of Study 6
1.3 Objectives of Study 7
1.4 Scope of Study 7
1.5 Thesis Outline 8

2 Data and Methodology **9**

2.1 Description of Study Area 10
2.2 Instruments and measurement protocols 13
2.2.1 Radiometer 14
2.2.2 CTD 16
2.2.3 Water Sampling 16
2.3 Satellite Data Processing 20
2.3.1 Sentinel-3 OLCI 20
2.3.2 Aqua MODIS 21

3 A Novel Three-wavelength CDOM Retrieval Algorithm: Formulation and Global Validation **23**

3.1 Introduction 23
3.2 Data 28
3.2.1 Datasets 28
3.2.2 Statistical Analysis 30
3.3 Methodology 32
3.3.1 Theory and Conceptual Basis of the Algorithm 32
3.3.2 Conceptual Reasoning 32
3.3.3 Summary of Concept 33

3.3.4 Wavelength Selection for the Index . . . 34
3.3.5 Algorithm formulation . . . 36
3.3.6 Fine-Tuning of the Algorithm . . . 36
3.3.7 Existing widely used CDOM retrieval algorithms . . . 39
3.4 Results . . . 43
3.4.1 In-situ Validation of the Developed Algorithm Across Diverse Optical Conditions . . . 43
3.4.2 Comparison against Published Algorithms . . . 47
3.4.3 Validation of Satellite-Retrieved CDOM . . . 48
3.5 Discussion . . . 49
3.6 Conclusion . . . 53

4 Seasonal Distribution of CDOM in Turbid Estuarine and Coastal Waters: Applications of the Algorithm 55
4.1 Introduction . . . 55
4.2 Data and Methodology . . . 57
4.2.1 Site Description . . . 57
4.2.2 Satellite Data Processing . . . 59
4.3 Results . . . 61
4.3.1 Seasonal Spatial Distribution of Retrieved CDOM Values in the MZE . 61
4.3.2 Seasonal Spatial Distribution of Retrieved CDOM Values in the CDB . 63
4.4 Discussion . . . 70
4.4.1 Processes controlling CDOM distribution in MZE . . . 70
4.4.2 Processes controlling CDOM distribution in CDB . . . 72
4.5 Conclusion . . . 73

5 Bio-optical Complexity of Coastal Waters and their Effect on Radiant Heating Rates 75
5.1 Introduction . . . 75
5.2 Data and Methodology . . . 77
5.2.1 Study Area . . . 77
5.2.2 Additional IOP parameters: Source of CDOM and spectral particulate backscattering coefficient . . . 78
5.2.3 Bio-optical complexity classifaction . . . 79
5.2.4 Radiant Heating Rate and other atmospheric condition parameters . . . 80

5.2.5 Statistical analysis 81
5.3 Results 82
5.3.1 Optical Water Types and Spectral Remote Sensing Reflectance Variability 83
5.3.2 Comparison of Radiant Heating Rates 89
5.4 Discussion 94
5.4.1 Bio-optical Variability Across Water Types 94
5.4.2 Estimates of Radiant Heating Rate 95
5.4.3 Implications for the Net Heat Flux and Vertical Structure 95
5.4.4 Limitations and Future Directions 96
5.5 Conclusion 96

6 Conclusion **101**
6.1 Summary 101
6.2 Significance of the Study 103
6.3 Future Scope 103

Bibliography **122**

List of Abbreviations

Abbreviation	Expanded form
BR	Band-ratio
CDB	Chesapeake and Delaware Bays
CDOM	Chromophoric Dissolved Organic Matter
Chl-a	Chlorophyll-a
C2RCC	Case 2 Regional Coast Colour
CTD	Conductivity-Temperature-Depth
DMF	N, N-Dimethylformamide
EAS	Eastern Arabian Sea
ESA	European Space Agency
EUMETSAT	European Organisation for the Exploitation of Meteorological Satellites
GOCAD	Global Ocean Carbon Algorithm Database
GoM	Gulf of Mexico
IOCCG	International Ocean Colour Coordinating Group
IOPs	Inherent Optical Properties
ML	Machine Learning
MLR	Multiple Linear Regression
MODIS	Moderate Resolution Imaging Spectrometer
MZE	Mandovi and Zuari estuaries
NASA	National Aeronautics and Space Administration
NOMAD	NASA bio-Optical Marine Algorithm Dataset
OACs	Optically Active Constituents
OD	Optical Depth
OLCI	Ocean and Land Colour Instrument
ORV	Ocean Research Vessel

Abbreviation	Expanded form
PAR	Photosynthetically Active Radiation
QAA	Quasi-Analytical Algorithm
QAAv6	Quasi-Analytical Algorithm version 6
SAA	Semi-Analytical Algorithm
SNAP	Sentinel Application Platform
TSM	Total Suspended Matter (other than active Chl-a)

List of Symbols

Symbol	Description
λ	Wavelength [nm]
$a(\lambda)$	Absorption coefficient of water [m^{-1}]
$b(\lambda)$	Scattering coefficient of water [m^{-1}]
$c(\lambda)$	Attenuation coefficient of water [m^{-1}]
R_{rs}	Remote sensing reflectance [sr^{-1}]
O^T	Optical water type classification (1 to 4)
E_s	Surface-reaching irradiance [Wm^{-2}]
$E_s(\lambda)$	Spectral surface-reaching irradiance
$E_d^-(\lambda)$	Spectral downwelling irradiance just below surface
$E_d^+(\lambda)$	Spectral downwelling irradiance just above surface
L_u	Upwelling radiance
$L_u^-(\lambda)$	Spectral upwelling radiance just below surface
$L_w^+(\lambda)$	Spectral water leaving radiance
$E_u(\lambda)$	Spectral upwelling irradiance
$R_{rs}(\lambda)$	Spectral remote sensing reflectance
Q_0	Bidirectional reflectance factor
k_d	Diffuse attenuation coefficient of downwelling irradiance [m^{-1}]
α	Fresnel reflection albedo from sun and sky (typically 0.043)
ρ_f	Fresnel reflectance index of seawater (typically 0.021)
η_w	Fresnel refractive index of seawater (typically 1.345)
$a_{oac}(\lambda)$	Spectral absorption coefficient of each OAC [m^{-1}]
l	Length of the cuvette [m]
V	Volume of water sample filtered for spectrophotometric analysis [m^3]

Symbol	Description
A	Effective area of filter paper during spectrophotometric analysis [m^2]
c_{oac}	Concentration of OAC
a_{cdom}^{440}	Absorption coefficient of CDOM at 440 nm [m^{-1}]
$a_{cdom}^{440'}$	Spectrophotometrically estimated absorption coefficient of CDOM at 440 nm
S_g	Spectral slope of CDOM absorption curve
$a_{sw}(\lambda)$	Spectral absorption coefficient of seawater
$a_{chl}(\lambda)$	Spectral absorption coefficient of Chl-a
$a_{tsm}(\lambda)$	Spectral absorption coefficient of TSM
$a_{cdom}(\lambda)$	Spectral absorption coefficient of CDOM
$b_b(\lambda)$	Spectral total backscattering coefficient of water parcel
$b_{b_{sw}}(\lambda)$	Spectral backscattering coefficient of seawater
$b_{b_{chl}}(\lambda)$	Spectral backscattering coefficient of Chl-a
$b_{b_{tsm}}(\lambda)$	Spectral backscattering coefficient of TSM
a_{cdom}^{700}	Absorption coefficient of CDOM at 700 nm
c_{chl}	Concentration of Chl-a
c_{tsm}	Concentration of TSM
a_{chl}^{440}	Absorption coefficient of Chl-a at 440 nm
a_{tsm}^{440}	Absorption coefficient of TSM at 440 nm
n	Number of observations
r^2	Coefficient of determination
$rmse$	Root mean square error
$bias$	Statistical bias
mae	Mean absolute error
$mape$	Mean absolute percentage error
mpe	Mean percent error
y_{insitu}	In situ measurements
$y_{estimated}$	Model-driven estimates
$\overline{y_{insitu}}$	Mean in situ measurements
r	Pearson's correlation coefficient
k_d^{490}	Diffuse attenuation coefficient of downwelling irradiance at 490 nm
RHR	Radiant heating rate

Symbol	Description
k_d^{PAR}	Diffuse attenuation coefficient of downwelling irradiance over PAR
b_b^{650}	Total backscattering coefficient at 650 nm
$b_{b_p}^{650}$	Particulate backscattering coefficient at 650 nm
$b_{b_{sw}}^{650}$	Seawater backscattering coefficient at 650 nm
R_{rs}^{412}	Remote sensing reflectance at 412 nm
R_{rs}^{443}	Remote sensing reflectance at 443 nm
R_{rs}^{488}	Remote sensing reflectance at 488 nm
R_{rs}^{547}	Remote sensing reflectance at 547 nm
$a^{488} : a^{547}$	Total absorbance ratio at 488 nm against 547 nm
SI	Solar irradiance index
h_{ratio}	CDOM humification ratio
E_n	Spectrally integrated net irradiance (400-700 nm)
E_u	Spectrally integrated upwelling irradiance (400-700 nm)
E_d	Spectrally integrated downwelling irradiance (400–700 nm)
E_s	Spectrally integrated incoming solar irradiance (400–700 nm)
ρ	Seawater density
z	Depth
z_e	Euphotic depth
c_p	Specific heat capacity under constant pressure
E_s^{max}	Maximum spectrally integrated incoming solar irradiance in dataset
α_s	Sea-surface albedo
E_{ref}	Energy flux reflected back at the sea surface
E_{tr}	Energy flux transmitted into the water column
T_r	Transmittance of solar energy through the water column
Q^0	Net surface heat flux
Q^{lw}	Net longwave heat flux
Q^{sw}	Net shortwave heat flux
Q^s	Sensible heat flux
Q^l	Latent heat flux
$\int_0^2 k_d^{PAR}\, dz$	Vertically integrated diffuse attenuation coefficient of downwelling irradiance over PAR
$\int_0^2 RHR\, dz$	Surface integrated radiant heating

Symbol	Description
$\int_0^{z_e} RHR$	Mean integral heating of the water column till euphotic depth
λ_1	First wavelength of the CDOM index
λ_2	Second wavelength of the CDOM index
λ_3	Third wavelength of the CDOM index

List of Figures

1.1 The schematic representation of the estuarine and coastal environment, highlighting important processes attributed to the observed variability in optically active constituents. 3

2.1 Map of the coastal Eastern Arabian Sea indicating cruise station locations (purple circles). The inset image highlights the Mandovi and Zuari estuarine region, indicating the location of the field survey stations (orange circles) 12

2.2 (a) Hyperspectral radiometer. (b) Operations of the radiometer. 14

2.3 a) CTD Profiler. b) CTD profiling in operation 17

2.4 Niskin Sampler in operation. 17

2.5 Water filtration setup. 18

2.6 Spectrophotometer 19

3.1 The mean (solid) and maximum/minimum (dotted) spectral absorption of CDOM (yellow), Chl-a (green), TSM (red) and seawater molecules (blue) for the Mandovi and Zuari estuarine regions and the coastal waters of eastern Arabian Sea. 25

3.2 The results of the partial differential analysis for wavelength identification of the R_{rs} index. a) The histogram indicating the wavelength at which the maximum change in $\frac{\partial R_{rs}}{\partial a_{cdom}}$ was observed, b) the histogram indicating the wavelengths at which the cumulative absorption of Chl-a, TSM and seawater molecules showed a minimum difference against that at 400 nm. c) the scatter plot between the cumulative absorption of Chl-a, TSM and seawater molecules at λ_1 (400 nm) and λ_2 (465 nm) with the coefficient of determination (r^2) between them. d) & e) The histogram representing the wavelengths at which minimum variation to $\frac{\partial R_{rs}}{\partial a_{chl}}$ and $\frac{\partial R_{rs}}{\partial a_{tsm}}$ was observed. 37

3.3 The regression fit between in-situ a_{cdom}^{440} against the R_{rs} index, i.e., $\left(\frac{1}{R_{rs}^{400}} - \frac{1}{R_{rs}^{465}}\right) \times R_{rs}^{575}$ with statistical performance metrics. 38

3.4 The $rmse$ resulting from the iteration analysis for fine-tuning the index when a) λ_1, b) λ_2 and d) λ_3 are varied, respectively. c) The scatterplot between the cumulative absorption of Chl-a, TSM and seawater for fine-tuned λ_1 and λ_2 set at 412 nm and 490 nm, respectively. 39

3.5 Regression fit between in-situ a_{cdom}^{440} and the R_{rs} index $\left(\frac{1}{R_{rs}^{412}} - \frac{1}{R_{rs}^{490}}\right) \times R_{rs}^{560}$, along with statistical performance metrics. 40

3.6 The ternary plot depicting the contribution of each OAC to total absorption (absorption budget) at 440 nm for MZE (green circles), CDB (blue circles), GoM (yellow circles) and the other global data points (pink circles). 44

3.7 The scatter plot of simulated k_d^{490} from the sensitivity analysis conducted over varying OACs concentrations representative of the estuarine and coastal waters. The dotted line represents the average regression curve. 52

3.8 The partially differentiated modelled R_{rs} curves with respect to spectral a) a_{chl}, b) $b_{b_{chl}}$, c) a_{tsm} and d) $b_{b_{tsm}}$. 53

4.1 The map of Mandovi and Zuari estuarine waters with the dotted lines sectioning the estuaries. 58

4.2 The map of Chesapeake and Delaware Bays. 60

4.3 Composite monthly maps of retrieved a_{cdom}^{440} for the Mandovi and Zuari estuaries, derived from cloud-free OLCI scans during 2022-2023. Months shown are: a) September, b) October, c) November, d) December, e) January. 64

4.4 Composite monthly maps of retrieved a_{cdom}^{440} for the Mandovi and Zuari estuaries, derived from cloud-free OLCI scans during 2022-2023. Months shown are: a) February, b) March, c) April, d) May, and e) June. No cloud-free images were available for July and August. 65

4.5 Composite monthly maps of retrieved a_{cdom}^{440} for coastal waters of Goa, derived from cloud-free OLCI scans during 2022-2023. Months shown are: a) September, b) October, c) November, d) December, e) January, f) February, g) March, h) April, i) May, and j) June. No cloud-free images were available for July and August. 66

4.6 Composite monthly maps of retrieved a_{cdom}^{440} values for Chesapeake and Delaware Bays and adjacent coastal waters of the Mid-Atlantic Bight, derived from cloud-free OLCI scans during 2022-2023. Months shown are: a) March, b) April, c) May, and d) June. 67
4.7 Composite monthly maps of retrieved a_{cdom}^{440} values for Chesapeake and Delaware Bays and adjacent coastal waters of the Mid-Atlantic Bight, derived from cloud-free OLCI scans during 2022-2023. Months shown are: a) July, b) August, c) September, d) October. 68
4.8 Composite monthly maps of retrieved a_{cdom}^{440} values for Chesapeake and Delaware Bays and adjacent coastal waters of the Mid-Atlantic Bight, derived from cloud-free OLCI scans during 2022-2023. Months shown are: a) November, b) December, c) January, and d) February. 69

5.1 The map of EAS indicating the station location of each optical water types O_1^T, O_2^T, O_3^T and O_4^T 83
5.2 The boxplot depicting the depth distribution for each O^T 84
5.3 The mean spectral R_{rs} (solid line) along with their standard deviation (shaded area) for each O^T; a) O_1^T, b) O_2^T, c) O_3^T & d) O_4^T. 85
5.4 The ternary plots representing the contribution of each OAC in the absorption budget at 440 nm for each O^T; a) O_1^T, b) O_2^T, c) O_3^T & d) O_4^T. 86
5.5 The frequency distribution of the radiometer estimated $b_{b_p}^{650}$ for each O^T; a) O_1^T, b) O_2^T, c) O_3^T & d) O_4^T. 87
5.6 The mean particulate backscattering spectra modelled (solid line) and standard deviation (shaded area) for each O^T; a) O_1^T, b) O_2^T, c) O_3^T & d) O_4^T. 87
5.7 The vertical variability of mean (solid line) and best-fit curve (dotted line) of a) downwelling irradiance, b) particulate backscatter, c) diffuse attenuation coefficient of downwelling irradiance, d) transmission, and, e) RHR for the optical classification O_1^T (blue), O_2^T (red), O_3^T (magenta) & O_4^T (black). 93

List of Tables

3.1 The details of the combined dataset and its subsets used for the formulation and validation of the CDOM retrieval algorithm. 30
3.2 Stepwise computation of the Quasi-Analytical Algorithm (QAAv6) for deriving absorption and backscattering coefficients. 43
3.3 A comparison of the developed semi-analytical algorithm and other widely-used algorithms processed using in-situ data. The statistics in bold indicate the best performance of the parameter over the dataset. 46
3.4 A comparison of the developed semi-analytical algorithm and other widely used algorithms for OLCI and MODIS match-ups. The statistics in bold indicate the best performance of the parameter for the sensor. 50

5.1 Statistical summary (mean and standard deviation) of OACs and their associated parameters, classified according to the bio-optical complexity 89
5.2 Statistical summary (mean and standard deviation) of the solar irradiance index (SI), surface albedo (α_s), energy transfer through the surface layers and the subsequent RHR and coefficient of diffuse attenuation of downwelling irradiance for surface waters, categorised by optical water type. 91
5.3 Columnar radiant heating rates (RHR) and euphotic depths (z^e) for different optical water types (O_i^T). Values are expressed as mean $\pm$ standard deviation. . 92
5.4 A comparison with past literature studies detailing the bio-optical conditions of the water and their corresponding radiant heating rates (RHR). 98
5.5 A comparison between O^T, R_{rs} ratios, SI, surface RHR, T_r and ratio percentage of spectrally integrated (over 400-700 nm) specific absorption by CDOM, Chl-a, and TSM to the spectrally integrated cumulative specific absorption by all OAC and estimated backscattering at 650 nm among the stations with similar heat flux using the timeseries data collected in January 2017. 99

Chapter 1

Introduction

Estuarine and coastal waters are among the most dynamic and optically complex aquatic environments on Earth. These regions form critical transitional zones between terrestrial and marine ecosystems and exhibit steep gradients in salinity, nutrients, and hydrodynamic forcing. Such gradients drive high biological productivity and biodiversity (Mobley et al., 2004; Coble, 2007; Blough and Del Vecchio, 2002). However, their proximity to human settlements and industrial activities renders these waters highly susceptible to natural variability and anthropogenic pressures. Inputs from industrial effluents, agricultural runoff, and urban wastewater disrupt the biogeochemical equilibrium of these systems, often leading to harmful algal blooms, oxygen depletion (hypoxia), and the bioaccumulation of heavy metals and persistent organic pollutants (de Souza Machado et al., 2016; Sonak et al., 2018; Gobler, 2020).

Monitoring these dynamic environments is essential for sustainable coastal management. Traditional in-situ monitoring approaches lack spatial and temporal coverage required to capture the variability of optical properties in estuarine and coastal zones. In this context, remote sensing has emerged as an indispensable tool for synoptic water quality assessment (Kutser, 2009; Sathyendranath et al., 2017). Satellite-borne sensors enable the estimation of key optically active constituents (OACs), i.e., chlorophyll-a (Chl-a), total suspended matter (TSM), and chromophoric dissolved organic matter (CDOM), which together modulate underwater light availability and water column biogeochemistry (IOCCG, 2000; Brando and Dekker, 2003). The variability of OACs governs the inherent optical properties (IOPs) of the water column, influencing primary productivity, radiant heating, and the detectability of remote sensing reflectance.

Solar irradiance penetrating estuarine and coastal waters undergoes absorption and scattering processes that are shaped by the IOPs, namely, the absorption coefficient $a(\lambda)$, scattering coefficient $b(\lambda)$, and beam attenuation coefficient $c(\lambda)$, where λ represents the wavelengths between 400 and 700 nm. These parameters dictate underwater light field and ultimately govern

processes such as stratification, heat distribution, and ecosystem metabolism (Mobley et al., 2004; Nelson and Siegel, 2013). Distinct spectral signatures of Chl-a, TSM, and CDOM can be detected from space-based platforms, enabling the inference of ecosystem processes and pollution dynamics.

Interpreting remote sensing reflectance (R_{rs}) in estuarine and coastal waters is inherently challenging due to the complex interplay between absorption and scattering processes. R_{rs} is a nonlinear function of both $a(\lambda)$ and $b(\lambda)$, and its spectral shape reflects the coupled influence of all OACs present in the water column (IOCCG, 2006). In highly turbid and vertically heterogeneous environments, multiple scattering can dominate the light field, while variable CDOM and TSM concentrations can obscure phytoplankton signatures (Werdell et al., 2018; Ruddick et al., 2006). Moreover, vertical gradients in constituent concentrations, which are common in stratified estuarine systems and monsoon-influenced coastal plumes, introduce additional complexity that is not readily captured by standard surface-based remote sensing measurements (IOCCG, 2020). Accurately disentangling the contributions of individual OACs to R_{rs} thus requires sophisticated inversion approaches that account for both the inherent optical variability and the three-dimensional structure of the water column.

The spectral signatures of phytoplankton blooms, sediment resuspension, and terrestrial CDOM inputs reflect both the concentration and dynamic redistribution of OACs in estuarine and coastal waters. Phytoplankton blooms exhibit characteristic absorption features at ≈ 440 nm (blue) and ≈ 675 nm (red), with elevated reflectance near ≈ 550 nm (green) due to lower absorption (Babichenko et al., 2000; Mobley, 2022). Suspended sediments significantly enhance backscattering, particularly in the blue-green region, leading to brighter water-leaving radiance and elevated apparent turbidity (Nechad et al., 2010). Terrestrial CDOM inputs introduce strong absorption in the ultraviolet and blue regions, often masking phytoplankton signals and reducing light penetration (Coble, 2007; Blough and Del Vecchio, 2002). These constituents interact in nonlinear ways, producing complex spectral signatures that can confound simple empirical retrieval methods (IOCCG, 2006). Moreover, OAC concentrations and vertical distributions are highly dynamic, varying with river discharge, tidal mixing, wind-driven resuspension, and seasonal monsoonal cycles (Gilerson et al., 2010; Sathyendranath et al., 2017). Episodic events such as storms and floods can introduce large pulses of sediments and CDOM, rapidly altering the optical properties of surface waters. This optical complexity underscores the need for regionally adapted retrieval algorithms that can accurately account for the combined and variable influences of multiple OACs in monsoon-influenced estuarine and coastal systems.

Consequently, understanding optical variability in estuarine and coastal waters requires a

multidisciplinary approach that integrates physical oceanography, biogeochemistry, and bio-optical modelling. Remote sensing provides a powerful means to observe these dynamic environments, offering synoptic coverage and high temporal resolution that are not achievable through traditional field-based methods (Sathyendranath et al., 2017; Werdell et al., 2018). Satellite-derived observations can capture the evolving spatial patterns of OACs in response to river discharge, tidal forcing, wind-driven resuspension, and episodic events. However, translating remote sensing reflectance into accurate estimates of constituent concentrations remains challenging in optically complex systems such as monsoon-influenced estuaries (IOCCG, 2006; Massicotte et al., 2021).

The development of robust retrieval algorithms requires a detailed understanding of region-specific interactions between physical drivers and optical processes, as well as comprehensive calibration and validation using high-quality in-situ datasets (Brando and Dekker, 2003). As bio-optical variability directly affects ecosystem health, sediment dynamics, and radiant heating, advancing remote sensing approaches is essential for improving coastal monitoring, informing management strategies, and enhancing our ability to model climate-relevant feedback in these vulnerable systems. The following section reviews recent progress in coastal bio-optics and the evolving role of remote sensing in addressing these scientific and practical challenges.

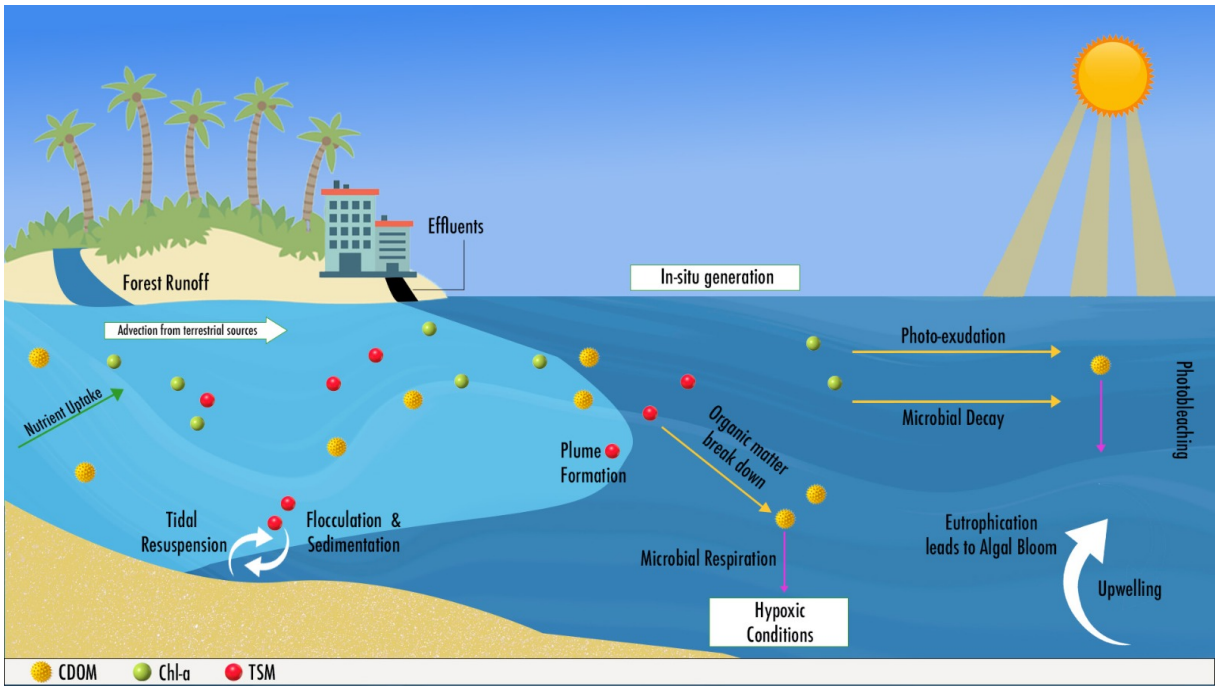

Figure 1.1: The schematic representation of the estuarine and coastal environment, highlighting important processes attributed to the observed variability in optically active constituents.

1.1 Coastal Bio-Optics and Remote Sensing

The bio-optical properties of estuarine and coastal waters play a pivotal role in modulating climate-relevant processes (Figure 1.1). In the visible spectrum, OACs govern the absorption and scattering of solar radiation, thereby influencing upper ocean heat budgets, vertical stratification, and feedback to regional and global climate systems (Chang and Dickey, 2004; Ohlmann et al., 2000). The partitioning of solar radiation between reflection, scattering, and absorption directly affects how much heat is retained in the surface ocean layers (Hill, 2008).

Among the OACs, CDOM plays a particularly important role due to its strong absorption in the ultraviolet and blue spectral regions. Elevated CDOM concentrations can significantly enhance surface heat absorption, promoting stratification, suppressing vertical mixing, and potentially amplifying the frequency and severity of hypoxic events in coastal waters (Hill, 2008; Soppa et al., 2019; Fichot and Benner, 2012; Massicotte et al., 2021). In Arctic and tropical coastal regions, CDOM-driven absorption has been shown to contribute to the timing and intensity of sea ice melt and coastal warming trends, with important implications for ecosystem dynamics and climate feedback (Soppa et al., 2019; Fichot and Benner, 2012). Moreover, the bio-optical influence on radiant heating is highly dynamic, responding to seasonal variability in river discharge, episodic extreme events (e.g., floods, storms), and anthropogenic pressures that alter CDOM and sediment loads (Bracher et al., 2017). These nonlinear interactions between optical and physical processes are increasingly recognised as a missing component in many regional climate and ecosystem models (Sathyendranath et al., 2019). Improved understanding of bio-optical feedback to climate is therefore critical, and satellite remote sensing offers a unique opportunity to quantify and monitor these processes across scales.

Remote sensing provides critical observational capacity for tracking bio-optical variability across broad spatial and temporal scales. Satellite observations are particularly valuable in coastal and estuarine regions, where traditional field-based monitoring is logistically challenging and often lacks sufficient spatial and temporal coverage (Matthews, 2011; Sathyendranath et al., 2019). Spaceborne ocean colour sensors enable synoptic, repeat observations of key bio-optical parameters, providing essential insights into ecosystem dynamics and climate feedback processes (IOCCG, 2020). Current and upcoming satellite missions offer a diverse set of observational capabilities. Multispectral sensors such as Sentinel-3 Ocean and Land Colour Instrument (OLCI) and Ocean Colour Monitor-3 (OCM-3) provide frequent coverage and wide swaths suitable for regional monitoring, while hyperspectral missions such as the Plankton, Aerosol, Cloud, ocean Ecosystem (PACE) mission are designed to capture fine spectral detail, enabling improved discrimination of optically active constituents in complex waters (Valente

et al., 2016; Pahlevan et al., 2021). Geostationary sensors, though still limited in number, offer high temporal resolution, critical for capturing rapidly evolving processes such as tidal mixing, phytoplankton blooms, and sediment resuspension events (Bracher et al., 2017). Applications of satellite ocean colour data in coastal and estuarine systems include the monitoring and forecasting of harmful algal blooms, assessment of pollution events and riverine plumes, tracking sediment transport dynamics, and estimating carbon fluxes (Mouw et al., 2015; Klein et al., 2019; Gokul et al., 2019).

The choice of algorithm for retrieving bio-optical properties depends strongly on the optical complexity of the target waters. Algorithms may be broadly classified as empirical, semi-analytical (SAA), or fully analytical (IOCCG, 2006; Li et al., 2023). Empirical algorithms, such as band-ratio methods, are computationally efficient and widely used but rely on simplified relationships between reflectance and OAC concentrations (Gitelson et al., 2008). These methods often perform poorly in optically complex coastal and estuarine waters where multiple OACs vary independently.

Semi-analytical algorithms represent a more physically based approach by incorporating radiative transfer theory to invert remote sensing reflectance into IOPs and then derive constituent concentrations (IOCCG, 2006; Brando et al., 2016). SAAs have been successfully applied in many coastal regions, but challenges remain in parameterising the diverse absorption and backscattering characteristics of TSM and CDOM, especially under highly variable monsoonal and river-influenced conditions (Ruddick et al., 2006). Additionally, the nonlinear interactions between absorption and scattering introduce uncertainties that limit the generalisability of SAAs across different coastal regimes.

Recent advances in hyperspectral remote sensing and machine learning (ML) are driving the development of next-generation coastal bio-optical algorithms. Hyperspectral inversion approaches leverage the full spectral shape of reflectance to better disentangle overlapping absorption features of OACs (Pahlevan et al., 2021). ML techniques, including neural networks, random forests, and hybrid physics-ML models offer powerful tools for capturing nonlinear relationships in high-dimensional data (Ruescas et al., 2018; Zhao et al., 2018). However, the success of ML approaches critically depends on the availability of extensive, high-quality training datasets that adequately sample the full range of optical variability in coastal environments (IOCCG, 2020; Werdell et al., 2018).

An emerging trend in coastal ocean colour science is the use of multi-sensor and multi-algorithm frameworks to improve retrieval robustness and accuracy (Bracher et al., 2017; IOCCG, 2020). Combining data from polar-orbiting and geostationary sensors, as well as integrating complementary algorithm outputs (e.g., ensemble approaches), can help mitigate the

limitations of individual methods and provide more consistent estimates of bio-optical parameters. The Ocean Colour Climate Change Initiative (OC-CCI) and upcoming PACE hyperspectral datasets will further enable the refinement of such frameworks (Sathyendranath et al., 2019; Werdell et al., 2018). Advancing these capabilities is essential for improving the monitoring of coastal water quality, ecosystem health, and climate feedback processes.

1.2 Rationale of Study

Estuarine and coastal systems are critical components of global biogeochemical cycles and provide key ecosystem services. However, significant knowledge gaps remain regarding the optical complexities of monsoon-influenced tropical estuaries, where rapid hydrological changes drive strong variability in OACs (Coble, 2007; Volta et al., 2020). Conventional ocean colour algorithms struggle to resolve the mixed and shifting spectral signatures characteristic of these systems (Morel and Prieur, 1977; Brando and Dekker, 2003).

Current satellite algorithms are primarily optimised for Case 1 waters, with limited applicability to Case 2 estuarine systems where TSM and CDOM vary independently (IOCCG, 2000; Gilerson et al., 2010). Recent advances in semi-analytical modelling and machine learning approaches show promise for enhancing retrieval accuracy in such environments. However, regional in-situ datasets required to support algorithm development remain scarce, particularly for monsoon-affected estuaries such as those along the Indian coast.

Furthermore, global bio-optical databases such as NASA bio-Optical Marine Algorithm Dataset (NOMAD) and GlobColour underrepresent estuarine systems, limiting the ability to generalise algorithm performance across diverse optical regimes (Werdell and Bailey, 2005; Aurin et al., 2013). Methodological inconsistencies in data collection and processing further impede the integration of regional datasets into global frameworks (D'Sa and DiMarco, 2009).

CDOM dynamics in particular are poorly constrained in climate models, despite their significant influence on upper ocean radiant heating and stratification (Fichot and Benner, 2012; Massicotte et al., 2021; Ohlmann et al., 2000). Understanding how CDOM variability modulates heat absorption in monsoon-influenced coastal systems is critical for improving regional climate predictions. This study addresses these knowledge gaps by advancing our understanding of coastal optical processes in Indian estuaries, with a focus on developing robust CDOM retrieval algorithms and linking bio-optical variability to radiant heating dynamics.

1.3 Objectives of Study

The objectives of this thesis are:

1. To quantify the influence of freshwater plume dynamics on bio-optical properties and associated radiant heating rates in coastal waters.

2. To analyse the bio-optical properties of estuarine outflows and associated plumes, with particular emphasis on CDOM variability as a proxy for organic pollution and biogeochemical processes.

The thesis explored the influence of spatial and temporal variability of OACs on radiant heating rates in the tropical coastal waters of the Eastern Arabian Sea off the coast of Goa. A classification framework for optical water types was proposed to elucidate the relationship between the prevailing OACs and heat absorption patterns under changing seasonal and hydrological regimes.

To address the second objective, a novel semi-analytical CDOM retrieval algorithm was developed, grounded in radiative transfer theory and optimised for application in highly turbid coastal waters. The algorithm facilitates the tracing of freshwater plume evolution, providing insights into hydrodynamic processes and biogeochemical cycling. It also supports the monitoring of organic pollution and early detection of hypoxia in vulnerable coastal zones.

1.4 Scope of Study

This study employs an integrated approach combining field-based observations and satellite remote sensing to characterise bio-optical variability in monsoon-influenced estuarine and coastal waters. The primary study areas include the *Mandovi* and *Zuari* estuaries along the west coast of India and the adjacent Eastern Arabian Sea.

Field campaigns encompass spectrophotometric and radiometric measurements across seasons to capture temporal variability in CDOM, Chl-a, and TSM. These observations are complemented by historical datasets from NOMAD and Global Ocean Carbon Algorithm Database (GOCAD) to enhance statistical robustness.

Satellite observations from Sentinel-3 OLCI and MODIS-Aqua provide large-scale context. A key component of the study involves the development and validation of a novel semi-analytical CDOM retrieval algorithm for turbid coastal waters. The work also includes classification of optical water types and quantification of radiant heating rates to elucidate potential climate feedbacks.

1.5 Thesis Outline

This thesis is organised into six chapters:

- **Chapter 1** introduces the research context, objectives, and significance of the study.
- **Chapter 2** details the methodology for data collection and processing, including field campaigns and satellite data analysis.
- **Chapter 3** presents the development and validation of the semi-analytical CDOM retrieval algorithm.
- **Chapter 4** applies the algorithm to analyse spatial and temporal CDOM variability and its ecological significance.
- **Chapter 5** introduces an optical water type classification framework and examines how bio-optical regimes influence radiant heating rates.
- **Chapter 6** synthesises key findings, discusses broader implications, and outlines future research directions.

Chapter 2

Data and Methodology

The previous chapter delineated the critical role of bio-optical properties in regulating energy balance, ecosystem health, and biogeochemical cycling in tropical estuarine and coastal waters. These properties, governed by optically active constituents (OACs), such as chromophoric dissolved organic matter (CDOM), chlorophyll-a (Chl-a), and total suspended matter (TSM) other than active Chl-a, exert strong control over the absorption and scattering of solar radiation, with direct implications on upper ocean heating, water clarity, primary production, and the onset of hypoxia (Chang and Dickey, 2004; Bélanger et al., 2013; Massicotte et al., 2021). However, as discussed, the synoptic retrieval of these parameters from satellite remote sensing remains highly challenging in optically complex waters, particularly under the influence of seasonal river discharge and anthropogenic perturbations. Addressing this challenge requires improved algorithms that can resolve spatial and temporal variability in OACs with higher accuracy and regional specificity.

This chapter presents the integrated data and methodological framework developed to support the thesis objectives. The overarching goal is to advance the remote sensing of bio-optical properties in Indian monsoon-influenced coastal waters and assess their role in modulating climate-relevant processes. The methodology combines three complementary approaches: (i) high-resolution in-situ bio-optical and hydrographic observations, (ii) satellite-based monitoring of ocean colour and surface reflectance, and (iii) radiative transfer modelling to link observed reflectance patterns to water column processes and radiant heating rates (RHR). This integrated approach enables the robust characterisation of OAC dynamics, supports the development of a novel semi-analytical CDOM retrieval algorithm, and informs the construction of an optical water type (O^T) classification scheme for the region.

Field campaigns were conducted strategically across contrasting phases of the Indian monsoon cycle, pre-monsoon, monsoon, and post-monsoon, capturing the extreme variability in hydrological forcing and its impact on OAC distributions and optical properties. Sampling covered both the Mandovi–Zuari estuarine system (MZE) and the broader Eastern Arabian Sea (EAS), facilitating a multi-scale perspective on bio-optical variability from nearshore to shelf waters. Radiometric and spectrophotometric measurements provided detailed vertical and spectral profiles of light fields and constituent absorption, while concurrent hydrographic observations allowed the interpretation of bio-optical signatures in the context of physical processes such as stratification, mixing, and plume dynamics.

A key focus of the thesis is to elucidate the influence of OAC variability on RHR in coastal waters, given its relevance to regional climate feedbacks such as increased sea surface temperatures and the intensification of tropical cyclones (Massicotte et al., 2021; Soppa et al., 2019). Initial analyses demonstrated that enhanced OAC absorption in nearshore regions, particularly during monsoon-driven discharge events, significantly modifies surface heat budgets. To better quantify these effects and improve remote retrievals of CDOM, a semi-analytical algorithm was developed and tuned to seasonal variability in the R_{rs} spectra. The algorithm was calibrated and validated against an extensive in-situ dataset collected across MZE and EAS domains, offering improved accuracy over standard empirical approaches.

In addition to algorithm development, a classification framework was established to segregate the optically diverse waters of the study area into distinct O^Ts based on bio-optical and radiometric properties. This typology supports the systematic analysis of heat absorption patterns and their linkage to OAC regimes, advancing our understanding of how bio-optical feedback interact with coastal climate processes.

Collectively, this chapter lays the methodological foundation for the analyses presented in subsequent chapters. It details the spatial and temporal scope of the field observations, the instrumentation and measurement protocols employed, the satellite data sources and processing workflows, and the computational techniques used for algorithm development and radiative transfer modelling. By integrating multi-platform observations and advanced bio-optical modelling, this work provides new insights into the optical complexity of tropical coastal waters and their broader significance within the regional climate system.

2.1 Description of Study Area

The data for the study was generated from two distinct bio-optical domains: the estuarine waters of Mandovi and Zuari rivers (Goa, India) and the coastal waters of the EAS. Mandovi and Zuari are two major rivers in Goa, India. Both originate in the Western Ghats (Sahyadri range)

and flow westward for approximately 70 to 75 kilometers before discharging into the Arabian Sea (Qasim and Sen Gupta, 1981) (Figure 2.1). The Mandovi flows into Aguada Bay, and the Zuari enters Mormugao Bay, both of which exhibit funnel shaped estuarine characteristics.

Aguada Bay spans 3.3 km at its mouth, narrowing to a 750 m wide inlet. The depth at the mouth reaches approximately 10 m, with an average bay depth of around 5 m. In contrast, Mormugao Bay features a 5 km wide opening, which narrows to 1 km near Cortalim, roughly 10 km inland (Shetye et al., 1995). Bathymetric features of this estuary include a depth reduction from 10 m at the mouth to a plateau of 2–3 m, followed by an increase to 8 m near the inlet and a subsequent decrease. These two estuaries are connected by the Cumbarjua Canal, which facilitates navigation through the system; however, the canal is too narrow to significantly influence estuarine dynamics.

In addition to the estuarine sites, the work incorporates bio-optical observations from the tropical coastal waters of the EAS. Numerous westward-flowing rivers originate in the Sahyadri range, which runs parallel to the western coastline of India. The orographic effect of the Sahyadri range on the southwest monsoon winds results in intense seasonal rainfall, with the monsoon season (June–September) contributing up to 80% of the region's annual precipitation. Though perennial, these rivers display marked seasonality in their discharge volumes.

Collectively, the rivers along the west coast contribute an annual freshwater discharge of approximately 255 km^3 into the EAS, transporting high levels of organic material into the coastal environment (Reddy et al., 2019). Apart from Mandovi and Zuari, other major rivers include the Kali, Sharavati, Haladi, Netravathi, Valapattanam, Chaliyar, Bharathapuzha, and Periyar (Figure 2.1).

Goa receives an average annual precipitation of approximately 3300 mm, largely governed by the southwest monsoon (Metri and Singh, 2010). The freshwater inflow into the MZE is primarily driven by land runoff from their respective catchment areas, contributing nearly 90–95% of the total annual discharge (Shetye et al., 2007). During the monsoon season, precipitation intensifies runoff from both the primary channels and their tributaries, resulting in a seasonal discharge volume nearly 40 times greater than the combined estuarine volume. These heavy rainfall events lead to significant flushing of the estuaries with low-salinity water (Shetye et al., 2007).

This influx of freshwater establishes a strong vertical stratification in the estuaries, with buoyant surface waters accelerating the ebb tide, while denser saline waters intrude landward along the bottom layers as a classical salt wedge system (Qasim and Sen Gupta, 1981). As the monsoon subsides, a decrease in riverine input allows saline water to intrude further upstream (Vijith et al., 2009). During the post-monsoon period (October to January), the flood flow

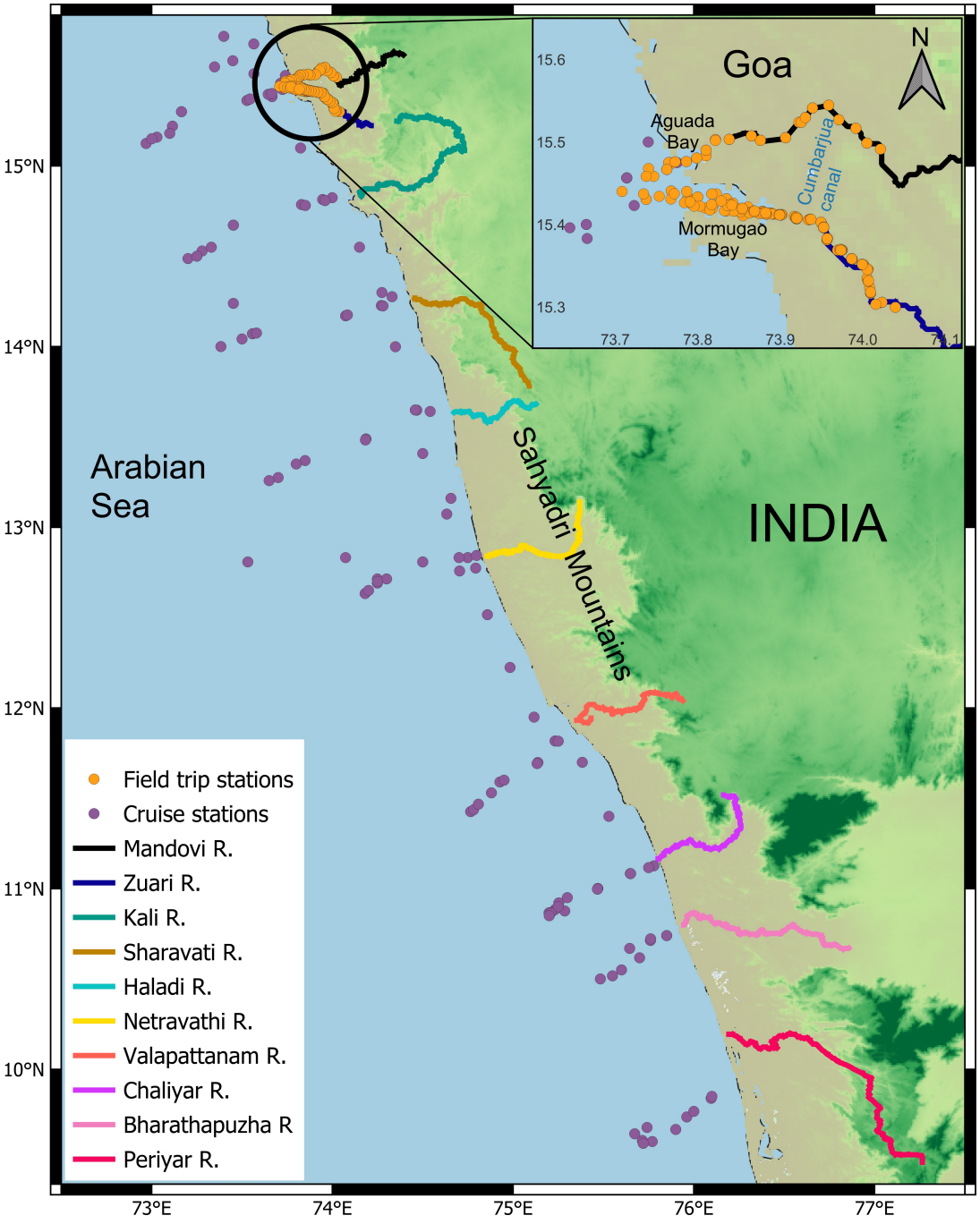

Figure 2.1: Map of the coastal Eastern Arabian Sea indicating cruise station locations (purple circles). The inset image highlights the Mandovi and Zuari estuarine region, indicating the location of the field survey stations (orange circles) .

dominates, creating a circulation pattern wherein flood tides typically enter along the southern edge of the estuarine bays and exit from the northern edge (Qasim and Sen Gupta, 1981). By the pre-monsoon period (February to May), riverine discharge becomes minimal, and the estuarine waters transition to a well-mixed state, resembling an extension of the adjacent sea (Vijith et al., 2016). Despite tidal intrusion being observed up to 65 km upstream in both rivers (Qasim and Sen Gupta, 1981), the upstream segments remain fresh due to channel narrowing and the resultant flow constraints (Shetye et al., 1995; Vijith et al., 2009).

To capture the spatial and temporal variability in bio-optical and hydrographic conditions across these dynamic systems, station selection was strategically designed. In the estuarine regions, sampling stations were aligned along the main channel axes of the Mandovi and Zuari rivers, extending into their upper reaches. Stations were selected to represent the full spectrum of hydrodynamic regimes across seasons. A key criterion for station selection was that water column depth be at least three times the Secchi depth, ensuring minimal bottom reflectance interference during optical measurements.

Field observations in the estuarine domain were conducted regularly between 2013 and 2024, covering all major seasons to ensure representative coverage of the monsoon-driven variability. Station locations for the MZE are illustrated in Figure 2.1. In the coastal domain, sampling transects were designed to span the continental shelf, covering depths from 10 m to 200 m. These transects were positioned adjacent to the mouths of major rivers along the western coast of India and oriented perpendicular to the shoreline. This design enabled effective monitoring of land-ocean interactions and seasonal shifts in water properties, especially under the influence of riverine discharge during pre- and post-monsoon periods.

Multiple research cruises supported coastal observations. Surveys were conducted aboard ORV Sagar Kanya (April 2008), ORV Sagar Purvi (December 2008), and ORV Sagar Sampada (April 2009 and 2010). Additional high-frequency time-series observations were conducted off the Mandovi and Zuari estuarine mouths onboard ORV Sagar Manjusha between 12th and 27th January 2017. These cruises captured surface water colour and the distribution of OACs, providing critical insights into temporal variability and underlying forcing mechanisms. Figure 2.1 shows the locations of all estuarine and coastal sampling stations included in this study.

2.2 Instruments and measurement protocols

Sampling and observations at each station were conducted concurrently, enabling the study to effectively capture the co-variability between bio-optical properties and hydrographic conditions. This synchronised approach ensured consistency in data interpretation, facilitating the assessment of how physical parameters influence the underwater light field and water column

optics.

2.2.1 Radiometer

The underwater light environment was characterised using a hyperspectral in-water radiometer (HyperPro II, Satlantic Inc.), deployed at each station. This free-falling profiler, with its streamlined hydrodynamic design, enables smooth descent at approximately 1 m s^{-1}, allowing accurate measurements of vertical light attenuation (Figure 2.2). For surface irradiance measurements, the instrument was mounted with a flotation collar to maintain position at the air-sea interface during time-series observations. The profiler was equipped with two Hyper-OCR sensors, one oriented upwards to measure downwelling irradiance, and another oriented downwards to capture upwelling radiance. The radiometer provided hyperspectral measurement between 349 to 803 nm.

Figure 2.2: (a) Hyperspectral radiometer. (b) Operations of the radiometer.

Integrated into the profiling system are ECO-series fluorometer and backscattering sensors, used to measure vertical distributions of Chl-a, CDOM, and the backscattering coefficient at 700 nm. To complement these observations, the profiler includes conductivity and temperature probes for determining salinity and thermal profiles, as well as pressure and tilt sensors for monitoring depth and profiling stability. The tilt sensor has an operational range of ±25°, with a resolution of 0.2°.

An additional irradiance sensor was mounted on the ship or trawler mast to measure

surface-reaching spectral irradiance (E_s), serving as a reference to ensure accuracy and consistency with in-water measurements. The profiler was deployed in the sunlit side of the vessel during clear-sky conditions, with care taken to avoid ship shadowing. Before each deployment, the instrument was pressure-tared. At each station, three high-quality downcasts with tilt angles less than 5° were recorded and retained for post-processing. The profiling continued either to one meter above the seabed or until photosynthetically active radiation (PAR) levels dropped below 1% of surface values.

Real-time monitoring of the instrument deployment was conducted using SatView (v2.9.5), allowing for continuous observation of the profiler's descent and orientation. Following each deployment, the collected data were post-processed using Satlantic ProSoft (v7.7), a dedicated software suite that converts raw measurements into multiple formats, including HDF, .mat, and ASCII. This software facilitates vertical binning of the radiometric data into 0.1-meter intervals and processes the information through various stages, from Level 1 (raw) to Level 4 (fully processed) products. The Level 4 outputs include a comprehensive set of optical parameters such as spectral E_s, above-surface and below-surface downwelling irradiance ($E_d^+(\lambda)$ and $E_d^-(\lambda)$), below-surface upwelling radiance ($L_u^-(\lambda)$), water-leaving radiance ($L_w^+(\lambda)$), and remote sensing reflectance ($R_{rs}(\lambda)$). In this notation, the subscript '+' refers to values measured just above the sea surface, while '–' denotes measurements taken just below of the interface. These parameters were calculated using established radiative transfer models, following the methodologies outlined by Mobley (2022), as

$$R_{rs}(\lambda) = \frac{L_w^+(\lambda)}{E_d^+(\lambda)} \tag{2.1}$$

where,

$$E_d^+(\lambda) = \frac{E_d^-(\lambda)}{1-\alpha} \tag{2.2}$$

and,

$$L_w^+(\lambda) = L_u^-(\lambda) \times \frac{1-\rho_f(\lambda,\theta)}{\eta_w^2(\lambda)} \tag{2.3}$$

The vertical profiles of upwelling irradiance (E_u) were derived from the upwelling radiance (L_u) by,

$$E_u(\lambda, z) = L_u(\lambda, z) \times Q_0 \tag{2.4}$$

where, Q_0 is the Bidirectional reflectance factor. For coastal waters of Arabian Sea, the value of Q_0 was ≈3.2. The vertical profiles of the diffuse attenuation coefficient of downwelling

irradiance (k_d) were computed as follows Lee et al. (2005),

$$k_d(z,\lambda) = \frac{1}{E_d(\lambda)} \times \frac{dE_d(\lambda)}{dz} \tag{2.5}$$

where the symbols α, ρ_f, and η_w stand for Fresnel reflection albedo from sun and sky (0.043), Fresnel reflectance index of seawater (0.021) and Fresnel refractive index of seawater (1.345), respectively.

2.2.2 CTD

The above observations were supplemented with measurements of the physical properties of the water column. The vertical profiles of salinity and temperature were generated using SeaBird Scientific's SBE 19plus V2 SeaCAT conductivity-temperature-depth (CTD) profiler (Figure 2.3). The CTD sensors had a response rate of 4 Hz, with accuracies of conductivity, temperature and pressure sensors having an accuracy of 0.0003 Sm^{-1}, 0.001°C & 0.1% of full scale range (600 m), respectively. At least three casts had been taken from each station for data aggregation, with care being taken to have a fixed rate of descent for the profiler.

The data was then extracted from the instrument using Seaterm (v2) software and converted to ASCII files using SBE Data Processing (v7.26) software. The software estimates the salinity and depth values from the measured conductivity and pressure readings, and the data was binned for every 10 cm depth. During profile aggregation, only downcast data were considered to mitigate the impact of potential cable tug.

2.2.3 Water Sampling

a. Niskin Sampler: Water samples were collected from the surface of the water column to estimate spectral absorption and concentration of various OACs present. The samples were collected using a 2-L Niskin Sampler (Figure 2.4). The sampler was deployed simultaneous to the deployment of the hyperspectral radiometer. During observations carried out in coastal waters onboard various research vessels, a rosette of 5-L Niskin Samplers was attached to the CTD and deployed off the side of the vessel. The sampler was rinsed before and after every sampling with distilled water.

b. Water Filtration Setup: The collected surface water samples were further filtered to estimate optical properties and concentrations of various optically active substances such as CDOM, Chl-a and TSM. The pump assembly used for filtration of the water sample consisted of a vacuum pump (Tarsons Rocyvac 300), Buchner funnel, conical filter flasks and vacuum tubing (Figure 2.5). For estimating the CDOM absorption coefficient, about 250

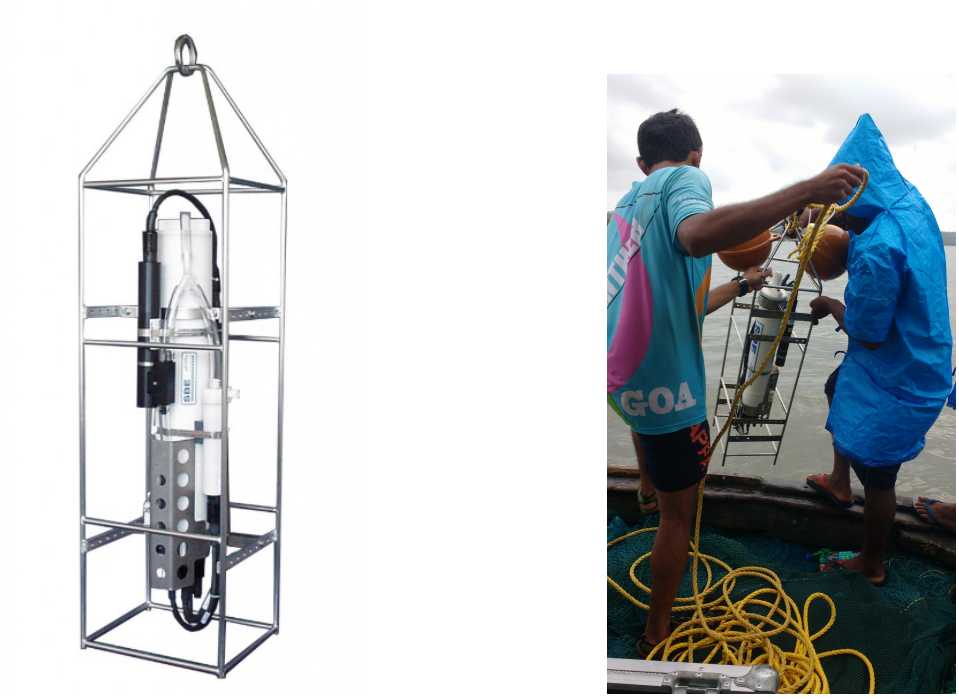

Figure 2.3: a) CTD Profiler. b) CTD profiling in operation

Figure 2.4: Niskin Sampler in operation.

ml of the sample collected was passed through 0.22 μm Sartorius membrane filter paper. A few drops (0.4 ml) of Mercuric Chloride ($HgCl_2$) were added to prevent the breakdown of dissolved organic matter in the aliquot due to microbial activity. The aliquot was transferred in amber-coloured bottles and stored in cold and dark conditions (Kowalczuk, 1999). For estimating Chl-a and TSM absorption coefficients, 1 L of sampled water was filtered through pre-weighed 0.45 μm glass fibre filter papers each to separate the particulate matter. For samples to carry out Chl-a analysis, a few drops of Magnesium Carbonate

($MgC0_3$) were added to reduce the adhesion of the phytoplankton to the filter papers. The filter paper was introduced in N, N-dimethylformamide (DMF) for 16-18 hours to preserve and extract the pigment (Suzuki and Ishimaru, 1990). The detritus was segregated by centrifuging only the DMF solution at 3000 rpm for 15 mins. The samples for TSM required the filter papers to be pre-combusted and to be kept in the oven at 60°C for 24 hours after filtration on returning to the lab.

Figure 2.5: Water filtration setup.

c. Spectrophotometry: The spectrophotometric analysis was performed using Shimazdu UV-2550 Spectrophotometer (Figure 2.6). The double-beam spectrophotometer estimated values from 349 to 803 nm with wavelength accuracy of 0.3 nm. The optical depth (OD) of CDOM and Chl-a samples was measured using a 5 cm quartz cuvette. Spectral absorbance measurements were conducted in triplicate, and the mean absorbance spectrum was used to compute the optical density. A fresh batch of Milli-Q water was used as a reference for CDOM samples, whereas DMF was used for Chl-a samples. Care was taken to conduct the operation in low-lighted conditions. The OD of TSM was recorded using the filter-pad technique with the integrating sphere component of the spectrophotometer. For reference, a moistened pre-combusted glass fibre filter paper was used. The spectrophotometer was operated using the UV-Probe software on a connected computer. Before each session, the *baseline* and *autozero* options were run for the empty chamber (no solution/filter paper added to the cuvette/holder) to avoid any instrument error. To mitigate potential sources of uncertainty in CDOM absorption measurements, such as

path-length amplification effects, cuvette alignment, and source spectral intensity variability, the spectrophotometer was annually calibrated in accordance with the manufacturer's recommendations.

Figure 2.6: Spectrophotometer

The spectral absorption coefficient for each OAC ($a_{oac}(\lambda)$) was computed from the OD using Beer-Lambert's law,

$$a_{oac}(\lambda) = 2.303 \times \frac{OD_{oac}(\lambda)}{l} \tag{2.6}$$

where, $a_{oac}(\lambda)$ is in m^{-1}, l is the length of the cuvette in metres. For TSM samples, the path length was computed as $l = V/A$, where V is the volume of the sample filtered, and A is the area over which the particles are collected in m^2. The specific absorption coefficient for Chl-a or TSM is given as,

$$a^*_{oac}(\lambda) = \frac{a_{oac}(\lambda)}{c_{oac}} \tag{2.7}$$

where, c_{oac} is the concentration of Chl-a (in μgL^{-1}) or TSM (mgL^{-1}). In scientific literature, the absorption of CDOM at 440 nm is the indicator for CDOM levels (a^{440}_{cdom}).

For CDOM, the remodelled exponentially decaying function was computed using the

spectrophotometrically estimated absorption coefficient of CDOM at 440 nm ($a_{cdom}^{440'}$) and the spectral slope (S_g) after subtracting the entire spectra with value of a_{cdom}^{700} to account for the errors introduced by colloid absorption (Green and Blough, 1994; Twardowski et al., 2004), as follows,

$$a_{cdom}(\lambda) = a_{cdom}^{440'} \times e^{-S_g(\lambda-440)} \tag{2.8}$$

2.3 Satellite Data Processing

Along with in-situ data, this study utilised optical data acquired from satellite-based ocean colour sensors to extend bio-optical analysis across broader spatial and temporal domains. Satellite remote sensing offers unparalleled synoptic coverage of coastal and estuarine waters, enabling the tracking of dynamic processes such as river plumes, phytoplankton blooms, sediment transport, and CDOM variability (Mouw et al., 2015; IOCCG, 2020). In this study, datasets from two major Earth observation missions were employed: the Sentinel-3 Ocean and Land Colour Instrument (OLCI), operated by the European Space Agency (ESA) and EUMETSAT; and the Moderate Resolution Imaging Spectroradiometer (MODIS) onboard NASA's Aqua satellite.

Both sensors offer long-term, consistent records of ocean colour and bio-optical parameters, supporting global and regional studies of marine and coastal environments (Brando et al., 2016; Werdell et al., 2018). Sentinel-3 OLCI provides enhanced spectral and spatial capabilities compared to previous sensors (e.g., Medium Resolution Imaging Spectrometer), with design features optimised for retrieval of optical water properties in coastal and inland waters (IOCCG, 2020). Moderate Resolution Imaging Spectrometer (MODIS) onboard Aqua, part of NASA's EOS mission series, delivers more than two decades of continuous ocean colour observations and remains a key dataset for climate-relevant marine research (Franz et al., 2005).

The use of multi-sensor data in this study enabled robust validation of in-situ derived algorithms and improved understanding of the spatial dynamics of OACs across the EAS and the MZE. The following sections provide technical details of each satellite sensor and describe the specific data processing procedures applied to support the objectives of this thesis.

2.3.1 Sentinel-3 OLCI

The primary satellite data used in this thesis is from the Sentinel-3 mission launched by the ESA. The mission has two identical sun-synchronous satellites flying out of phase (±140°) in the same low Earth orbit (814 km). Both these platforms have an OLCI to monitor the ocean colour. The instrument showed improved capability compared to Medium Resolution Imaging

Spectrometer instrument, onboard the ENVISAT satellite with only 15 bands in the same range, also designed by ESA. The improved design of OLCI also minimised sun glint contamination, had a broader field of view and repeated observations over a particular region every two days. The spatial resolution of the instrument is 300 m.

The European Organisation for the Exploitation of Meteorological Satellites (EUMETSAT) processes the remotely sensed data and publishes Level 1B and Level 2 data to its users free of charge in a near real-time and non-time-critical manner. For the algorithm validation and application, reprocessed geo-referenced Level 1B data was downloaded from the EUMETSAT data store (`https://data.eumetsat.int/`). The downloaded data was further processed using the Sentinel Application Platform (ESA SNAP; v9.9). The Case 2 Regional Coast Colour (C2RCC) was applied to estimate the surface leaving remote sensing reflectance for atmospheric correction.

2.3.2 Aqua MODIS

The satellite scans from MODIS onboard the NASA-launched Aqua satellite were also used to validate the CDOM algorithm put forward in this thesis. The MODIS instrument has a spatial resolution of 1km with 12 bands in the visible range and a revisit time over a particular region every 2 to 3 days. The cloud-free scans processed for surface reflectance data were obtained from Level 2 browser at `https://oceancolor.gsfc.nasa.gov/`

For both the above-mentioned satellite data, pixels with cloud cover and sun-glint risk were masked out. Validation was conducted over a 3-by-3 grid with in-situ data point's geolocation at the centre if at least 5 of the 9 pixels were valid. The values of the surface reflectance were averaged over the available pixels of the grid for this study.

The details about the computation related to the objectives of the thesis are explained in the data and methodology section of the particular chapters.

Chapter 3

A Novel Three-wavelength CDOM Retrieval Algorithm: Formulation and Global Validation

3.1 Introduction

Chromophoric dissolved organic matter (CDOM) is a key optically active constituent (OAC) in estuarine and coastal waters that exerts a profound influence on their inherent and apparent optical properties. CDOM consists of the light-absorbing fraction of the bulk dissolved organic matter pool, comprising a complex mixture of aromatic compounds, humic substances, and fulvic acids (Coble, 2007; Helms et al., 2008). It is characterised by strong absorption in the ultraviolet (UV) and short-wavelength visible regions of the spectrum, with absorption decreasing exponentially toward longer wavelengths (Bricaud et al., 1981). Through this optical behaviour, CDOM plays a dual ecological role, attenuating harmful UV radiation and modulating the underwater light field available for photosynthesis (Arrigo and Brown, 1996; Tedetti and Sempéré, 2006).

The sources of CDOM are both autochthonous and allochthonous. Allochthonous inputs originate from the microbial and photochemical degradation of terrestrial plant detritus, soil organic matter, and humic substances delivered via riverine discharge (Coble, 2007). Autochthonous contributions arise from the exudation of phytoplankton and macrophytes, microbial reworking of organic matter, and in-situ production processes (Stedmon and Markager, 2005). Once in the aquatic environment, CDOM constitutes a transient and reactive pool of dissolved organic carbon (DOC), undergoing continuous transformations via photobleaching, photo-oxidation, and microbial degradation (Fasching et al., 2014; Piccini et al., 2009). These

transformations contribute to nutrient regeneration, alter light penetration, and link CDOM dynamics to broader estuarine and coastal carbon cycling (Moran and Miller, 2007; Helms et al., 2008).

The spatio-temporal distribution of CDOM in estuarine and coastal systems is controlled by a dynamic interplay of physical and biogeochemical processes. Riverine discharge represents the dominant source of terrestrial CDOM, particularly during periods of elevated flow such as the monsoon season in tropical estuaries (Joshi et al., 2017; Bai et al., 2013; Cao et al., 2018). Physical processes, including estuarine circulation, tidal mixing, wind-driven resuspension, and stratification, regulate the horizontal and vertical transport of CDOM and its residence time within the system (Campanelli et al., 2017; Mannino et al., 2014; Tehrani et al., 2013). In monsoon-influenced systems, large seasonal pulses of terrestrial CDOM can drastically alter coastal optical properties and biogeochemical dynamics (Joshi et al., 2017; Reddy et al., 2019). In contrast, during the dry season or periods of low river flow, autochthonous sources and photochemical transformation dominate CDOM dynamics (Stedmon and Markager, 2005).

The high temporal and spatial variability of CDOM adds substantial complexity to the optical signature of estuarine and coastal waters. CDOM absorption overlaps spectrally with other OACs but varies independently of chlorophyll-a (Chl-a) and total suspended matter (TSM), particularly in Case 2 waters (IOCCG, 2000). This makes it challenging to isolate CDOM contributions from the total water-leaving radiance signal using conventional remote sensing approaches (Werdell et al., 2018). In optically complex environments, CDOM variability also influences vertical light penetration, heat absorption, and primary production (Massicotte et al., 2021).

Despite these challenges, remote sensing provides a powerful tool for tracking CDOM dynamics over large spatial and temporal scales. Multispectral sensors (e.g., MODIS, OLCI) and, increasingly, hyperspectral instruments (e.g., PACE) offer the spectral resolution required to differentiate CDOM absorption features (Mouw et al., 2015; IOCCG, 2020). Advances in algorithm development, including semi-analytical (SAA) and machine learning (ML) approaches, have improved CDOM retrievals in turbid and dynamic coastal waters (Nechad et al., 2010; Ruescas et al., 2018). Such capabilities enable better understanding of CDOM transport pathways, links to land-sea interactions, and feedbacks to regional climate processes (Fichot and Benner, 2012; Bélanger et al., 2013).

The spectral remote sensing reflectance (R_{rs}) is fundamentally governed by the inherent optical properties (IOPs) of water, primarily absorption and backscattering. The ratio of backscattering to absorption shapes both the magnitude and spectral distribution of R_{rs}, providing the foundation for deriving bio-optical properties from remote sensing data as,

$$R_{rs}(\lambda) \propto \frac{b_b(\lambda)}{a(\lambda) + b_b(\lambda)} \tag{3.1}$$

where,

$$a(\lambda) = a_{sw}(\lambda) + a_{chl}(\lambda) + a_{tsm}(\lambda) + a_{cdom}(\lambda) \tag{3.2}$$

$$b_b(\lambda) = b_{b_{sw}}(\lambda) + b_{b_{chl}}(\lambda) + b_{b_{tsm}}(\lambda) \tag{3.3}$$

The symbols $a(\lambda)$ and $b_b(\lambda)$ denote the spectral total absorption and backscattering coefficients. In equation 3.2, the terms $a_{sw}(\lambda)$, $a_{chl}(\lambda)$, $a_{tsm}(\lambda)$, $a_{cdom}(\lambda)$ are the absorption coefficients of seawater, Chl-a, TSM, and CDOM, respectively. Similarly, in equation 3.3, the terms $b_{b_{sw}}(\lambda)$, $b_{b_{chl}}(\lambda)$, $b_{b_{tsm}}(\lambda)$ are the backscattering coefficients of seawater, Chl-a and TSM, respectively.

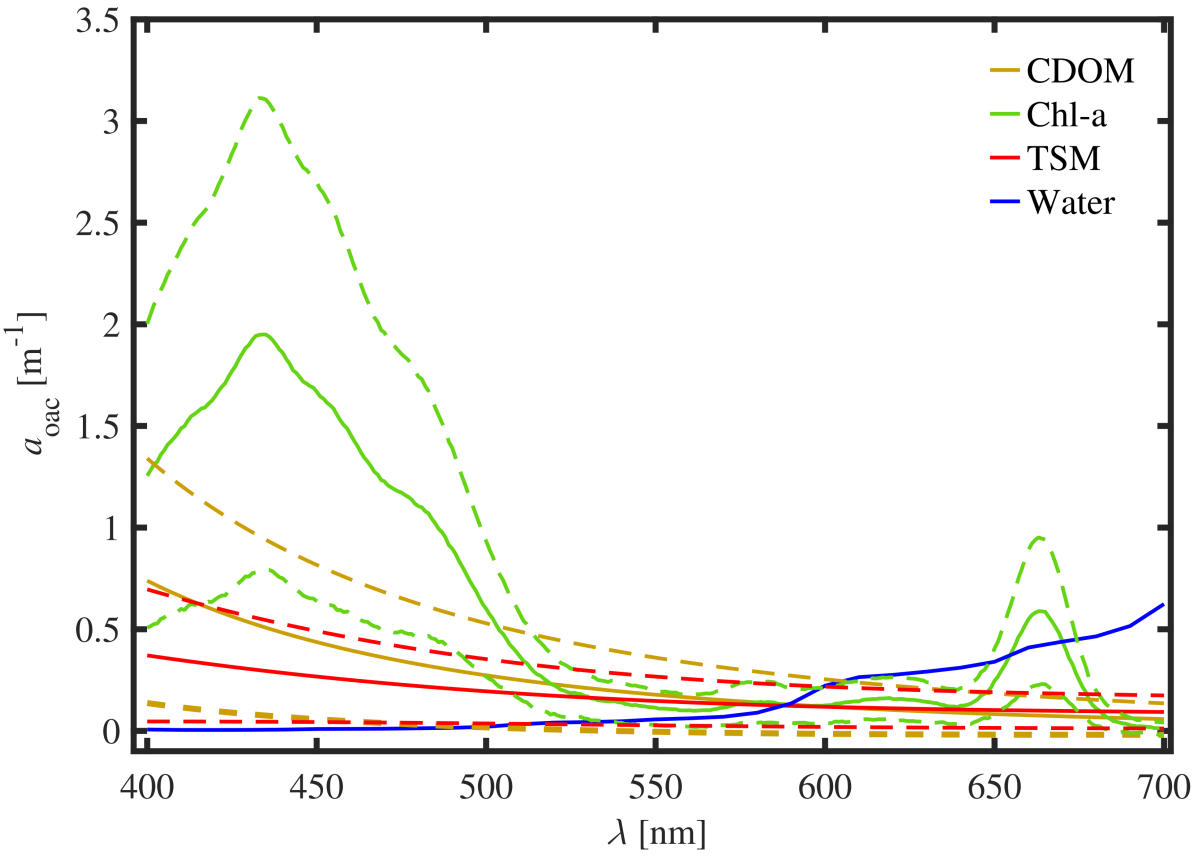

Figure 3.1: The mean (solid) and maximum/minimum (dotted) spectral absorption of CDOM (yellow), Chl-a (green), TSM (red) and seawater molecules (blue) for the Mandovi and Zuari estuarine regions and the coastal waters of eastern Arabian Sea.

Figure 3.1 illustrates the absorption characteristics of the principal OACs found in estuarine and coastal waters along the west coast of India. Among these, Chl-a typically dominates light absorption in productive waters. Its spectral signature features a prominent absorption peak near ≈443 nm (blue region) and a secondary peak at ≈663 nm (red region), with enhanced reflectance in the green portion of the spectrum owing to reduced absorption in this band (Bricaud et al., 1995). The exact shape and magnitude of the Chl-a absorption spectrum is modulated by phytoplankton species composition, cell morphology, intracellular pigment packaging effects, and environmental factors such as nutrient availability and light acclimation (Bricaud et al., 1998; IOCCG, 2006).

The absorption spectra of CDOM exhibit strong absorption in the UV and blue portions of the spectrum, with absorption values declining exponentially toward longer wavelengths (Figure 3.1). The spectral slope of CDOM absorption is a useful diagnostic parameter that provides information on CDOM composition and source. Steeper slopes (higher values of S_g) are typically associated with terrestrial humic material, while flatter slopes may indicate autochthonous, microbial, or photochemically altered CDOM (Helms et al., 2008). This distinction is particularly relevant in monsoon-influenced estuaries, where seasonal shifts in CDOM source material are pronounced (Joshi et al., 2017; Reddy et al., 2019).

In contrast, TSM exhibits a broad absorption spectrum, with a gradual decline in absorption from blue to red wavelengths. The spectral shape of TSM absorption is largely governed by the mineralogical and organic composition of suspended particles, which vary across spatial and seasonal scales (Bowers and Binding, 2006; Neukermans et al., 2012). Pure seawater absorption, dominated by water molecules, increases strongly in the red and near-infrared regions (Pope and Fry, 1997). The absorption spectra of these OACs show significant overlap, particularly in the blue and red regions, creating challenges for isolating individual component signals from water-leaving radiance.

Modelled spectral backscattering characteristics of particulate OACs, particularly TSM and Chl-a, in the Mandovi-Zuari Estuarine system (MZE) reveal peaks in the backscattering spectrum between 500–600 nm in Chl-a-dominant waters and between 600–700 nm in stratified waters with elevated TSM concentrations (Adhikari et al., 2023). The backscattering and absorption properties of Chl-a and TSM are highly variable and influenced by factors such as phytoplankton community structure, sediment mineralogy, and particulate concentration (Bricaud et al., 1995; Roesler et al., 1989; Stramski et al., 1999).

Natural variability in OAC characteristics, including concentration, source, and optical interactions, introduces substantial complexity into the R_{rs} signal (IOCCG, 2000). Equations 3.1,

3.2, and 3.3 highlight how R_{rs} depends on the combined effects of absorption and backscattering. Isolating the spectral signature of CDOM from this complex signal is particularly challenging due to the co-variance and spectral overlap with other OACs in optically dynamic estuarine and coastal waters (Mannino et al., 2008; Aurin et al., 2018). Historically, a variety of algorithmic approaches have been developed to estimate CDOM absorption from R_{rs} spectra, including empirical, semi-empirical, analytical, and semi-analytical methods. Among these, band-ratio (BR) algorithms remain the most widely used due to their simplicity and computational efficiency. These approaches typically involve regressing ratios of R_{rs} at selected visible wavelengths against in-situ CDOM absorption measurements (Campanelli et al., 2017; Chen et al., 2017b; D'sa et al., 2006; Mabit et al., 2022; Mannino et al., 2008; Menon et al., 2011). Despite their ease of implementation, BR models often perform poorly in optically complex coastal waters, with performance highly dependent on region, season, and dataset (Matthews, 2011; Lotliker et al., 2015; Najah and Al-Shehhi, 2021).

Attempts to generalise CDOM retrieval have led to global algorithms such as those of Tiwari and Shanmugam (2011) and Aurin et al. (2018). However, these algorithms often struggle in coastal environments, where highly variable OAC composition and hydrodynamics complicate retrievals. Analytical and SAA approaches based on radiative transfer theory offer a more mechanistic understanding of light interactions in water and can, in principle, disentangle the contributions of different OACs (IOCCG, 2006).

Prominent examples of such models include the Garver-Siegel-Maritorena model (Garver and Siegel, 1997; Maritorena et al., 2002; Maritorena and Siegel, 2005), Linear Matrix Inversion (Hoge and Lyon, 1996), and the Quasi-Analytical Algorithm (QAA) (Lee et al., 2002). These models relate R_{rs} to IOPs such as the $a(\lambda)$ and the $b_b(\lambda)$, enabling estimation of CDOM absorption. However, performance evaluations have shown that these models frequently underperform in estuarine and coastal regions such as the northern South China Sea, tropical Australia, the northwestern Bay of Bengal, the eastern Arabian Sea, the Gulf of California, and Chesapeake Bay (Najah and Al-Shehhi, 2021).

To improve retrieval accuracy, some studies have explored re-parameterisation of IOPs using site-specific relationships or by substituting near-infrared bands for red bands to improve sensitivity to TSM and CDOM variability (Nechad et al., 2010; Werdell et al., 2018). Although such refinements can improve performance in certain regions, their generalisability remains limited, necessitating further regional adaptation and validation (Ruescas et al., 2018). Neural network-based approaches have also been investigated for CDOM retrieval (Chen et al., 2017a), but these are often constrained to open ocean applications due to their reliance on extensive, high-quality training datasets and the greater optical homogeneity of oceanic waters.

The core limitation of many existing approaches lies in their inability to fully account for the highly dynamic optical regimes of estuarine and coastal waters, where physical, biogeochemical, and hydrodynamic processes drive rapid and nonlinear changes in OAC composition and distribution (Odermatt et al., 2012; Blondeau-Patissier et al., 2014). As a result, CDOM retrieval in these environments remains a significant challenge for current remote sensing methodologies.

Recent advances in computational capacity have spurred interest in ML-based algorithms for CDOM retrieval (Ruescas et al., 2018; Zhao et al., 2018; Sun et al., 2021). ML models, such as random forests, support vector machines, and deep neural networks, can capture nonlinear relationships between R_{rs} and CDOM absorption, offering improved performance in optically complex waters. However, the application of ML techniques requires extensive and well-representative training datasets, substantial computational resources, and advanced expertise, which can limit their accessibility and transferability across different regions.

In this chapter, a novel and computationally efficient SAA is proposed for the retrieval of CDOM absorption at 440 nm (a_{cdom}^{440}) in optically complex estuarine and coastal waters. The approach leverages a simple three-wavelength index designed to enhance sensitivity to CDOM while minimising confounding influences from other OACs. Section 3.2 details the datasets used in algorithm development and validation, Section 3.3 presents the formulation of the index and its performance evaluation, while Section 3.4 discusses the validation results across diverse turbid water regimes. Section 3.5 addresses the algorithm's advantages, limitations, and future prospects for operational applications in coastal remote sensing.

3.2 Data

3.2.1 Datasets

The distribution and sources of OACs in global estuarine and coastal waters are governed by a complex interplay of environmental factors that leads to pronounced spatial and temporal variability. To effectively account for this variability and enable the development of an algorithm for accurate CDOM concentration estimation, data from the following datasets were compiled and thoroughly analysed.

In-situ

The in-situ dataset, collected between 2008 and 2024, served as the primary dataset for the development of the algorithm described in Chapter 2. The procedures involved in the collection and processing of this dataset are detailed in section 2.2.

NOMAD

The NASA bio-Optical Marine Algorithm Dataset (NOMAD) is a globally distributed archive of in-situ measurements comprising spectral R_{rs}, coincident IOP observations such as absorption and backscattering coefficients, along with associated metadata relevant to observational protocols and environmental conditions. Curated by the NASA Ocean Biology Processing Group, NOMAD compiles data collected by the international ocean colour research community and serves as a key resource for the calibration, validation, and development of ocean colour algorithms. The dataset plays an essential role in supporting global scale assessments of marine biogeochemical variability and in improving satellite based retrievals across diverse water types. Detailed information about NOMAD and access to the dataset are available at: `https://seabass.gsfc.nasa.gov/wiki/NOMAD` (Werdell and Bailey, 2005).

GOCAD

The Global Ocean Carbon Algorithm Database (GOCAD) is a comprehensive compilation of ocean colour observations gathered from over 500 field campaigns over the past three decades. This dataset, developed by Aurin et al. (2018), includes in-situ measurements of R_{rs} along with multi- or hyperspectral CDOM absorption data. It also encompasses DOC levels, IOPs such as absorption and backscattering from various constituents, and associated physical and biogeochemical parameters, where available. The database was designed to aid in the development and refinement of remote sensing algorithms for accurately estimating CDOM and DOC concentrations in aquatic environments. The collection of such extensive data allows researchers to address the challenges of estimating CDOM in optically complex waters, a critical component for ocean colour studies and carbon cycling in marine ecosystems (Aurin et al., 2018; Lee et al., 2002; Werdell and Bailey, 2005).

For algorithm development, only surface layer data (less than 2 meters from the surface) from tropical and temperate regions (between 60 °S to 60 °N) were included. This geographic restriction was necessary because OAC interactions in the Arctic and near Antarctic coasts differ significantly, with CDOM dominating the OACs year-round (Matsuoka et al., 2007, 2013). Most of the observations from the aforementioned databases were collected from open ocean waters. To ensure the data was relevant for the study, only those meeting the Case 2 criterion, where the ratio of R_{rs} of 412 nm to 443 nm $\leq$ 1; were selected following the methodology outlined by Matsushita et al. (2012). The complete dataset was randomly split into formulation and validation sets, containing 850 and 649 data points, respectively (Table 3.1). Some spectral R_{rs} observations were obtained using multiwavelength radiometers instead of hyperspectral radiometers, meaning only 502 out of the 850 data points had hyperspectral data available

for the developmental analysis. Data from campaigns where the absorption of all OACs was measured were utilised to map their respective absorption budgets. Regression analysis was performed only on data points where CDOM absorption contributed at least 33% of the total absorption budget, ensuring the CDOM signal was isolated and not influenced by Chl-a or TSM attenuation. The validation dataset consisted of 550 data points, with no satellite match-ups. However, 19 and 80 unique data points had concurrent overpasses from the Ocean and Land Colour Instrument (OLCI) and the Moderate Resolution Imaging Spectroradiometer (MODIS), respectively, as specified in Section 2.3 of chapter 2.

Table 3.1: The details of the combined dataset and its subsets used for the formulation and validation of the CDOM retrieval algorithm.

Dataset	**No. of points in the dataset**	**Description of data points**	**No. of points in the subset**	**Original dataset**
Formulation	850	All data points with available hyperspectral R_{rs} and OAC absorption	502	Regional (MZE and coastal EAS), GOCAD
		All data points where CDOM influence on the absorption budget was greater than 33% at 440 nm	348	Regional (MZE), GOCAD & NOMAD
Validation	649	Only in-situ validation points	550	Regional (MZE and coastal EAS), GOCAD & NOMAD
		OLCI match-ups	19	Regional (MZE and coastal EAS), GOCAD
		MODIS match-ups	80	GOCAD & NOMAD

3.2.2 Statistical Analysis

A suite of statistical metrics was employed to evaluate the performance of the proposed CDOM retrieval algorithm during its development, validation, and comparison with previously published algorithms. These metrics quantify the degree of agreement between algorithm estimates and corresponding in-situ observations and provide insights into both the accuracy and bias of the retrievals. The statistical measures used are described below.

a. Coefficient of determination: The coefficient of determination (r^2) quantifies the proportion of the variance in the observed (in-situ) variable that is explained by the model estimates. It provides an indication of the goodness-of-fit between the estimated and measured values. The coefficient ranges between 0 and 1, where values closer to 1 indicate a stronger linear relationship between the model and observations. It is computed as follows,

$$r^2 = 1 - \frac{\sum(y_{estimated} - y_{insitu})^2}{\sum(y_{insitu} - \overline{y_{insitu}})^2} \tag{3.4}$$

where, y_{insitu} represents the in-situ measurements, $y_{estimated}$ represents the corresponding model-derived estimates, and $\overline{y_{insitu}}$ is the mean of the in-situ measurements.

b. Root mean square error: The Root Mean Square Error ($rmse$) provides an absolute measure of the average magnitude of the errors between the model estimates and the corresponding in-situ observations. It is sensitive to large errors due to the squaring of residuals and is widely used as an indicator of the overall accuracy of a model. $rmse$ is computed as,

$$rmse = \sqrt{\frac{\sum(y_{estimated} - y_{insitu})^2}{n}} \tag{3.5}$$

where, n is the number of data points.

c. Bias: Bias quantifies the systematic deviation of the model estimates from the in-situ observations. It indicates whether the algorithm tends to overestimate or underestimate the parameter of interest. A positive bias suggests overestimation, whereas a negative bias indicates underestimation. Bias is computed as,

$$bias = \frac{\sum(y_{estimated} - y_{insitu})}{n} \tag{3.6}$$

d. Mean absolute error: The Mean Absolute Error (mae) provides the average magnitude of the absolute differences between model estimates and in-situ measurements, irrespective of direction (i.e., whether the error is positive or negative). It is less sensitive to outliers than $rmse$ and provides an intuitive measure of model accuracy. mae is calculated as,

$$mae = \frac{\sum|y_{estimated} - y_{insitu}|}{n} \tag{3.7}$$

e. Mean absolute percentage error: The Mean Absolute Percentage Error ($mape$) expresses the mae as a percentage of the in-situ measurements. It provides a dimensionless and

easily interpre indicator of model performance, enabling comparison across datasets with varying scales and distributions. $mape$ is particularly useful when comparing relative errors. It is computed as,

$$mape = \frac{100}{n} \sum \left| \frac{y_{estimated} - y_{insitu}}{y_{insitu}} \right| \tag{3.8}$$

3.3 Methodology

3.3.1 Theory and Conceptual Basis of the Algorithm

In this study, a SAA was developed to estimate the a_{cdom}^{440}, from R_{rs} spectra. The algorithm is grounded in the fundamental relationships between the IOPs of CDOM and the spectral response of R_{rs}.

CDOM, unlike other OACs, strongly absorbs incoming solar radiation in the UV and blue portions of the spectrum but contributes minimally to light scattering. Its absorption influences the shape and magnitude of R_{rs} by attenuating the upwelling radiance, especially at shorter wavelengths. This unique spectral behavior provides a theoretical basis to isolate the contribution of CDOM from other optical influences.

Building upon the work of Gitelson et al. (2008), Menon and Adhikari (2018), and Adhikari and Menon (2022), we propose a three-wavelength index that captures the relative absorption effect of CDOM in a computationally efficient manner,

$$a_{cdom}^{440} \propto \left(\frac{1}{R_{rs}(\lambda_1)} - \frac{1}{R_{rs}(\lambda_2)} \right) \times R_{rs}(\lambda_3) \tag{3.9}$$

This formulation is designed to account for the specific spectral properties of CDOM and mitigate interference from other OACs such as Chl-a and TSM.

3.3.2 Conceptual Reasoning

The proposed index is based on the following key observations.

First, CDOM does not significantly contribute to backscattering in the water column; its optical impact is largely limited to absorption. Therefore, the inverse of R_{rs} at a wavelength strongly influenced by CDOM absorption should vary proportionally with a_{cdom}. Mathematically, this relationship is expressed as:

$$a_{cdom} \propto \frac{1}{R_{rs}(\lambda)}. \tag{3.10}$$

To enhance the selectivity for CDOM absorption, the index uses the difference between the inverses of R_{rs} at two wavelengths (λ_1 and λ_2). The first wavelength λ_1 is selected in a spectral region where CDOM absorption is dominant, while λ_2 is chosen such that the absorption effects of Chl-a, TSM, and seawater molecules are comparable to those at λ_1, allowing the differential term to effectively isolate the CDOM absorption signal from other interfering signals.

$$\left(\frac{1}{R_{rs}(\lambda_1)} - \frac{1}{R_{rs}(\lambda_2)}\right) \tag{3.11}$$

Second, to compensate for the influence of particulate scattering and absorption (primarily from Chl-a and TSM), a multiplicative normalisation factor $R_{rs}(\lambda_3)$ is introduced. The wavelength λ_3 is carefully selected from a region where the absorption by particulates is minimal and where the contribution of CDOM to R_{rs} is also relatively low. This helps reduce variability introduced by the backscattering coefficient $b_b(\lambda)$, which is common to both numerator and denominator in the fundamental expression for R_{rs} (see Equations 3.1, 3.3).

Since the IOPs of pure seawater are relatively well-known and consistent, the remaining variability in R_{rs} is primarily driven by the varying concentrations and spectral properties of particulate backscattering and absorption. The magnitude of particulate backscattering $b_b(\lambda)$ in turbid coastal waters typically ranges from 10^{-4} to 10^{-2} m^{-1}, whereas the corresponding absorption coefficients $a(\lambda)$ are generally one to two orders of magnitude higher. Because $b_b(\lambda)$ appears in both the numerator and denominator of the remote sensing reflectance equation, its influence is largely minimised, leaving absorption as the dominant driver of spectral variability.

Finally, the selection of λ_3 is optimised to ensure that the resulting index remains minimally sensitive to Chl-a and TSM variations, thereby improving the robustness of CDOM retrieval across a wide range of optical conditions.

3.3.3 Summary of Concept

In summary, the proposed three-wavelength index was formulated to,

- leverage the inverse relationship between R_{rs} and CDOM absorption at carefully selected wavelengths.
- Utilise differential inverse R_{rs} to isolate CDOM's influence from other OACs.
- Normalise the index using a third wavelength λ_3 with minimal particulate influence, thereby enhancing retrieval accuracy.

This semi-analytical design provides a computationally simple yet physically simplified approach for estimating a_{cdom}^{440} in optically complex estuarine and coastal waters. The next

section 3.3.4 details the specific wavelength selection, index calibration, and performance evaluation of this algorithm using a diverse dataset.

3.3.4 Wavelength Selection for the Index

The formulation of the three-wavelength index (Equation 3.9) requires careful selection of spectral bands that optimise sensitivity to CDOM absorption while minimising interference from other OACs. To identify these wavelengths, a systematic partial differential analysis was conducted using the formulation dataset, which consisted of 502 samples with hyperspectral R_{rs} and corresponding OAC absorption measurements (Table 3.1).

This approach of radiative transfer theory shows that R_{rs} is inversely related to the total absorption and directly related to the backscattering within the water column (IOCCG, 2006). Therefore, the spectral response of R_{rs} to specific absorbing components such as CDOM can be quantitatively explored through partial derivatives of R_{rs} with respect to the absorption coefficients of these components. In highly turbid estuarine and coastal waters, where bio-optical complexity is substantial, this analysis provides a principled method to isolate wavelengths where CDOM absorption dominates the spectral variability of R_{rs} (Odermatt et al., 2012; Blondeau-Patissier et al., 2014).

The selection of these three wavelengths, i.e., λ_1, λ_2, and λ_3, was performed in three sequential steps,

1. Identification of λ_1: Sensitivity to CDOM absorption

   The first wavelength, λ_1, was selected to maximise sensitivity to CDOM absorption. For each data point in the dataset, the partial derivative of R_{rs} with respect to a_{cdom} was computed, i.e., $\frac{\partial R_{rs}}{\partial a_{cdom}}$. This derivative quantifies the responsiveness of R_{rs} to changes in CDOM absorption, thereby identifying spectral regions where CDOM exerts the greatest influence on the water-leaving radiance.

   The analysis was restricted to the spectral range of 400–450 nm, where CDOM absorption is typically strongest due to its characteristic exponential decay toward longer wavelengths (Twardowski et al., 2004; Helms et al., 2008). The resulting histogram of $\frac{\partial R_{rs}}{\partial a_{cdom}}$ peaks (Figure 3.2a) indicated that for 166 spectra, maximum sensitivity occurred at 400 nm. Accordingly, 400 nm was selected as λ_1 to ensure maximum responsiveness of the index to CDOM variability.

2. Identification of λ_2: Minimising confounding absorption

   The second wavelength, λ_2, was chosen to minimise differential absorption effects from Chl-a, TSM, and seawater molecules in the index term,

$$\left(\frac{1}{R_{rs}(\lambda_1)} - \frac{1}{R_{rs}(\lambda_2)}\right). \tag{3.12}$$

To identify λ_2, the cumulative absorption of non-CDOM components was calculated at each wavelength:

$$a_{chl}(\lambda) + a_{tsm}(\lambda) + a_{sw}(\lambda) \tag{3.13}$$

The optimal λ_2 was the wavelength where this cumulative absorption most closely matched that at λ_1, thus ensuring that the difference term isolates CDOM absorption rather than reflecting differences in other absorbers. This approach leverages the fact that a minimal difference in total non-CDOM absorption at λ_1 and λ_2 reduces the likelihood of systematic errors when estimating a_{cdom}^{440}.

The histogram of optimal wavelengths (Figure 3.2b) revealed that for 148 data points, the minimum cumulative absorption difference was observed between 460 and 470 nm. Consequently, 465 nm (the centre of this range) was selected as λ_2. The cumulative absorption at 465 nm exhibited a strong correlation with that at 400 nm ($r^2 = 0.92$; Figure 3.2c), confirming its suitability.

3. Identification of λ_3: Minimising sensitivity to particulate absorption and backscattering

   The third wavelength, λ_3, was introduced to normalise the index and further reduce the impact of particulate absorption on the estimation of CDOM absorption. In highly turbid coastal waters, the contribution of Chl-a and TSM to R_{rs} can vary substantially across seasons and regions, thereby confounding CDOM retrieval if not properly accounted for (Brando and Dekker, 2003).

   To identify λ_3, the partial derivatives $\frac{\partial R_{rs}}{\partial a_{chl}}$ and $\frac{\partial R_{rs}}{\partial a_{tsm}}$ were computed for each sample. The spectral inflection points where these derivatives reached a minimum were interpreted as wavelengths where R_{rs} was least sensitive to variations in Chl-a and TSM.

   The histograms of these minima (Figures 3.2d–e) showed that for 71 and 79 stations, respectively, the absolute minima in $\frac{\partial R_{rs}}{\partial a_{chl}}$ and $\frac{\partial R_{rs}}{\partial a_{tsm}}$ occurred within the 570–580 nm range. Based on these findings, 575 nm was selected as λ_3.

Based on this comprehensive wavelength selection procedure, the final three-wavelength index for estimating a_{cdom}^{440} was formulated as,

$$\left(\frac{1}{R_{rs}^{400}} - \frac{1}{R_{rs}^{465}}\right) \times R_{rs}^{575}. \tag{3.14}$$

This index is expected to improve the retrieval accuracy of CDOM absorption in optically complex estuarine and coastal waters by optimising spectral sensitivity and mitigating confounding effects from other OACs. The methodology adopted here represents a robust, SAA grounded in radiative transfer principles and empirical bio-optical analysis, which is particularly well-suited for application in regions characterised by strong seasonal and spatial variability in bio-optical properties.

3.3.5 Algorithm formulation

The above-determined CDOM index (equation 3.14) was regressed against in-situ a_{cdom}^{440} in the formulation dataset, with the contribution of CDOM to the absorption budget being greater than 33% (n = 384). The criterion was established to train the model while minimising the noise from attenuation of Chl-a and TSM. The regression curve considered was a polynomial of the second degree (Figure 3.3). The algorithm to estimate a_{cdom}^{440} was identified as,

$$a_{\text{CDOM}}^{440} = -0.00146x^2 + 0.1854x + 0.025 \tag{3.15}$$

where, $x = \left(\frac{1}{R_{rs}^{400}} - \frac{1}{R_{rs}^{465}}\right) \times R_{rs}^{575}$. The statistics for best-fitting second-order polynomial were r^2 = 0.51, $rmse$ = 0.2648 m^{-1}, and mae = 0.1846 m^{-1} with a $mape$ of 50.14%.

3.3.6 Fine-Tuning of the Algorithm

The preliminary index-based algorithm (equation 3.15) was subjected to an iterative refinement process to assess whether alternative combinations of wavelengths could yield improved regression performance. The objective was to optimise the selection of λ_1, λ_2, and λ_3 by minimising the $rmse$ in the retrieval of a_{cdom}^{440} against in-situ observations. The entire formulation dataset ($n = 850$) was employed in this analysis to ensure that the resulting algorithm remains robust across a wide range of optical water types, including those dominated by phytoplankton or suspended sediments that could potentially obscure CDOM signals.

In the first iteration, λ_2 and λ_3 were fixed at their original values (465 nm and 575 nm, respectively), while λ_1 was varied across the visible spectrum. The $rmse$ values for each λ_1 candidate were computed, and the lowest error was observed at 414 nm, slightly red-shifted compared to the initially selected 400 nm (Figure 3.4a). Therefore, 412 nm, a standard waveband on most satellite sensors (e.g., MODIS and Sentinel-3 OLCI), was selected as the revised λ_1.

In the second step, λ_1 was fixed at 412 nm and λ_3 at 575 nm, while λ_2 was varied. The

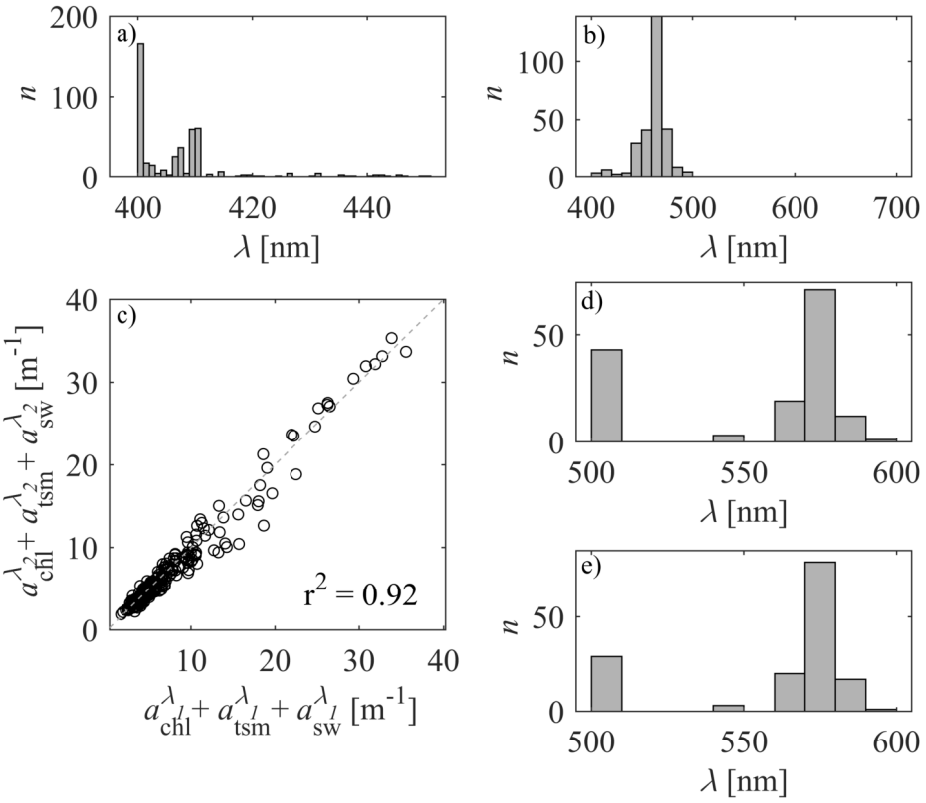

Figure 3.2: The results of the partial differential analysis for wavelength identification of the R_{rs} index. a) The histogram indicating the wavelength at which the maximum change in $\frac{\partial R_{rs}}{\partial a_{cdom}}$ was observed, b) the histogram indicating the wavelengths at which the cumulative absorption of Chl-a, TSM and seawater molecules showed a minimum difference against that at 400 nm. c) the scatter plot between the cumulative absorption of Chl-a, TSM and seawater molecules at λ_1 (400 nm) and λ_2 (465 nm) with the coefficient of determination (r^2) between them. d) & e) The histogram representing the wavelengths at which minimum variation to $\frac{\partial R_{rs}}{\partial a_{chl}}$ and $\frac{\partial R_{rs}}{\partial a_{tsm}}$ was observed.

minimum $rmse$ was recorded at 459 nm (Figure 3.4b). However, considering sensor availability and practical implementation, the nearest operational bands 443 nm and 490 nm were evaluated. Between these, 490 nm was chosen for λ_2 as it exhibited lower $rmse$ and minimal interference from Chl-a absorption. Furthermore, a strong correlation ($r^2 = 0.97$) was observed between the cumulative absorption of Chl-a, TSM, and seawater molecules at 412 and 490 nm (Figure 3.4c), which supports the selection of these wavelengths.

In the final iteration, with $\lambda_1 = 412$ nm and $\lambda_2 = 490$ nm fixed, λ_3 was varied from

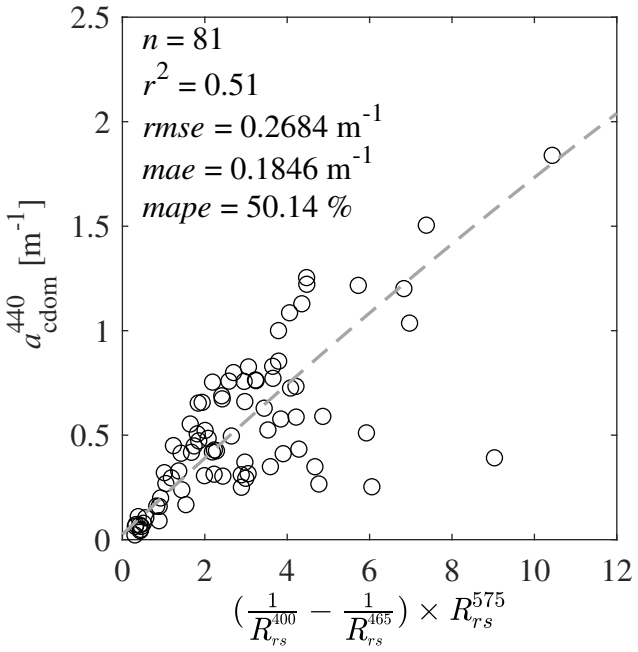

Figure 3.3: The regression fit between in-situ a_{cdom}^{440} against the R_{rs} index, i.e., $\left(\frac{1}{R_{rs}^{400}} - \frac{1}{R_{rs}^{465}}\right) \times R_{rs}^{575}$ with statistical performance metrics.

400 to 700 nm. The analysis revealed that 594 nm yielded the lowest $rmse$ (Figure 3.4d). However, considering the availability of satellite bands and the need to reduce the influence of backscattering from Chl-a and TSM, 560 nm was chosen as the revised λ_3 due to its comparable error and better compatibility with operational sensors such as Sentinel-3 OLCI.

Thus, the refined three-band CDOM index, optimised through iterative wavelength selection, was expressed as,

$$a_{\text{cdom}} \propto \left(\frac{1}{R_{rs}^{412}} - \frac{1}{R_{rs}^{490}}\right) \times R_{rs}^{560} \tag{3.16}$$

This revised formulation is expected to provide improved robustness and accuracy across optically diverse estuarine and coastal waters.

The optimised R_{rs} index was then regressed over the subset of the formulation dataset, where CDOM contributed to at least 33% of the OAC absorption budget. The second-order best-fit polynomial is given as follows,

$$a_{cdom}^{440} = -0.01368x^2 + 0.102x + 0.02295 \tag{3.17}$$

where $x = \left(\frac{1}{R_{rs}^{412}} - \frac{1}{R_{rs}^{490}}\right) \times R_{rs}^{560}$

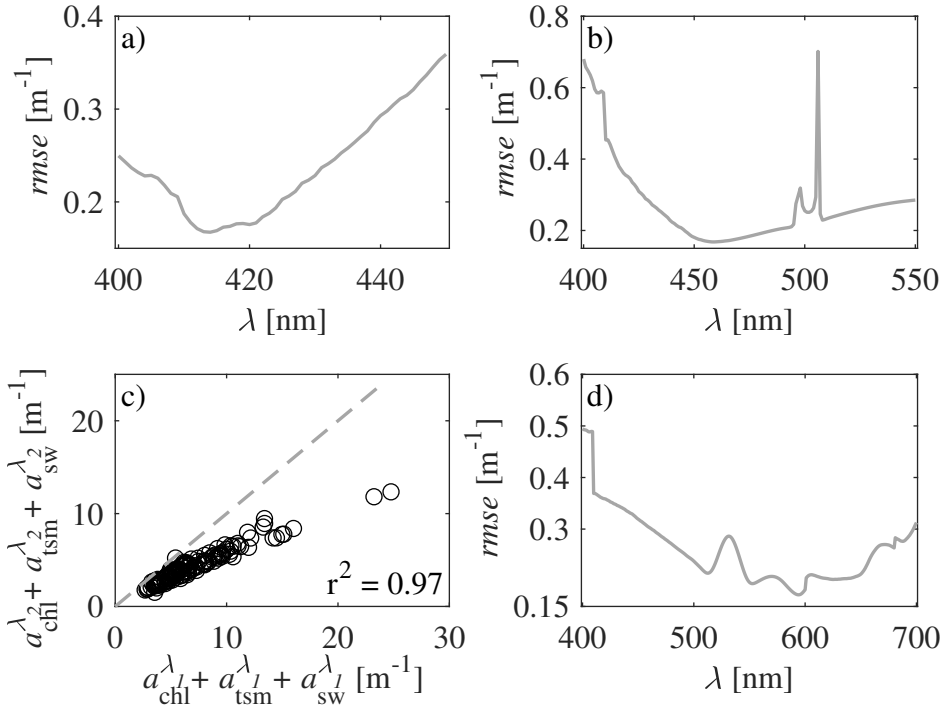

Figure 3.4: The $rmse$ resulting from the iteration analysis for fine-tuning the index when a) λ_1, b) λ_2 and d) λ_3 are varied, respectively. c) The scatterplot between the cumulative absorption of Chl-a, TSM and seawater for fine-tuned λ_1 and λ_2 set at 412 nm and 490 nm, respectively.

The statistics of the curve fitting were r^2 of 0.81, $rmse$ of 0.1116 m^{-1}, and mae of 0.07817 m^{-1} (Figure 3.5). The validation of the formulated retrieval algorithm (Equation 3.17) is discussed in section 3.4.

3.3.7 Existing widely used CDOM retrieval algorithms

In addition to the developed algorithm, the following algorithms were evaluated using the validation dataset encompassing the diverse optical water types usually observed in estuarine and coastal waters globally. The algorithms were grouped according to their approach into empirical, semi-empirical and SAA.

In analysis, the empirical and semi-empirical algorithms were,

(a) Band-ratio algorithms: The equation of the BR algorithm developed for the coastal waters

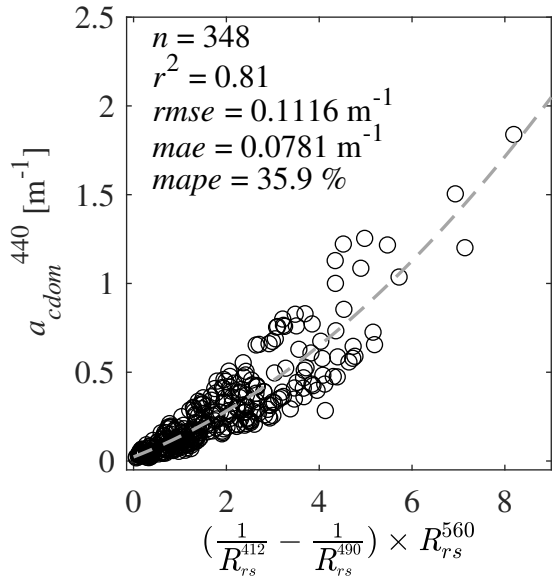

Figure 3.5: Regression fit between in-situ a_{cdom}^{440} and the R_{rs} index $\left(\frac{1}{R_{rs}^{412}} - \frac{1}{R_{rs}^{490}}\right) \times R_{rs}^{560}$, along with statistical performance metrics.

of northeastern United States of America (Mannino et al., 2008) was as follows,

$$a_{cdom}^{443} = \frac{ln\left[\frac{\frac{R_{rs}^{\lambda_1}}{R_{rs}^{\lambda_2}} - 0.4363}{0.2221}\right]}{(-13.26)} \tag{3.18}$$

where, λ_1 and λ_2 were centred around 490 nm and 560 nm for OLCI retrievals, while it was 488 nm and 551 nm for MODIS retrievals. This equation is here onwards referred to as M08.

The only BR algorithm for global coastal waters was formulated and validated on the NOMAD dataset. The equation of the algorithm was of the following form,

$$a_{cdom}^{443} = 0.00129 + 0.6543\left[\frac{R_{rs}^{\lambda_1}}{R_{rs}^{\lambda_2}}\right] \tag{3.19}$$

where λ_1 and λ_2 were centred around 490 nm and 665 nm for OLCI retrievals, while it was 488 nm and 667 nm for MODIS retrievals. The equation shall be referred to as TS11.

(b) Linear regression algorithms: Empirical algorithms like the multiple linear regression (MLR) algorithm developed by Mannino et al. (2014) showed great success in the coastal

waters northeastern United States of America. The equation was of the following form,

$$\ln(a_{cdom}^{440}) = \beta_0 + \beta_1 \times \ln(R_{rs}^{\lambda_1}) + \beta_2 \times \ln(R_{rs}^{\lambda_2}) \tag{3.20}$$

where the regression coefficients were β_0 = -3.664, β_1 = -1.291, β_2 = 1.105 for MODIS retrievals for the wavelengths λ_1 = 443 nm and λ_2 = 547 nm while the regression coefficients were β_0 = -3.379, β_1 = -1.1513, β_2 = 1.006 for the wavelengths λ_1 = 443 nm and λ_2 = 555 nm for OLCI retrievals.

Another algorithm developed with the MLR approach (Aurin et al., 2018) was trained on global coastal and open ocean waters. The equation is of the following form,

$$\ln(a_{cdom}^{440}) = \beta_0 + \beta_1 \times \ln(R_{rs}^{\lambda_1}) + \beta_2 \times \ln(R_{rs}^{\lambda_2}) + \beta_3 \times \ln(R_{rs}^{\lambda_3}) + \beta_4 \times \ln(R_{rs}^{\lambda_4}) \tag{3.21}$$

where the coefficients and wavelengths were regressed for MODIS and SeaWiFS sensor data. For retrieval from MODIS, the regressed wavelengths were λ_1 = 443 nm, λ_2 = 488 nm, λ_3 = 531 nm and λ_4 = 547 nm with the regressed coefficients β_0 = -3.287, β_1 = -0.727, β_2 = -0.922, β_3 = 1.278, and β_4 = 0.261. Aurin et al. (2018) also regressed the retrieval algorithm on SeaWiFS sensor data, with the coefficients taking the values β_0 = -6.410, β_1 = 0.743, β_2 = -0.145, β_3 = -0.367, and β_4 = 0.547 for the wavelengths λ_1 = 443 nm, λ_2 = 490 nm, λ_3 = 510 nm and λ_4 = 555 nm. While applying the same to OLCI sensor data, we consider λ_4 as 560 nm. The algorithm was tested for its application in just the coastal waters of the validation dataset. It is referred to henceforth as A18, with subscripts S and M indicating SeaWiFS and MODIS, the satellite bands considered in the application.

(c) Machine learning algorithms: This study employed and adapted two ML algorithms to model the relationship between in-situ measurements and hyperspectral R_{rs} spectra.The first model is a support vector regression algorithm developed by Zhao et al. (2018) for the turbid waters of the Pearl River Estuary. In this study, the algorithm was re-implemented using the formulation dataset in MATLAB (v2023b). The regression was performed using the fitrsvm function with Sequential Minimal Optimisation as the solver. The Support Vector Regression was configured with a Gaussian kernel function, a kernel scale of 0.25, and a box constraint of 0.11. These parameters enabled the model to determine the optimal hyperplane that best represents the continuous relationship between the in-situ measurements and the hyperspectral R_{rs} data. This implementation is referred to as Z18 throughout the thesis.

The second algorithm used for comparative evaluation is the Gaussian Process Regression model developed by Ruescas et al. (2018). This algorithm previously demonstrated superior performance over regularised linear regression, random forest regression, kernel ridge regression, and other Support Vector Regression approaches when applied to simulated Sentinel-2 and Sentinel-3 OLCI data. The Gaussian Process Regression model leverages various kernel functions to capture complex non-linear relationships between in-situ measurements and hyperspectral R_{rs} spectra. In this study, the algorithm was retrained on the formulation dataset using MATLAB's *fitrgp* function with default settings. This implementation is referred to as R18.

(d) Semi-analytical algorithms: SAA estimate specific inherent or apparent optical properties of the water column using analytical models. One of the most widely used methods in this category is the QAA, initially developed by Lee et al. (2002). These have been extensively refined to enhance the retrieval of total absorption and backscattering coefficients in turbid coastal waters.

The latest version, referred to in this thesis as QAAv6, is presented step by step in Table 3.2. In this version, the reference wavelengths λ_0 and λ_r are set to 560 nm and 674 nm, respectively, for OLCI retrievals, and to 551 nm and 667 nm for MODIS retrievals.

Another SAA used in the comparative analysis is the model developed by Loisel et al. (2014). This method first estimates the diffuse attenuation coefficient of the water column and then applies a theoretical relationship to derive the absorption properties of CDOM in coastal waters. The equation used in this model is as follows:

$$a_{cdom}^{412} = 10^{0.15482\times(\log_{10}(X))^2+1.1939\times(\log_{10}(X))+0.0689} \tag{3.22}$$

where, $X = \Delta k_d(\lambda_1 - \lambda_2) - \Delta_p(\lambda_1 - \lambda_2)$

$$\Delta k_d(\lambda_1 - \lambda_2) = 10^{a\times(\log_{10}(Y))^3+b\times(\log_{10}(Y))^2+c\times(\log_{10}(Y))+d} \tag{3.23}$$

$$\Delta_p(\lambda_1 - \lambda_2) = 10^{e\times(\log_{10}(\Delta k_d(\lambda_1-\lambda_2)))^2+f\times\log_{10}(\Delta k_d(\lambda_1-\lambda_2))+g} \tag{3.24}$$

and $Y = \frac{R_{rs}^{\lambda_1}}{R_{rs}^{\lambda_2}}$

where, λ_1 and λ_2 were centred around 412 nm and 560 nm for OLCI retrievals, while it was 412 nm and 551 nm for MODIS retrievals. The coefficients were a = -0.0634808, b = 0.254858, c = - 1.223848, d = - 0.886471, e = -0.009, f = 1.147 and g = - 0.26. The algorithm equation shall be referred to as L14 in the thesis.

Table 3.2: Stepwise computation of the Quasi-Analytical Algorithm (QAAv6) for deriving absorption and backscattering coefficients.

Step	QAAv6 Computations	
1	$r_{rs}^{\lambda} = \frac{R_{rs}^{\lambda}}{0.52+0.17\times R_{rs}^{\lambda}}$	
2	$u^{\lambda} = \frac{-g_0+\sqrt{g_0^2+4g_1 r_{rs}^{\lambda}}}{2g_1}$, where $g_0 = 0.089$, $g_1 = 0.1245$	
3	If $R_{rs}^{670} < 0.0015$ sr^{-1}	If $R_{rs}^{670} \geq 0.0015$ sr^{-1}
	$\chi = \log\left(\frac{r_{rs}^{443}+r_{rs}^{490}}{r_{rs}^{\lambda_0}+5\frac{r_{rs}^{670}}{r_{rs}^{490}}r_{rs}^{670}}\right)$ $a(\lambda_0) = a_w^{\lambda_0} + 10^{-1.146-1.366\chi+0.469\chi^2}$ $b_{bp}(\lambda_0) = \frac{u(\lambda_0)a(\lambda_0)}{1-u(\lambda_0)} - b_{bw}(\lambda_0)$	– $a(\lambda_r) = a_w^{\lambda_r} + 0.39\left(\frac{R_{rs}^{670}}{R_{rs}^{443}+R_{rs}^{670}}\right)^{1.14}$ $b_{bp}(\lambda_r) = \frac{u(\lambda_r)a(\lambda_r)}{1-u(\lambda_r)} - b_{bw}(\lambda_r)$
4	$\gamma = 2\left(1 - 1.2e^{-0.9\frac{r_{rs}^{443}}{r_{rs}^{\lambda_0}}}\right)$	
5	$b_{bp}(\lambda) = b_{bp}^{\lambda_0}\left(\frac{\lambda_0}{\lambda}\right)^{\gamma}$	$b_{bp}(\lambda) = b_{bp}(\lambda_r)\left(\frac{\lambda_r}{\lambda}\right)^{\gamma}$
6	$a(\lambda) = (1-u(\lambda))\left(\frac{b_{bw}(\lambda)+b_{bp}(\lambda)}{u(\lambda)}\right)$	
7	$\zeta = 0.74 + \frac{0.2}{0.8+\frac{r_{rs}(443)}{r_{rs}(\lambda_0)}}$ $S = 0.015 + \frac{0.002}{0.6+\frac{r_{rs}(443)}{r_{rs}(\lambda_0)}}$ $\xi = e^{S(442.5-412.5)}$	
8	$a_{CDOM}(443) = \frac{a(412)-\zeta a(443)}{\xi-\zeta} - \frac{a_w(412)-\zeta a_w(443)}{\xi-\zeta}$	

3.4 Results

3.4.1 In-situ Validation of the Developed Algorithm Across Diverse Optical Conditions

The semi-analytical CDOM retrieval algorithm (Equation 3.17) was rigorously evaluated using a comprehensive global validation dataset comprising 649 data points. This dataset spans a wide range of optically diverse water types where the contribution of CDOM to the total OAC absorption budget varies extensively, ranging from as low as 5% to as high as 95% (Figure 3.6). The in-situ measurements of CDOM absorption at 440 nm, a_{CDOM}^{440}, within the validation dataset range from 0.0056 m^{-1} to 1.1843 m^{-1}, with an average value of 0.1878 m^{-1}.

Application of the algorithm to this global dataset resulted in a strong correlation between observed and estimated a_{cdom}^{440}, with a $r^2 = 0.64$, indicating that 64% of the variance in CDOM absorption is captured by the model (Table 3.3). Error statistics included a $rmse$ of 0.1039 m^{-1}, mae of 0.0746 m^{-1}, and a low bias of -0.0021 m^{-1}, demonstrating minimal systematic deviation. The $mape$ of 51.96% reflects the significant heterogeneity in optical properties across the validation dataset.

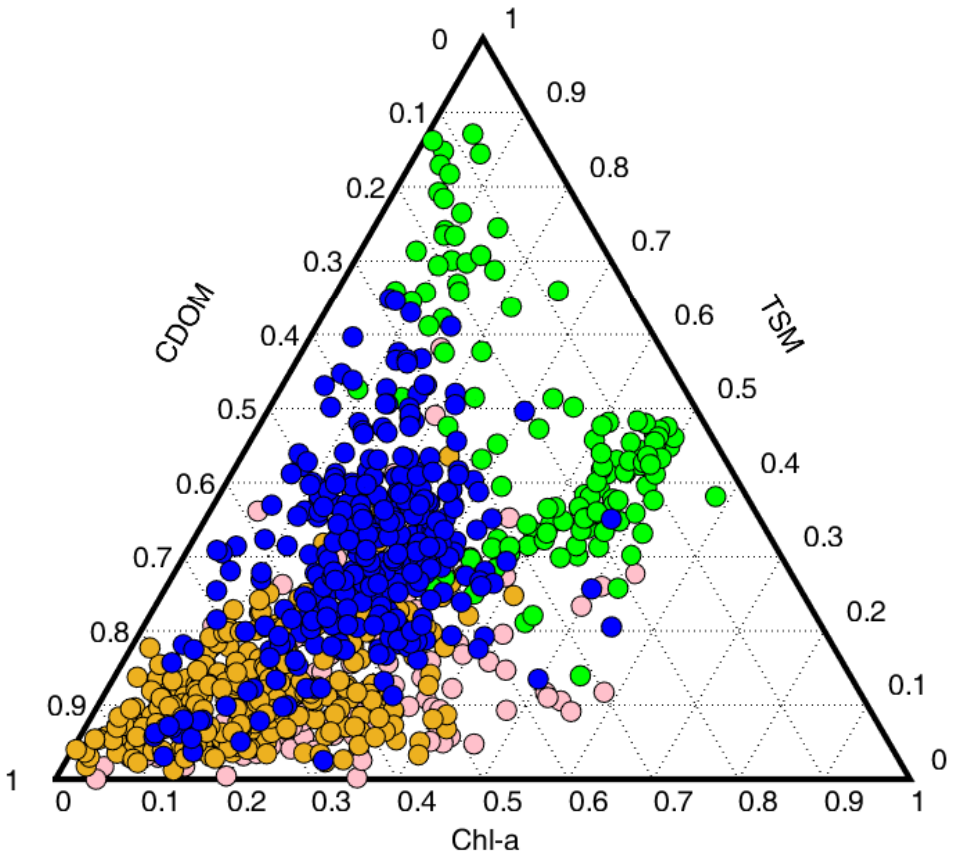

Figure 3.6: The ternary plot depicting the contribution of each OAC to total absorption (absorption budget) at 440 nm for MZE (green circles), CDB (blue circles), GoM (yellow circles) and the other global data points (pink circles).

To further evaluate regional performance, the algorithm was applied to four distinct subsets characterised by differing optical regimes:

- Gulf of Mexico (GoM): This region's waters ($n = 261$) are typically rich in CDOM, with CDOM contributing approximately 86% to the total absorption budget. The in-situ a_{cdom}^{440}

ranged from 0.0192 m^{-1} to 1.1843 m^{-1}, averaging 0.1940 m^{-1}. The algorithm yielded an improved $r^2 = 0.77$, $rmse$ of 0.0876 m^{-1}, mae of 0.0604 m^{-1}, bias of -0.0047 m^{-1}, and a relatively low $mape$ of 36.56%, confirming its effectiveness in CDOM-dominated waters.

- Chesapeake-Delaware Bay (CDB): Estuarine waters here ($n = 77$) show greater optical complexity with CDOM averaging 45% of total absorption. a_{cdom}^{440} values range between 0.05 and 0.5499 m^{-1}, with a mean of 0.2356 m^{-1}. The algorithm performance was satisfactory with $r^2 = 0.62$, $rmse$ of 0.1040 m^{-1}, mae of 0.0870 m^{-1}, bias of -0.0376 m^{-1}, and $mape$ of 39.43%. The negative bias indicates a slight underestimation, potentially due to competing absorption by other OACs.

- Mandovi–Zuari Estuarine System (MZE): In these tropical estuarine and adjacent coastal waters ($n = 82$), particulate matter and phytoplankton absorption dominate, with CDOM contributing only about 18% to total absorption. In-situ a_{cdom}^{440} ranges from 0.0476 to 0.918 m^{-1}, with a mean of 0.3176 m^{-1}. The algorithm achieved $r^2 = 0.61$, $rmse$ = 0.1283 m^{-1}, mae = 0.1091 m^{-1}, bias = 0.0615 m^{-1}, and $mape$ = 43.75%. The positive bias suggests a tendency to overestimate CDOM absorption in particle-rich, optically complex waters.

- CDOM-Rich Subset: Focusing on samples where CDOM contributed at least 33% of the absorption budget ($n = 130$), the algorithm demonstrated its best performance, achieving $r^2 = 0.78$, $rmse$ = 0.1037 m^{-1}, mae = 0.0735 m^{-1}, bias = –0.0051 m^{-1}, and $mape$ = 35.04%.

Overall, the algorithm exhibits consistent and reliable performance across a wide range of coastal and estuarine optical regimes. The modest variations in error statistics across regions reflect the natural complexity and variability of OACs in these environments. These results underscore the algorithm's robustness and applicability for accurately retrieving CDOM absorption from spectral R_{rs} in both particle-dominated and CDOM-rich waters.

Table 3.3: A comparison of the developed semi-analytical algorithm and other widely-used algorithms processed using in-situ data. The statistics in bold indicate the best performance of the parameter over the dataset.

Type	**Algorithm name**	**Dataset**	n	r^2	$rmse$ [$\mathbf{m^{-1}}$]	mae [$\mathbf{m^{-1}}$]	$bias$ [$\mathbf{m^{-1}}$]	$mape$ [**%**]
SAA	Eq. 3.17	Global	649	**0.64**	**0.1039**	**0.0746**	0.0021	**51.96**
		GoM	261	0.77	**0.0876**	0.0604	**-0.0047**	36.56
		CDB	77	**0.62**	0.1040	0.0870	**-0.0376**	39.43
		MZE	82	**0.61**	**0.1283**	**0.1091**	0.0615	43.75
		CDOM-rich	130	0.78	0.1037	0.0735	0.0051	35.04
BR	M08	Global	631	0.52	0.1346	0.0818	0.0540	57.06
		GoM	261	0.64	0.1572	0.0857	-0.0687	38.01
		CDB	75	0.50	0.1025	0.0853	-0.0792	**34.42**
		MZE	82	0.36	0.1729	0.1208	-0.1054	43.28
	TS11	Global	596	0.30	0.2436	0.1433	-0.0852	53.25
		GoM	261	**0.82**	0.0940	**0.0588**	-0.0371	**30.74**
		CDB	75	0.45	0.1480	0.1093	0.0748	50.69
		MZE	82	0.19	0.4592	0.3725	0.3559	146.05
MLR	$A18_S$	Global	615	0.01	0.6459	0.1567	-0.0023	97.5
		GoM	261	0.39	0.1742	0.1041	-0.0923	46.49
		CDB	77	0.02	0.1656	0.1336	-0.0877	55.11
		MZE	82	0.01	0.742	0.2834	-0.0251	104.38
	$A18_M$	Global	631	0.50	0.1391	0.0851	-0.0642	43.99
		GoM	261	0.72	0.1978	0.0849	-0.0751	33.39
		CDB	75	0.48	0.1125	0.0946	-0.0906	39.12
		MZE	82	0.26	0.1921	0.1373	-0.1248	37.45

Table 3.3 continued from previous page

Type	**Algorithm name**	**Dataset**	n	r^2	$rmse$ **[m^{-1}]**	mae **[m^{-1}]**	$bias$ **[m^{-1}]**	$mape$ **[%]**
MLR	M14	Global	608	0.46	0.1250	0.0779	0.0332	48.31
		GoM	261	0.73	0.1292	0.0709	-0.0497	32.75
		CDB	58	0.37	0.0977	0.0837	-0.0656	37.48
		MZE	82	0.23	0.1623	0.1135	-0.0673	34.43
ML	Z18	Global	649	0.30	0.1456	0.1051	0.0250	94.99
		GoM	261	0.32	0.1599	0.1060	-0.0347	120.63
		CDB	77	0.37	**0.0928**	**0.0674**	-0.0473	34.44
		MZE	82	0.33	0.1582	0.1094	**-0.0412**	37.46
	R18	Global	649	0.28	0.2642	0.1869	-0.1382	71.94
		GoM	261	0.59	0.1541	0.1136	0.0797	119.32
		CDB	77	0.01	0.1263	0.1008	-0.0460	49.23
		MZE	82	0.24	0.5079	0.4253	0.4028	167.05
SAA	QAAv6	Global	519	0.36	0.1878	0.1135	**0.0011**	76.11
		GoM	223	0.73	0.1185	0.0840	-0.0554	51.35
		CDB	57	0.61	0.0972	0.0832	-0.0498	45.79
		MZE	82	0.18	0.3508	0.2130	0.1524	81.14
	L14	Global	344	0.53	0.1912	0.1311	-0.0236	45.11
		GoM	45	0.81	0.3390	0.2211	-0.1945	26.02
		CDB	60	0.55	0.1776	0.1528	-0.1068	44.14
		MZE	82	0.62	0.1569	0.1232	0.0674	40.76

3.4.2 Comparison against Published Algorithms

The SAA developed in this study (Equation 3.17) consistently outperformed a range of widely used CDOM retrieval algorithms, including BR, MLR, ML, and semi-analytical models, when tested against the same comprehensive in-situ dataset (Table 3.3). It demonstrated the

highest r^2 alongside the lowest $rmse$, mae, and $mape$, underscoring its robustness and accuracy in optically complex waters.

The relatively low r^2 values exhibited by other algorithms on the global dataset highlight the lack of universally applicable CDOM retrieval methods capable of effectively handling the extensive optical variability present in coastal and estuarine waters worldwide. Given the pronounced spatial heterogeneity and varying dominance of OACs such as Chl-a, TSM, and CDOM in different regions, it is imperative to evaluate algorithm performance on region-specific subsets with distinct optical characteristics.

Analysis across regional subsets revealed that only the developed algorithm maintained an r^2 above 0.6 consistently across all optical regimes (Table 3.3). In contrast, MLR and ML algorithms exhibited suboptimal performance irrespective of optical complexity, suggesting limitations in their generalisability across diverse water types. BR algorithms showed improved accuracy in the specific optical regimes for which they were originally designed but failed to capture the complex interactions in turbid estuarine waters such as the MZE, reflected by markedly reduced r^2 values.

The QAAv6 exhibited similar behaviour, achieving reasonable accuracy in CDOM-rich waters but performing poorly in regions where particulate absorption and scattering dominate. This trend was particularly evident in the MZE subset (r^2 = 0.18; $rmse$ = 0.3508 m^{-1}), where Chl-a and TSM strongly influence the optical signal.

L14 algorithm produced relatively favourable r^2 values; however, its retrieval errors were larger across all datasets, indicating limited practical reliability for precise CDOM estimation in optically diverse coastal environments.

Overall, the developed algorithm's superior performance is attributed to its tailored semi-analytical formulation that effectively isolates CDOM absorption signals amidst competing optical effects from particulate and dissolved constituents, thereby ensuring robustness across variable coastal optical conditions.

3.4.3 Validation of Satellite-Retrieved CDOM

The developed algorithm was further validated using remote sensing reflectance data acquired from two prominent satellite sensors: the OLCI onboard Sentinel-3 ($n = 19$) and the MODIS onboard Aqua ($n = 80$) (Table 3.4).

For OLCI-derived data, the developed algorithm again demonstrated superior performance relative to all other evaluated methods. It achieved the highest r^2 of 0.89, along with the lowest $mape$ of 52.94%, confirming its capability to reliably retrieve CDOM absorption in turbid and optically complex coastal waters from satellite platforms. While the $rmse$, mae, and bias

were higher compared to in-situ validations, an expected outcome due to inherent atmospheric correction uncertainties and spatial mismatches, the algorithm's accuracy remained consistently better than alternative approaches.

MODIS-based validation utilised a larger sample size and exhibited generally lower retrieval errors, with the developed algorithm yielding an r^2 of 0.72 and a $mape$ of 42.46%. Other algorithms, such as TS11 and M14, produced marginally lower $rmse$ and mae values; however, these improvements were minimal (on the order of 10^{-2} m^{-1}) and accompanied by poorer correlation coefficients ($r^2 < 0.6$). Notably, the developed algorithm consistently delivered the best balance between correlation and error metrics across both satellite sensors.

Despite a slight tendency to underestimate in-situ a_{cdom}^{440} values, the developed algorithm's reliable performance across multiple satellite platforms reinforces its potential as a robust tool for operational monitoring of CDOM in complex coastal and estuarine waters. This capability is critical for enhancing the accuracy of bio-optical remote sensing products used in ecological assessments, water quality monitoring, and climate-related studies.

3.5 Discussion

Estuarine and coastal environments are governed by a complex interplay of physical, chemical, and biogeochemical processes that result in significant spatial and temporal variability in the concentrations and compositions of OACs. These variations manifest over multiple temporal scales, including seasonal cycles, tidal fluctuations, and diurnal changes, and may arise from both interdependent and independent mechanisms (Jafar-Sidik et al., 2017; Uudeberg et al., 2019). The inherent nonlinear optical behaviour of such waters means that even subtle changes in individual OACs can produce marked shifts in the spectral R_{rs}, complicating the remote sensing retrieval of water quality parameters (Ashphaq et al., 2023; Topp et al., 2020).

In many datasets lacking direct turbidity measurements, the diffuse attenuation coefficient of downwelling irradiance at 490 nm (k_d^{490}) is widely used as a reliable proxy for turbidity (Shi and Wang, 2010). Elevated values of k_d^{490} correlate with more turbid, optically dense waters, whereas lower values indicate clearer conditions. Observed in-situ k_d^{490} values span broad ranges: from 0.14 to 2.51 m^{-1} in the CDB, from 0.019 to 3.39 m^{-1} in the MZE, and from 0.01 to 2.62 m^{-1} near the Mississippi and Atchafalaya river mouths in the GoM (Schaeffer et al., 2011). Such variability is characteristic of the diverse optical environments typically encountered in global estuarine and coastal systems.

The superior performance of the newly developed SAA, compared to established BR, ML, and semi-analytical methods, across these varied optical regimes suggests its strong potential for broad application in optically complex coastal waters. Attempts to retrain ML algorithms across

Table 3.4: A comparison of the developed semi-analytical algorithm and other widely used algorithms for OLCI and MODIS match-ups. The statistics in bold indicate the best performance of the parameter for the sensor.

Sr. No.	**Satellite sensor**	**Algorithm name**	n	r^2	$rmse$ **[m^{-1}]**	mae **[m^{-1}]**	$bias$ **[m^{-1}]**	$mape$ **[%]**
1	OLCI	Eq. 3.17	19	**0.89**	**0.2686**	**0.1918**	**-0.1899**	**52.94**
		M08	19	0.80	0.2719	0.1969	-0.1969	76.20
		TS11	19	0.76	0.4002	0.3776	0.3776	96.96
		A18$_S$	19	0.52	0.3518	0.2581	-0.2572	72.09
		M14	19	0.86	0.2907	0.2093	-0.2090	59.06
		Z18	19	0.58	0.2767	0.2352	-0.2259	364.40
		R18	19	0.01	0.3508	0.2669	0.1806	624.89
		QAAv6	19	0.73	0.2883	0.2161	-0.2161	83.91
		L14	19	0.86	0.2650	0.1842	-0.1836	56.31
2	MODIS	Eq. 3.17	80	**0.72**	0.1240	0.0805	-0.0206	**42.46**
		M08	70	0.53	0.1124	0.0763	-0.0590	44.45
		TS11	70	0.23	0.1678	0.0910	0.0118	81.48
		A18$_M$	70	0.49	0.1108	0.0781	-0.0579	43.20
		M14	70	0.44	**0.1016**	**0.0703**	-0.0318	42.63
		Z18	80	0.26	0.1135	0.0788	**0.0052**	97.35
		R18	80	0.44	0.1327	0.1046	0.0109	120.52
		QAAv6	70	0.52	0.1257	0.1063	-0.0850	75.53
		L14	70	0.51	0.2976	0.1387	-0.0067	51.01

the entire turbidity gradient generally resulted in degraded predictive performance, highlighting inherent limitations of these methods for generalised global application. BR algorithms, such as those developed by Mannino et al. (2008) and Tiwari and Shanmugam (2011), performed well only within the specific optical regimes for which they were designed, but their accuracy deteriorated substantially in turbid waters dominated by Chl-a and suspended sediments.

The robustness of developed algorithm across a wide range of optical water types indicates that it effectively captures the nonlinear interactions between multiple OACs influencing R_{rs}. In contrast, other algorithms fail in optically complex environments such as the MZE system and other geographically diverse coastal regions, including waters off Australia, Korea, and the Indian coasts off Gujarat and Odisha (Najah and Al-Shehhi, 2021). For example, the SAA proposed by Loisel et al. (2014) showed limited performance; although it estimates k_d^{490} from spectral R_{rs}, the empirical relationship linking k_d^{490} to a_{cdom}^{440} was not consistently valid across diverse optical regimes. This illustrates the challenges of applying regional empirical models globally in optically heterogeneous waters.

To further explore the influence of OACs on spectral R_{rs}, a sensitivity analysis was performed using the GURTRAM radiative transfer model (Menon, 2004) with IOCCG-simulated inherent optical property datasets. This analysis encompassed globally representative OAC concentration ranges, a_{cdom}^{440} from 0.1 to 2 m^{-1}, Chl-a from 0.25 to 30 μg L^{-1}, and TSM from 0.25 to 15 mg L^{-1}. Under fixed Chl-a and TSM conditions, k_d^{490} exhibited a strong exponential dependence on CDOM absorption, described by the regression, $k_d^{490} = 0.7 \times e^{1.13 \times a_{cdom}^{440}}$ (Figure 3.7). This finding reinforces the dominant role of CDOM in modulating light attenuation in turbid and optically complex coastal waters.

Despite the spectral complexity arising from overlapping contributions of various OACs, the developed algorithm (Equation 3.17) demonstrated robust capability in retrieving the a_{cdom}^{440} across a broad spectrum of optical conditions. The algorithm's index is primarily sensitive to variations in the spectral R_{rs} driven by CDOM absorption, while incorporating methodological strategies to mitigate confounding effects from particulate constituents such as Chl-a and TSM.

To assess the spectral stability and suitability of the selected retrieval wavelength λ_3 under varying turbidity conditions, partial derivatives of modelled R_{rs} spectra were computed with respect to the absorption and backscattering coefficients of Chl-a and TSM, namely a_{chl}, $b_{b_{chl}}$, a_{tsm}, and $b_{b_{tsm}}$. Across all simulated scenarios, the inflexion points of these partial derivatives consistently occurred within the 560 to 580 nm spectral range (Figure 3.8), indicating that this region exhibits minimal sensitivity to variations in particulate OAC concentrations. This spectral characteristic supports the choice of 560 nm as the optimal wavelength for the index, striking a well-founded balance that maximises the CDOM-specific signal while minimising

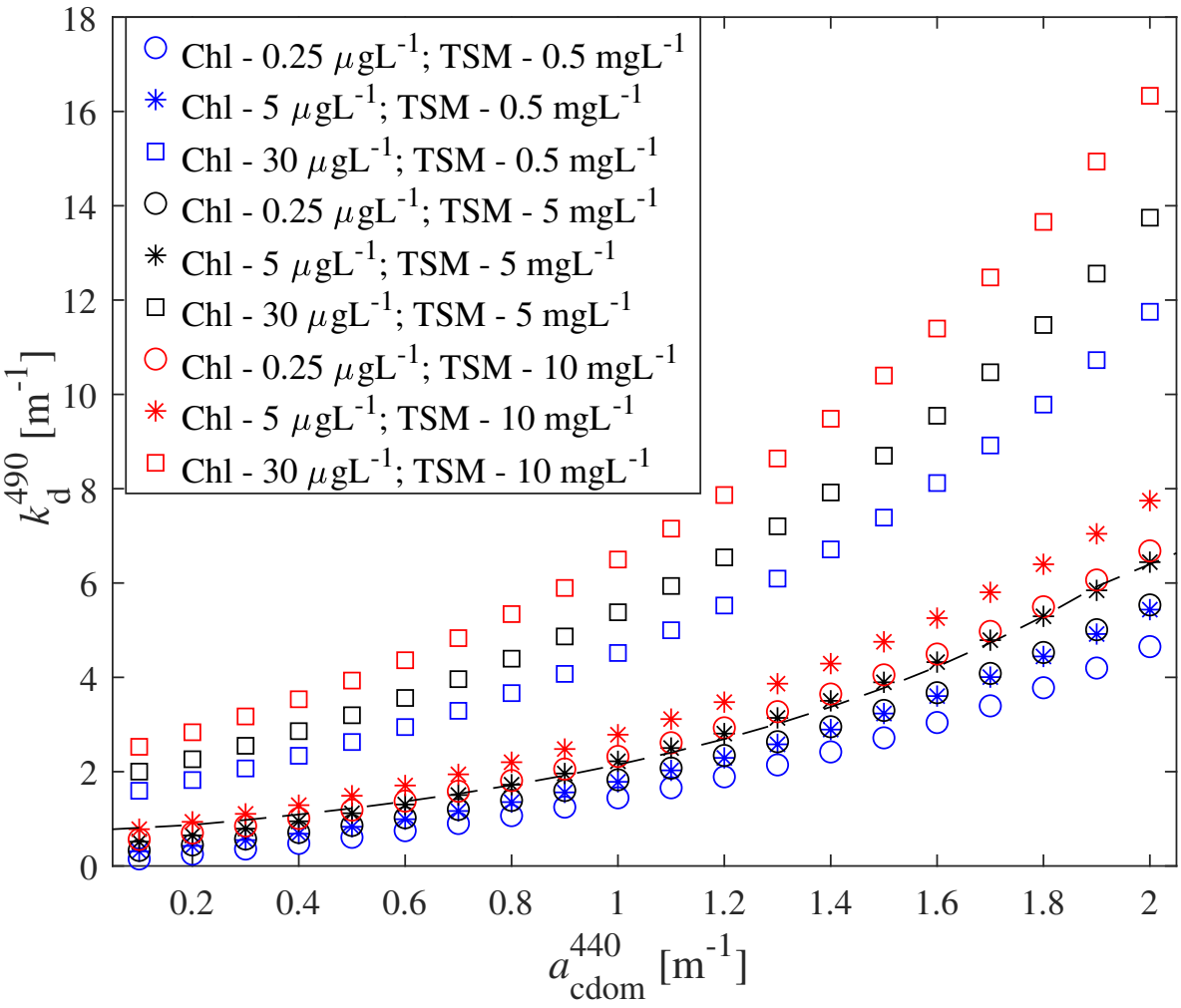

Figure 3.7: The scatter plot of simulated k_d^{490} from the sensitivity analysis conducted over varying OACs concentrations representative of the estuarine and coastal waters. The dotted line represents the average regression curve.

interference from Chl-a and TSM. Such selection enhances the algorithm's ability to effectively isolate CDOM absorption features within the complex optical environment of estuarine and coastal waters.

Although the developed algorithm successfully retrieves a_{cdom}^{440} in turbid waters, the retrieval index inherently responds to changes in the R_{rs} spectra caused by CDOM absorption. Given the partial susceptibility of the index to variations in particulate OACs, the approach was designed to minimise their influence on the attenuation and reflectance signals. To validate the global applicability of the chosen λ_3, the modelled spectral R_{rs} was further analysed by partial differentiation with respect to spectral a_{chl}, $b_{b_{chl}}$, a_{tsm}, and $b_{b_{tsm}}$. The resulting inflexion points

remained within the 560–580 nm window (Figure 3.8), confirming that the originally identified wavelength of 575 nm for the index is appropriate. The fine-tuned wavelength of 560 nm lies within this range, reinforcing the robustness of the index to delineate CDOM absorption signals from the composite R_{rs} spectra in optically complex waters.

Overall, these findings substantiate the efficacy of the selected index wavelengths in providing an accurate retrieval of CDOM absorption, even under challenging turbidity regimes dominated by multiple interacting OACs.

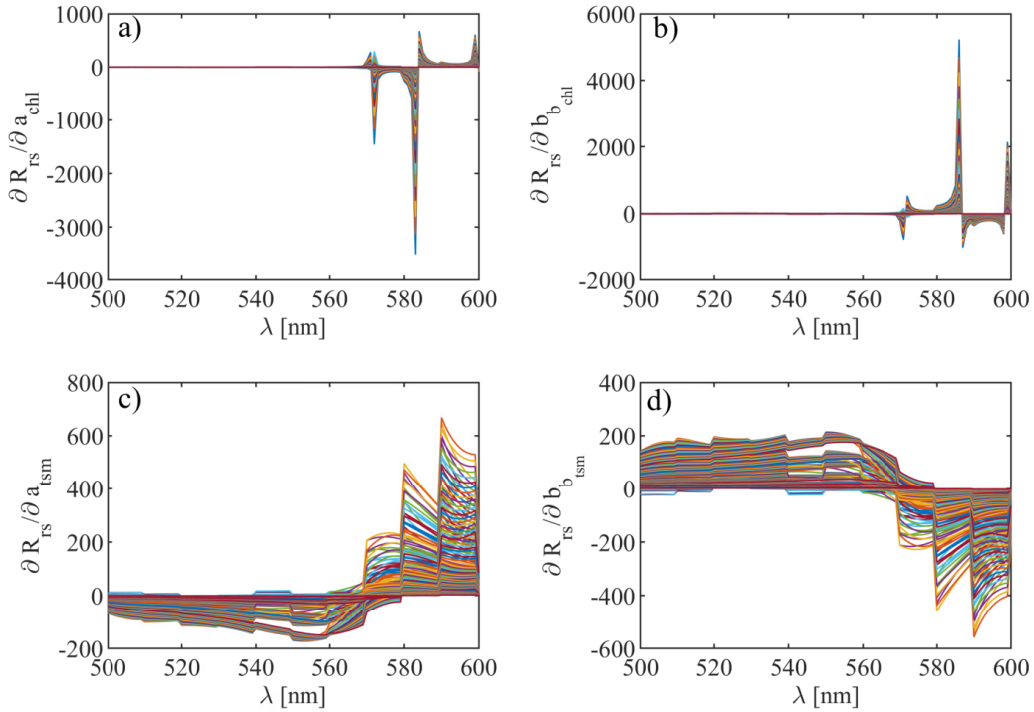

Figure 3.8: The partially differentiated modelled R_{rs} curves with respect to spectral a) a_{chl}, b) $b_{b_{chl}}$, c) a_{tsm} and d) $b_{b_{tsm}}$.

3.6 Conclusion

The dynamic variability and interdependent nature of OACs in estuarine and global coastal waters generate highly complex optical environments. Despite these inherent challenges, the developed SAA demonstrated significantly improved accuracy in estimating in-situ a_{cdom}^{440}, underscoring its robustness and potential for wide applicability in diverse aquatic environments. The effectiveness of the algorithm can be attributed to the following key findings,

a. Comprehensive validation across diverse optical conditions: The proposed algorithm was rigorously validated using a comprehensive global in-situ dataset covering a broad range of a_{cdom}^{440} values from 0.0056 m^{-1} to 1.1843 m^{-1}. Regionally, the absorption values spanned from 0.0476 m^{-1} to 0.918 m^{-1} in the MZE, 0.05 m^{-1} to 0.55 m^{-1} in the CDB, and 0.0192 m^{-1} to 1.1843 m^{-1} in the GoM. This dataset encompassed a wide spectrum of optical regimes where CDOM contributed between 5% and 95% of the total absorption at 440 nm. Additionally, the associated k_d^{490} ranged from 0.019 m^{-1} to 3.39 m^{-1}, effectively capturing the full range of turbidity conditions typically observed in estuarine and coastal waters. This extensive coverage ensures that the validation reflects global optical variability and complexity.

b. Superior performance in algorithm benchmarking: Across both the global coastal dataset and individual regional subsets (GoM, CDB, and MZE), the developed algorithm consistently achieved r^2 exceeding 0.6. It showed stronger correlations and lower retrieval errors compared to widely used BR, ML, and semi-analytical CDOM retrieval algorithms. While BR methods often exhibited limited applicability outside their development regions and ML approaches faced challenges in generalising to diverse optical regimes, the proposed algorithm maintained reliable performance across turbid and CDOM-dominated waters alike. Notably, retrieval errors decreased in CDOM-rich waters, affirming the algorithm's efficacy in isolating and quantifying CDOM contributions within the remote sensing reflectance spectra.

c. Enhanced satellite-based retrieval capability: Validation using satellite-derived remote sensing reflectance data from OLCI and MODIS sensors further corroborated the robustness of the developed algorithm. Although retrieval errors were marginally higher compared to those obtained from in-situ R_{rs} measurements-likely due to sensor noise and uncertainties inherent in atmospheric correction, the algorithm consistently outperformed traditional BR algorithms, ML models, and other SAA in satellite data applications. This finding highlights the potential for operational deployment of the algorithm in routine satellite-based monitoring of CDOM in optically complex coastal and estuarine waters.

Chapter 4

Seasonal Distribution of CDOM in Turbid Estuarine and Coastal Waters: Applications of the Algorithm

4.1 Introduction

Chromophoric dissolved organic matter (CDOM) is a fundamental component influencing the optical, biogeochemical, and ecological dynamics of estuarine and coastal waters worldwide. The distribution of CDOM in these waters exhibits pronounced spatial and temporal heterogeneity, driven by a complex interplay of natural and anthropogenic processes that modulate its sources, transport, transformation, and sinks (Castillo and Miller, 2008; Campanelli et al., 2017; Joshi et al., 2017). Understanding this variability is crucial as CDOM affects light penetration, photochemistry, carbon cycling, and ecosystem health in coastal zones, which are among the most productive and vulnerable environments on Earth.

Remote sensing has emerged as an indispensable tool for monitoring CDOM distribution and dynamics, providing synoptic spatial coverage and high-frequency temporal observations that are difficult to achieve through traditional in-situ sampling methods (Cao et al., 2018; Werdell et al., 2018; IOCCG, 2020). Satellite sensors, such as the Sentinel-3 Ocean and Land Colour Instrument (OLCI), Moderate Resolution Imaging Spectroradiometer (MODIS), and others, enable the consistent measurement of water-leaving reflectance (R_{rs}) under controlled viewing geometry, which can be exploited to retrieve CDOM absorption coefficients with improved accuracy (Vecchio and Subramaniam, 2004; Hu et al., 2004). In highly turbid estuarine waters, however, the retrieval of CDOM is complicated by the overlapping optical signals from other optically active constituents (OACs), such as phytoplankton pigments (e.g., chlorophyll-a) and suspended sediments.

In the preceding chapter, a semi-analytical algorithm was developed to reliably estimate the CDOM absorption coefficient at 440 nm (a_{cdom}^{440}) from R_{rs} spectra, explicitly addressing the optical complexity inherent to turbid estuarine and coastal waters. This algorithm incorporates strategies to minimise interference from particulate matter and pigments, enabling robust retrievals across a broad range of water types (Adhikari et al., 2023).

CDOM primarily originates from terrestrial sources, entering coastal waters through riverine discharge carrying organic matter from soils, wetlands, and decaying plant material (Bai et al., 2013; Shanmugam et al., 2016). These inputs often contain humic and fulvic acids that contribute to the characteristic absorption of CDOM in the ultraviolet (UV) and blue visible wavelengths (Coble, 2007). Estuarine wetlands and tidal marshes also export significant quantities of dissolved organic carbon (DOC) and CDOM, playing a critical role in coastal carbon budgets (Cao et al., 2018). Human activities such as urbanisation, agriculture, and industrial effluents further contribute to increased CDOM and DOC loads in many estuaries, intensifying pollution pressures and altering natural biogeochemical cycles (Menendez and Tzortziou, 2024; Fichot et al., 2023).

The transport and fate of CDOM within estuaries are governed by mixing dynamics, tidal exchange, photodegradation, microbial transformation, and sediment interactions (Castillo and Miller, 2008; Fasching et al., 2014). Seasonal freshwater inflows modulate the extent and intensity of CDOM plumes, which can be tracked remotely to infer freshwater discharge rates, pollutant dispersion, and carbon fluxes (Palacios et al., 2009; Tehrani et al., 2013). The relationship between CDOM and salinity often follows conservative mixing patterns, allowing remote sensing to effectively delineate freshwater influence and monitor estuarine circulation and plume behaviour (Binding and Bowers, 2003; Hu et al., 2004).

In addition to its ecological significance, CDOM influences the underwater light field by absorbing UV and visible radiation, thereby regulating photochemical reactions and primary productivity. CDOM-mediated UV attenuation protects aquatic organisms from harmful radiation, but also limits light availability for photosynthesis (Arrigo and Brown, 1996; Twardowski et al., 2004). Photodegradation of CDOM produces bioavailable substrates fuelling microbial respiration, which can lead to oxygen depletion and hypoxia in eutrophic estuaries (D'Sa and DiMarco, 2009; Fichot and Benner, 2012). Therefore, spatial and temporal monitoring of CDOM is essential for assessing water quality, ecosystem function, and hypoxia risk in coastal waters (Zhao et al., 2009).

Anthropogenic changes, including climate-driven alterations in precipitation patterns and river discharge, further complicate CDOM dynamics by modifying input loads, residence times, and degradation pathways (Fichot et al., 2023; Menendez and Tzortziou, 2024). Increased urban

runoff and wastewater discharges often elevate CDOM and DOC concentrations in estuaries, exacerbating optical complexity and pollution-related impacts (Menendez and Tzortziou, 2024). Accurate remote sensing of CDOM can inform management strategies for nutrient and pollutant control, habitat restoration, and mitigation of eutrophication and hypoxia (Jutla et al., 2013; Branco and Kremer, 2005).

Beyond pollution and carbon cycling, CDOM monitoring has public health implications. Variations in CDOM and associated OACs have been linked to the proliferation of waterborne pathogens such as Vibrio cholerae, enabling predictive modelling of cholera outbreaks in vulnerable coastal populations (Jutla et al., 2013). Thus, remote sensing of CDOM contributes not only to environmental but also to socio-economic resilience.

This chapter applies the semi-analytical algorithm developed in Chapter 3 to two case study regions characterised by distinct optical regimes and varying CDOM dominance. Using cloud-free OLCI satellite data from 2022-2023, the seasonal and spatial distribution of CDOM is mapped and analysed. Section 4.2 details the satellite data acquisition and processing protocols. The results for each region are presented in section 4.3, followed by a discussion of ecological and biogeochemical implications in section 4.4. Finally, section 4.5 summarises the key findings and future research directions. This study demonstrates the efficacy of the algorithm in capturing CDOM variability in turbid coastal environments and underscores the importance of improved CDOM monitoring for pollution assessment, ecosystem management, and carbon budget estimations in estuarine and coastal waters.

4.2 Data and Methodology

4.2.1 Site Description

The versatility of the developed algorithm in retrieving spatio-temporal CDOM distribution was evaluated across turbid waters in two estuarine regions with differing optical characteristics. The following sections provide detailed descriptions of the geomorphological attributes, hydrodynamic conditions, and environmental factors that influence CDOM distribution at the case study sites.

Mandovi and Zuari Estuaries

The Mandovi and Zuari Estuarine (MZE) network represents the confluence of two monsoonal rivers, the Mandovi and Zuari, with the Arabian Sea, interconnected by the Cumbarjua channel. The geometric characteristics of the MZE are described in detail in chapter 2, section 2.1. To facilitate a better understanding of the seasonal spatial distribution of surface a_{cdom}^{440} retrieved through remote sensing, both estuaries were subdivided into sections.

The Mandovi estuary was divided into two sections: the upper estuary, which is a 0.75 km wide channel along Panjim city, and the lower estuary, which includes Aguada Bay to the west of Miramar Beach (Figure 4.1). The Zuari estuary was subdivided into three sections, i.e., the upper estuary, a 1 km wide channel where the Cumbarjua canal meets the Zuari River; the middle estuary, which spans from Agacaim/Sancole to Chicalim, where Mormugao Bay begins to widen; and the lower estuary, from Chicalim to the mouth of estuary. A shallow plateau with depths of 2-3 meters was observed in the bathymetry of region, resulting in strong resuspension dynamics during periods of high flow conditions.

The bio-optical characteristics of the MZE network exhibited significant seasonal variability, primarily driven by hydrodynamic processes and monsoon winds. The relative dominance of absorption or scattering by chlorophyll-a (Chl-a) and total suspended matter (TSM) shifted according to the estuarine stratification and tidal influences (Adhikari et al., 2023). Additional details on the monsoonal nature of the estuarine network and the OACs influencing the absorption budget can be found in Sections 2.1 and c., respectively.

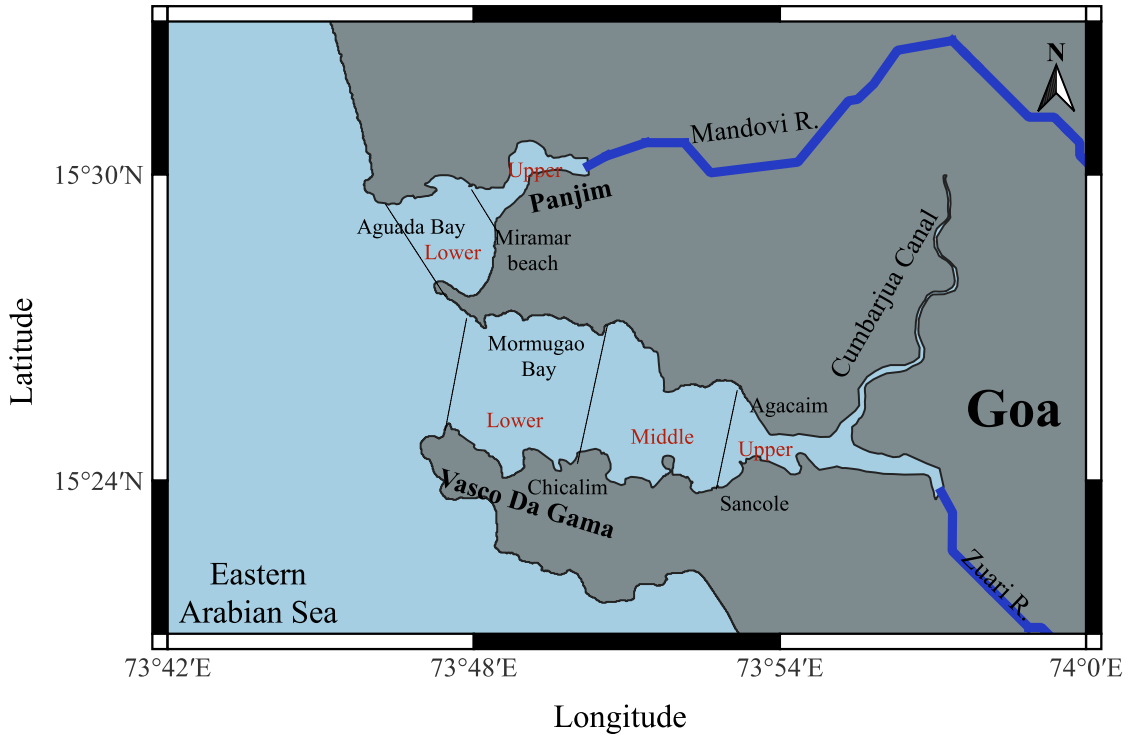

Figure 4.1: The map of Mandovi and Zuari estuarine waters with the dotted lines sectioning the estuaries.

Chesapeake and Delaware Bays

The Chesapeake and Delaware Bays (CDB) are two highly turbid and productive estuaries located along the eastern coast of the United States of America. The Chesapeake Bay is considered a single estuary, stretching about 320 km in length and varying in width between 6 and 48 km (Figure 4.2). The head of estuary marks the confluence of Susquehanna River and the bay at Harve De Grace, Maryland. The Susquehanna River contributes approximately 60% of the freshwater flow to the estuary, bringing in agricultural runoff rich in nitrogen, snowmelt, and precipitation that increase discharge volume during the spring (March to May) and summer (June to August) months.

In addition to the Susquehanna River, other major rivers, including the Potomac, Rappahannock, and James rivers, drain into the Chesapeake Bay, each exhibiting a similar seasonal discharge pattern. Approximately 700 km^2 of the eastern and western shores of the Bay are covered by tidal marshes (Tzortziou et al., 2008), with the most extensive tidal wetlands, the Blackwater Refuge National Park, located on the eastern shore near Dorchester County, Maryland. The Blackwater River, flowing through the wildlife refuge and estuaries of the Nanticoke and Wicomico rivers, shows a dominance of CDOM as it leaches through the peat soils of the marshlands (Rochelle-Newall and Fisher, 2002; Cao et al., 2018). Chesapeake Bay opens to the Mid-Atlantic Bight at Northampton, Delaware, and Cape Henry, Virginia.

The Delaware Estuary spans 80 km, with a width varying from 8 km at the head of the estuary (near Woodland Beach) to a maximum of 45 km and a narrow mouth of 18 km (Figure 4.2). It opens to the Mid-Atlantic Bight at Cape Henlopen and Cape May. The Delaware River has an annual mean freshwater discharge of 330 $m^3\ s^{-1}$, accounting for about 50% of the freshwater input to the estuary (Wane et al., 1996). The Delaware Bay is a coastal plain estuary with a shallow mean depth of 8 m and tidal marshes along both banks (Sharp et al., 2009; Cao et al., 2018). The estuary is known for its high nutrient loading from both urbanised sources (Sharp et al., 2009). The optical interactions in these estuaries are dominated by the attenuation caused by TSM and CDOM, with CDOM playing a more significant role than TSM at 440 nm (Wane et al., 1996).

4.2.2 Satellite Data Processing

Satellite data processing for retrieving CDOM from R_{rs} involves several critical steps to ensure accuracy and reliability, especially in optically complex turbid estuarine and coastal waters.

a. Data Acquisition: Imagery from OLCI aboard Sentinel-3 satellites was selected for its superior spatial resolution (300 m) and spectral bands optimised for coastal and inland

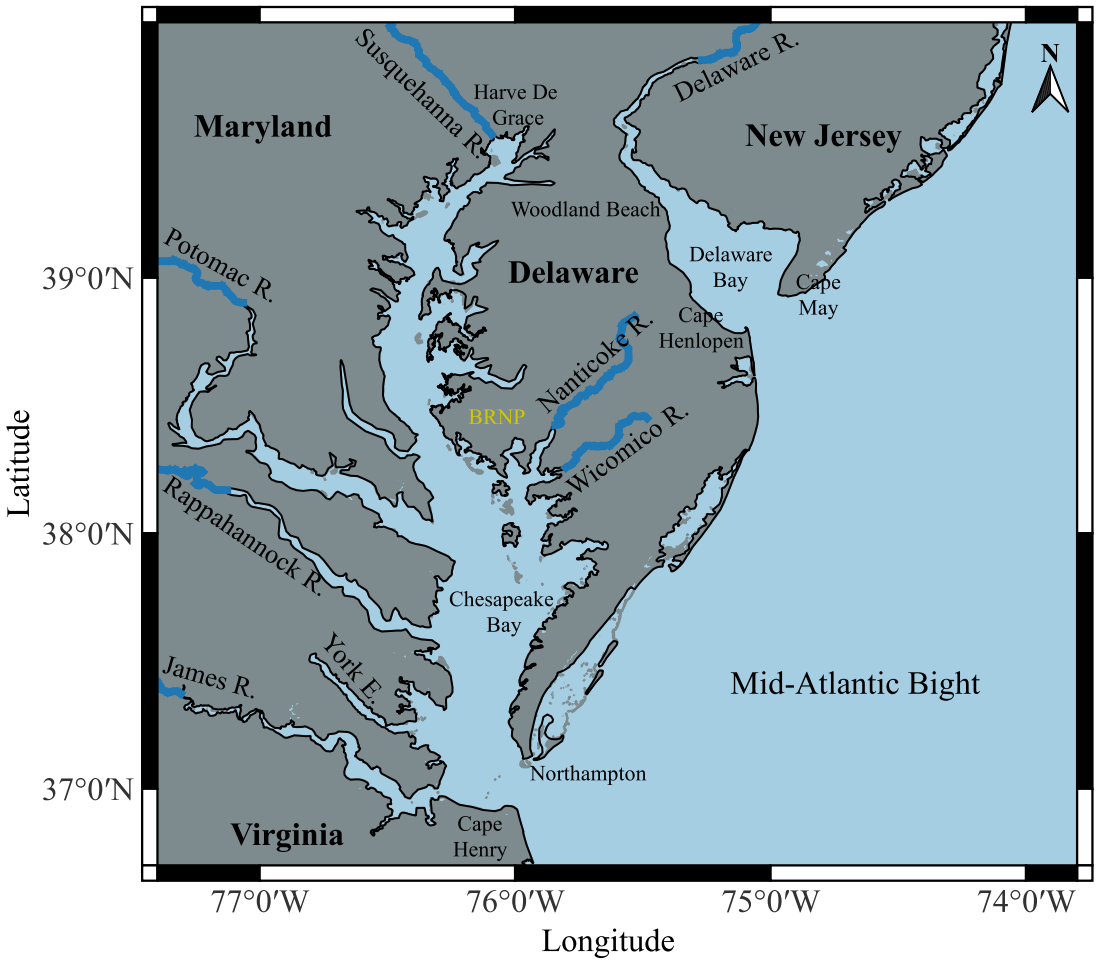

Figure 4.2: The map of Chesapeake and Delaware Bays.

waters (Werdell et al., 2018; IOCCG, 2020). Cloud-free Level 2 scenes for 2022 and 2023 covering the study regions were downloaded from the EUMETSAT data portal.

b. Atmospheric Correction: The Case 2 Regional CoastColour (C2RCC) atmospheric correction is applied Level 1 OLCI data with values typical to each region to remove contributions from aerosols, water vapour, and Rayleigh scattering that distort water-leaving radiance (Lee et al., 2002; Gao et al., 2020). This step is especially important in turbid waters with elevated suspended sediments and CDOM concentrations, which significantly alter optical properties.

c. Georeferencing and Reprojection: All scenes were reprojected to a common spatial reference system (e.g., WGS84, UTM) to maintain spatial consistency across temporal datasets. This ensures accurate spatial alignment of estuarine boundaries, riverine inputs, and coastal waters across acquisitions, enabling reliable pixel-level temporal analyses.

d. Quality Control and Pixel Masking: The pixels flagged as cloud-covered, affected by sun glint, adjacent to land, or with poor atmospheric correction quality were masked out (Gao et al., 2020). Shallow or bottom-influenced pixels were excluded using high-resolution bathymetry and coastline buffers.

e. Application of CDOM Retrieval Algorithm: The semi-analytical algorithm developed in Chapter 3 (Equation 3.17) was applied to valid pixels. Spectral bands minimising interference from Chl-a and TSM were used to estimate the CDOM absorption coefficient at 440 nm (a_{cdom}^{440}) even in complex optical waters (Adhikari et al., 2023).

f. Temporal Compositing: Monthly mean composites of a_{cdom}^{440} were generated to reduce noise from transient atmospheric variability, tidal influences, and sensor limitations. Temporal averaging preserves seasonal trends driven by monsoonal discharge, tidal cycles, and anthropogenic inputs while smoothing short-term fluctuations (Mouw et al., 2015).

g. Visualisation and Data Representation: Due to skewed CDOM concentration distributions in coastal waters, a logarithmic colour scale was employed to enhance contrast and reveal spatial and seasonal variability, highlighting hotspots linked to pollution, terrestrial runoff, or algal blooms (Ruescas et al., 2018).

h. Validation and Performance Assessment: Satellite-derived CDOM estimates were validated against concurrent in-situ a_{cdom}^{440} measurements. Statistical metrics, including coefficient of determination (r^2), root mean square error ($rmse$), mean absolute error (mae), and mean absolute percentage error ($mape$), quantified algorithm performance and uncertainties in the previous chapter 3.

4.3 Results

4.3.1 Seasonal Spatial Distribution of Retrieved CDOM Values in the MZE

The monthly-averaged spatial distribution of retrieved a_{cdom}^{440} values across the MZE and adjacent coastal waters of Goa revealed distinct and pronounced seasonal variability (Figures

4.3 - 4.5). This variability was strongly influenced by the monsoonal precipitation cycle, with the Indian Summer Monsoon (June to September) serving as the primary driver of enhanced CDOM concentrations and its spatial extent.

Persistent cloud cover during June, July, and August limited remote sensing observations. Cloud-free imagery representative of the later phase of the monsoon was only available for the month of September. To facilitate seasonal interpretation, the results were grouped into four periods: late monsoon (September), early post-monsoon (October & November), late post-monsoon (December & January) and pre-monsoon (February-May) conditions. The only cloud-free OLCI scenes were available only before the onset of heavy monsoonal rainfall (before June 10 in both 2022 and 2023). The monthly composite image thereby showed a similar distribution as the pre-monsoon months (Figure 4.4).

During the late monsoon month of September (Figure 4.3a), elevated a_{cdom}^{440} values were detected in the upper and middle reaches of the Zuari estuary, ranging from 0.45 to 0.6 m^{-1}. Conversely, the lower sections of the Mandovi and Zuari estuaries showed moderate CDOM concentrations between 0.08 and 0.17 m^{-1}. The influence of freshwater CDOM extended roughly 11 km offshore from the estuarine mouths, beyond which values decreased markedly to 0.04-0.08 m^{-1}, and became negligible at distances exceeding 47 km. It is important to note that the upper Mandovi estuary was unresolved in satellite data due to its narrow channel morphology.

This spatial pattern persisted into the early post-monsoon period. In October (Figure 4.3b), the upper and middle Zuari estuary maintained high a_{cdom}^{440} values (0.45-0.6 m^{-1}), while the lower estuarine sections remained between 0.08 and 0.17 m^{-1}. By November (Figure 4.3c), CDOM concentrations in the upper Zuari estuary peaked above 0.87 m^{-1}, with a distinct plume extending from the estuarine mouth into adjacent coastal waters. This plume began to dissipate as it spread offshore, where CDOM levels reduced to 0.04-0.08 m^{-1} up to 70 km from the coastline. Such distribution patterns reflect continued riverine discharge and mixing processes typical of the post-monsoon season.

During the later post-monsoon months (December and January; Figures 4.3d-e), CDOM showed increased lateral diffusion and decreased spatial gradients, resulting in a less sharply defined interface between high and low concentration zones. In December, a_{cdom}^{440} in the middle Zuari estuary ranged from 0.26 to 0.6 m^{-1}, with the highest values (>0.87 m^{-1}) concentrated near the estuary head. By January, the estuary exhibited partially mixed conditions, reflected by a more homogeneous CDOM distribution. The CDOM concentrations at the estuary mouth ranged from 0.08 to 0.26 m^{-1}, while a zonal gradient was observed in coastal waters with nearshore values of 0.08-0.17 m^{-1} extending 17-20 km offshore, followed by values of 0.04-0.08 m^{-1} reaching up to 40 km. Beyond this, CDOM levels were minimal.

The pre-monsoon months exhibited a marked intensification of CDOM concentrations throughout the estuary and coastal zone. In February (Figure 4.4a), the upper and middle Zuari estuary exhibited elevated a_{cdom}^{440} values exceeding 0.6 m^{-1} and between 0.26-0.43 m^{-1}, respectively, while lower estuarine sections registered 0.17-0.26 m^{-1}. This upward trend continued into March (Figure 4.4b), with upper estuarine values surpassing 0.87 m^{-1} and lower estuary values rising to 0.17-0.45 m^{-1}. These represent the highest CDOM levels observed across all seasons, likely reflecting reduced freshwater flushing and increased residence time, promoting autochthonous production or accumulation.

In coastal waters, the zonal distribution pattern evident during the late post-monsoon period contracted in the period preceeding the monsoon (Figures 4.5f-j). Nearshore CDOM concentrations of 0.08-0.17 m^{-1} were confined within 9-11 km from the coast, with values of 0.04-0.08 m^{-1} extending only to 19-24 km offshore. This contraction likely reflects increased coastal salinity reducing the influence of freshwater-derived CDOM inputs, combined with enhanced mixing and photodegradation under clearer water conditions (Vecchio and Subramaniam, 2004; Cao et al., 2018).

Overall, the seasonal patterns of a_{cdom}^{440} distribution in the MZE highlight the strong influence of monsoonal river discharge, estuarine circulation, and mixing processes on the transport and fate of CDOM in tropical estuarine-coastal systems. These findings underscore the utility of the developed algorithm in resolving complex bio-optical patterns associated with CDOM variability in turbid waters.

4.3.2 Seasonal Spatial Distribution of Retrieved CDOM Values in the CDB

The spatial and temporal patterns of a_{cdom}^{440} in the CDB reflect the strong influence of terrestrial inputs, primarily driven by riverine discharge and land-based sources, consistent with previous studies of estuarine CDOM dynamics (Vecchio and Subramaniam, 2004; Mannino et al., 2014). Across all months, a clear gradient in CDOM concentration was observed, with the highest values near the headwaters of major tributaries, such as the Susquehanna River, progressively decreasing toward the estuarine mouths and coastal waters (Figures 4.6 - 4.8).

Seasonal fluctuations in CDOM concentration were most pronounced near the head of the Chesapeake Bay estuary. Peak a_{cdom}^{440} values occurred during the spring, particularly in April (up to 1.6 m^{-1}; Figure 4.6b), coinciding with increased river discharge from snowmelt and precipitation events (Hong and Shen, 2013). In contrast, the summer months of July and August exhibited significantly reduced CDOM concentrations, with minimum values around 0.4 m^{-1} (Figures 4.7a-b), likely due to decreased freshwater input, increased photodegradation,

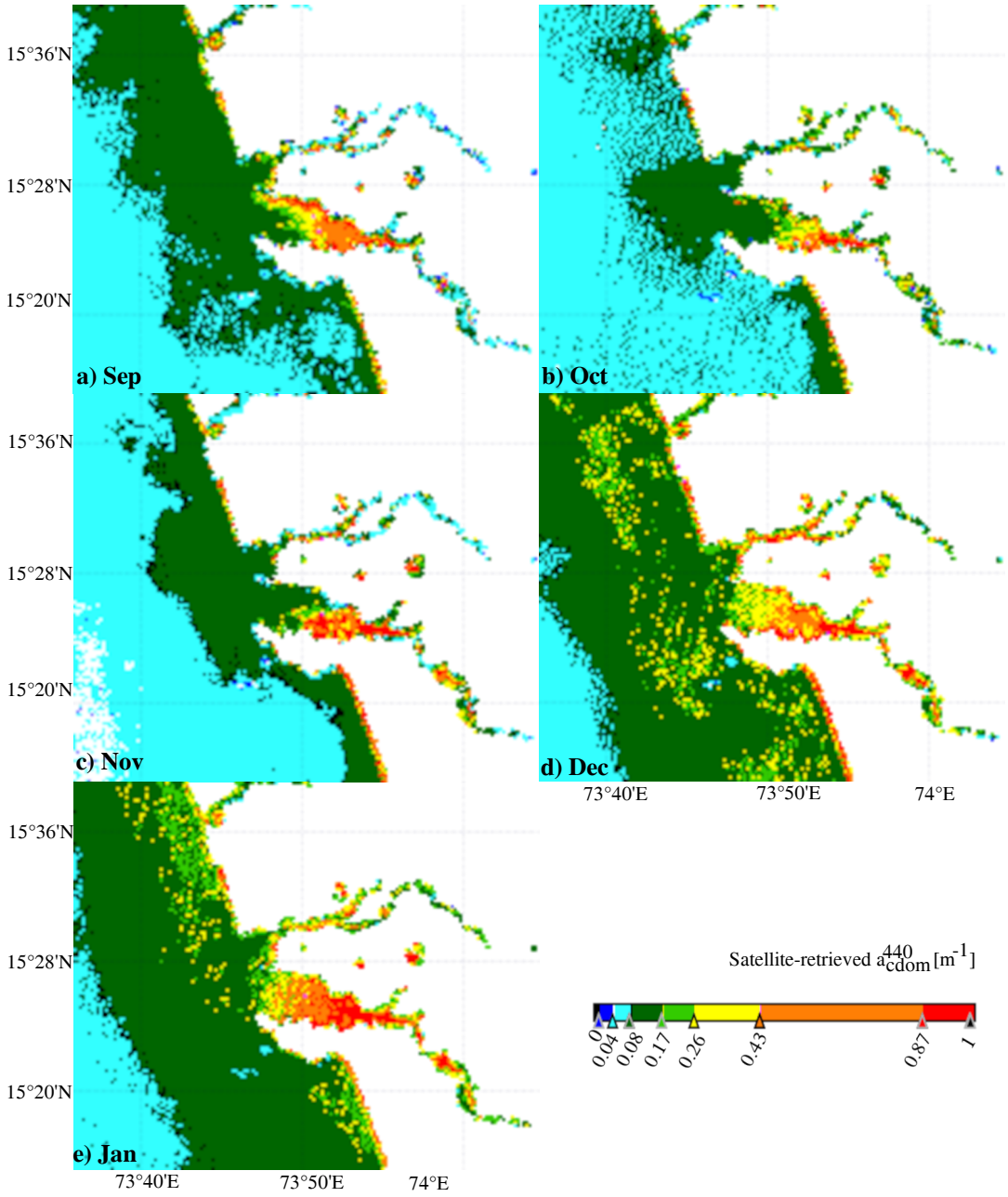

Figure 4.3: Composite monthly maps of retrieved a_{cdom}^{440} for the Mandovi and Zuari estuaries, derived from cloud-free OLCI scans during 2022-2023. Months shown are: a) September, b) October, c) November, d) December, e) January.

and enhanced biological consumption during warmer periods.

The spatial extent of elevated CDOM concentrations (>0.75 m^{-1}) also varied seasonally.

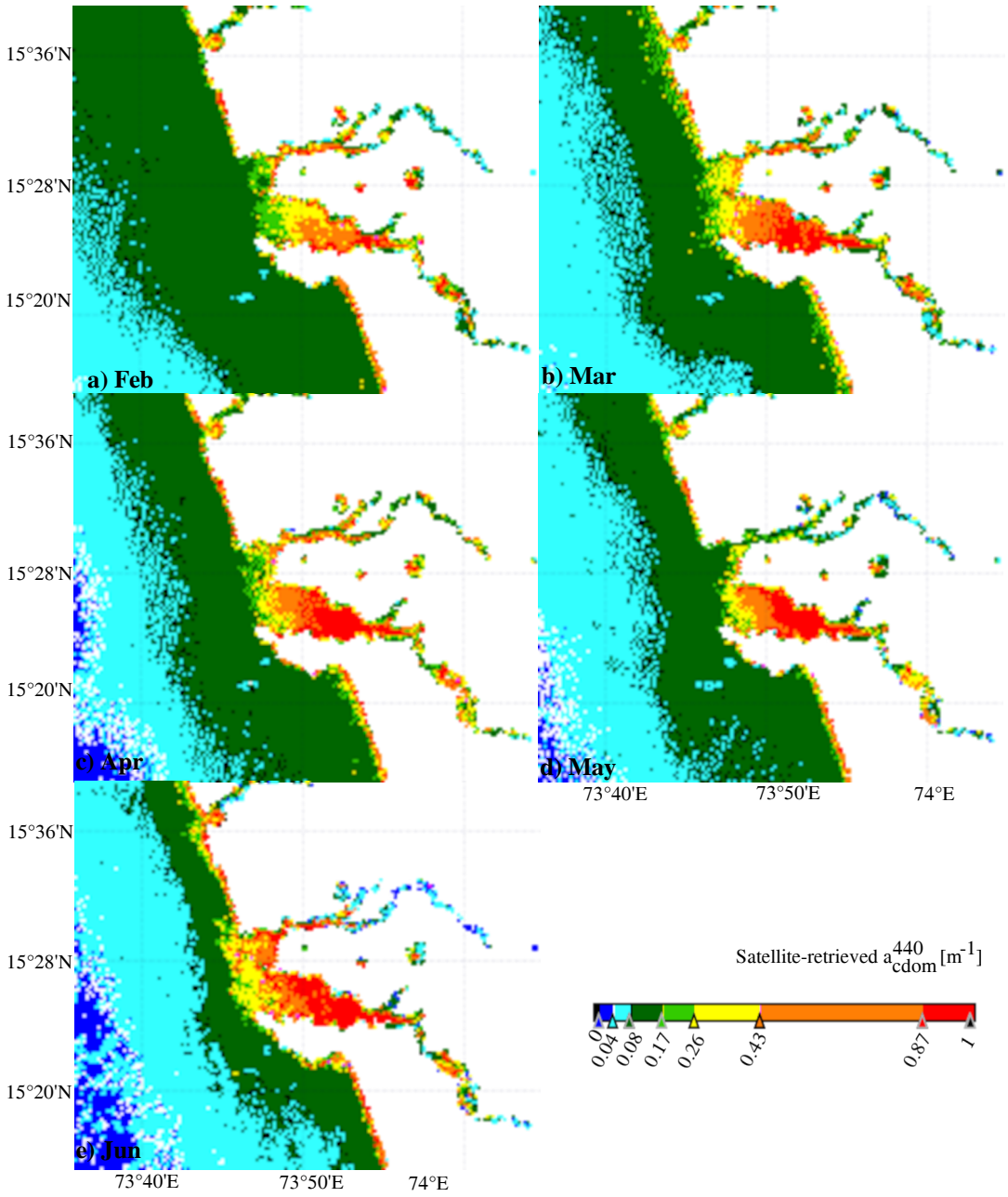

Figure 4.4: Composite monthly maps of retrieved a_{cdom}^{440} for the Mandovi and Zuari estuaries, derived from cloud-free OLCI scans during 2022-2023. Months shown are: a) February, b) March, c) April, d) May, and e) June. No cloud-free images were available for July and August.

During winter and early spring (December to April), high CDOM levels extended up to 45

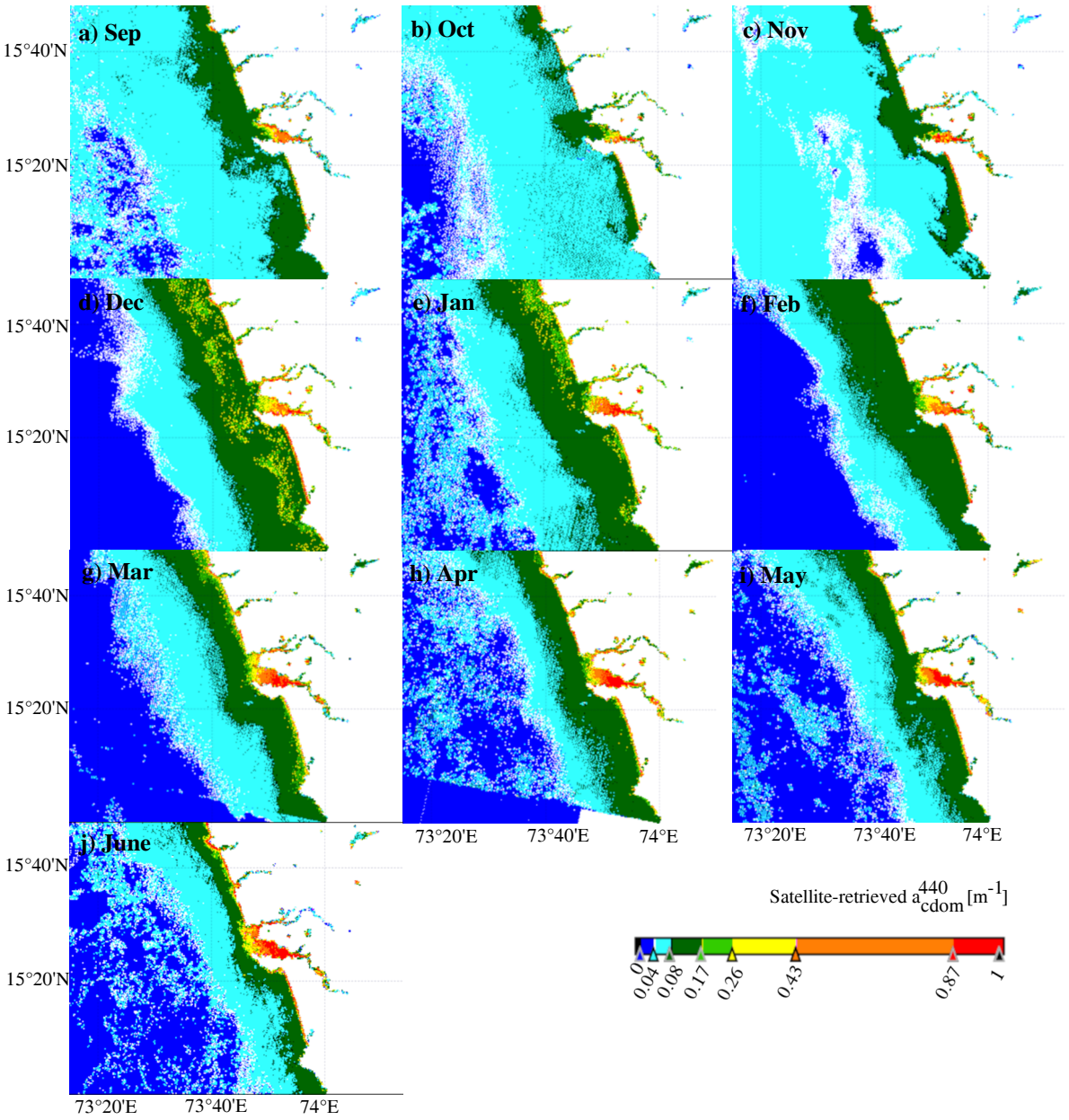

Figure 4.5: Composite monthly maps of retrieved a_{cdom}^{440} for coastal waters of Goa, derived from cloud-free OLCI scans during 2022-2023. Months shown are: a) September, b) October, c) November, d) December, e) January, f) February, g) March, h) April, i) May, and j) June. No cloud-free images were available for July and August.

km offshore from the estuary head in December (Figure 4.8b) and reached approximately 65

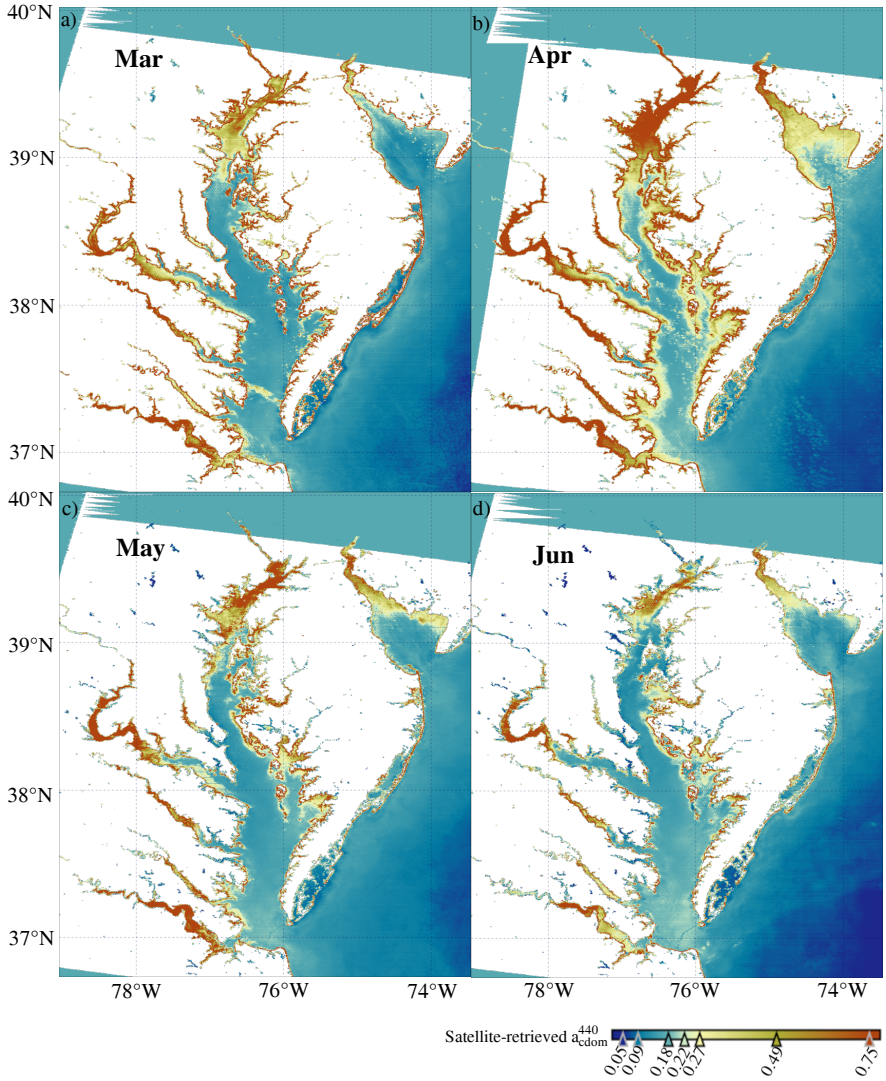

Figure 4.6: Composite monthly maps of retrieved a_{cdom}^{440} values for Chesapeake and Delaware Bays and adjacent coastal waters of the Mid-Atlantic Bight, derived from cloud-free OLCI scans during 2022-2023. Months shown are: a) March, b) April, c) May, and d) June.

km by April (Figure 4.6b). By summer, this extent contracted markedly, with elevated CDOM confined within 12-15 km offshore, reflecting reduced riverine discharge and increased dilution from coastal circulation (Figure 4.7b).

This seasonal pattern was similarly evident in other major tributaries, such as the Potomac and James Rivers, where the spatial distribution and magnitude of CDOM mirrored that observed in the Susquehanna River. For example, in August, elevated a_{cdom}^{440} values were restricted to 50 km upstream in the Potomac River and 40 km in the James River, compared to broader

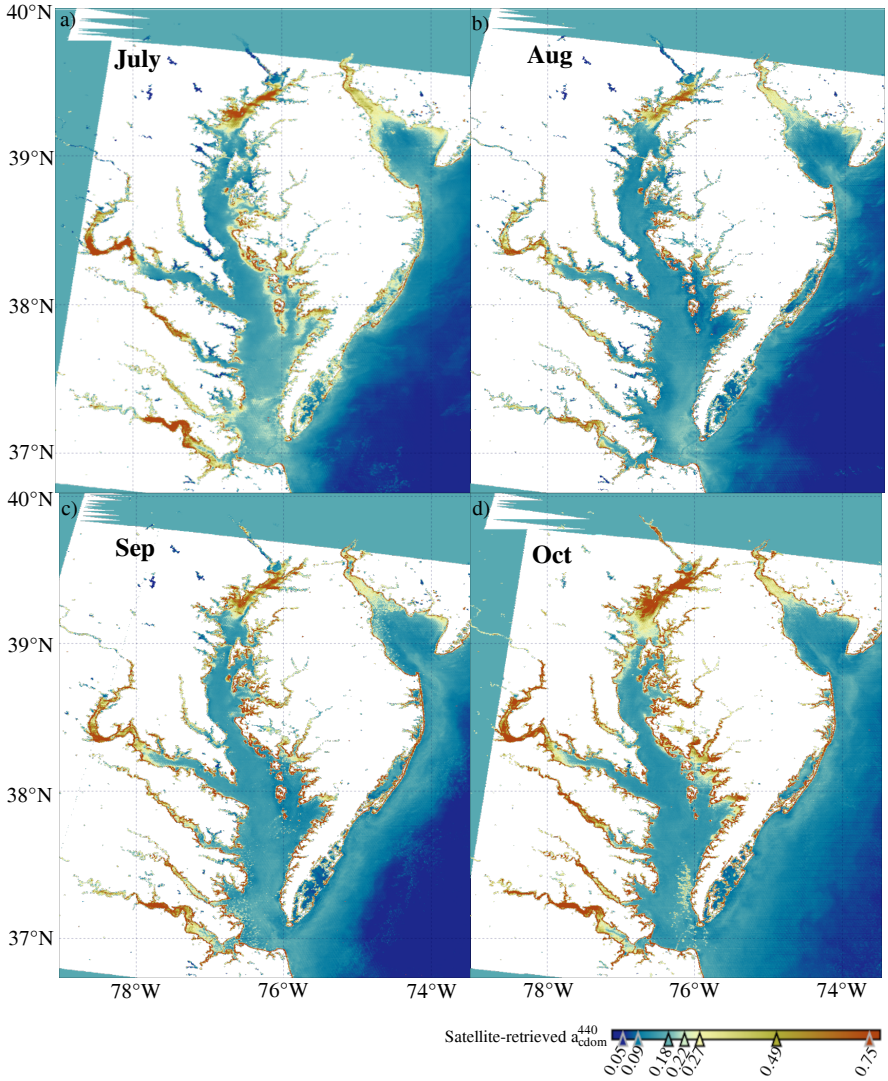

Figure 4.7: Composite monthly maps of retrieved a_{cdom}^{440} values for Chesapeake and Delaware Bays and adjacent coastal waters of the Mid-Atlantic Bight, derived from cloud-free OLCI scans during 2022-2023. Months shown are: a) July, b) August, c) September, d) October.

extents during the spring months. At the river mouths, springtime CDOM concentrations averaged around 0.49 m^{-1}, declining to approximately 0.12 m^{-1} throughout the remainder of the year.

Throughout the main stem of Chesapeake Bay, CDOM concentrations remained relatively low and stable, ranging between 0.09 and 0.11 m^{-1}, with the lowest values observed in late fall (November) and the highest in spring (April). This consistency likely reflects the mixing of freshwater inputs with higher salinity coastal waters and dilution processes (Spencer et al., 2007).

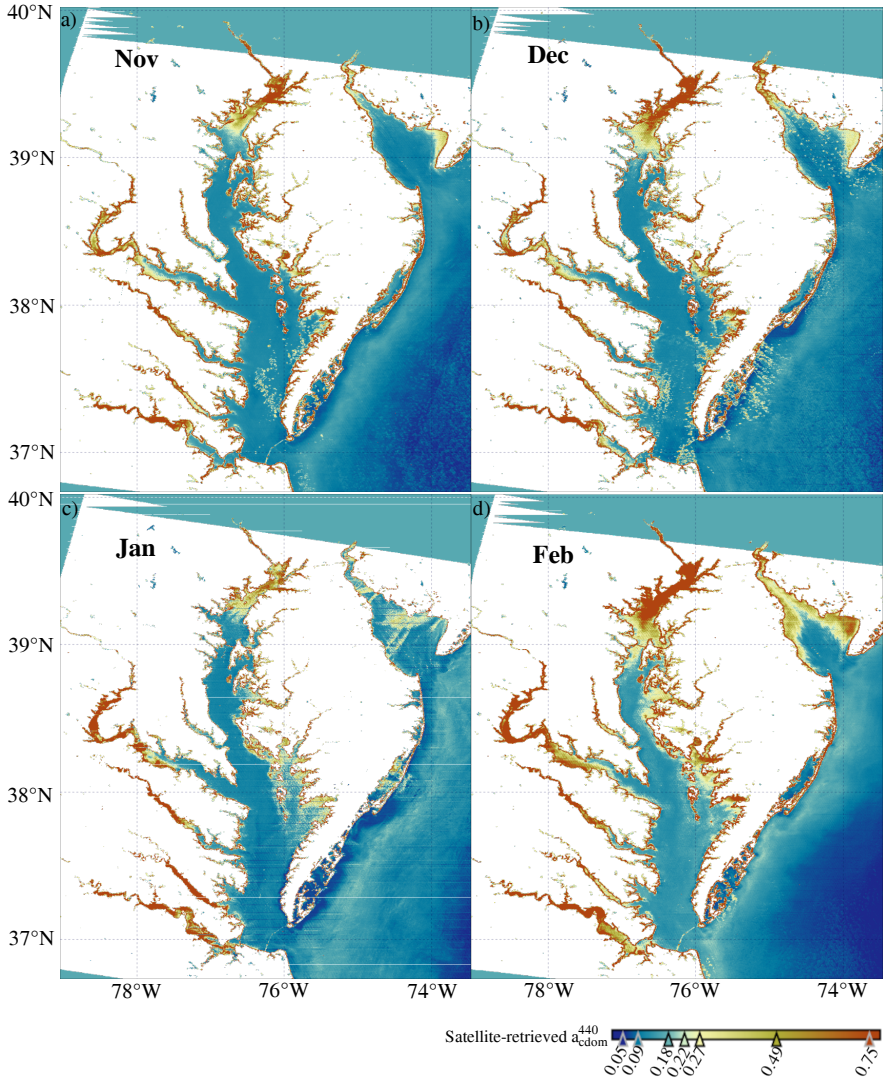

Figure 4.8: Composite monthly maps of retrieved a_{cdom}^{440} values for Chesapeake and Delaware Bays and adjacent coastal waters of the Mid-Atlantic Bight, derived from cloud-free OLCI scans during 2022-2023. Months shown are: a) November, b) December, c) January, and d) February.

Elevated CDOM concentrations (0.4-0.8 m^{-1}) were also detected along the eastern shore of Chesapeake Bay, particularly surrounding ecologically important wetlands such as the Blackwater National Wildlife Refuge and estuarine regions of Nanticoke and Wicomico rivers (Figures 4.6b-c). These wetlands are significant sources of CDOM and DOC to adjacent waters (Briggs et al., 2018). Seasonal declines in these concentrations during summer and early fall (0.2-0.3 m^{-1}; Figures 4.7b-d,4.8a) correspond with reduced freshwater inflows and heightened photobleaching under increased solar irradiance.

In the Delaware estuary, seasonal dynamics of CDOM closely paralleled those in Chesapeake Bay. Maximum a_{cdom}^{440} values were observed during spring (April), ranging from 1.7 m^{-1} at the estuary head to 0.9 m^{-1} at the mouth, consistent with riverine discharge peaks (Coble, 2007). During summer (August), concentrations decreased significantly to 0.36 m^{-1} at the estuary head and 0.2 m^{-1} at the mouth (Figure 4.7b), reflecting the combined influence of diminished freshwater input, photodegradation, and biological uptake.

Coastal waters adjacent to both estuaries demonstrated generally lower CDOM concentrations, although localised plumes were occasionally evident, particularly near river mouths where terrestrial inputs and tidal mixing introduce CDOM into the coastal ocean. Seasonal modulation of CDOM in these nearshore zones was apparent, with elevated concentrations during spring and early summer and marked reductions in late summer and fall. Offshore regions of the Mid-Atlantic Bight exhibited lower and more diffuse CDOM values, likely due to mixing with open ocean waters and photo-bleaching effects under increased solar exposure (Stedmon et al., 2000; Spencer et al., 2007).

Overall, the observed seasonal and spatial variability in a_{cdom}^{440} underscores the dominant role of terrestrial inputs, estuarine circulation, biological processes, and photochemical degradation in controlling CDOM dynamics in temperate estuarine-coastal environments.

4.4 Discussion

The satellite-derived CDOM distributions for both the MZE and CDB reveal critical insights into the biogeochemical and physical processes governing these turbid estuarine systems, despite their distinct bio-optical characteristics.

4.4.1 Processes controlling CDOM distribution in MZE

The optical properties of the MZE fluctuate dynamically between absorption-dominated conditions, primarily influenced by Chl-a, and scattering-dominated regimes governed by TSM (Adhikari et al., 2023). This variability is strongly modulated by estuarine hydrodynamics, including tidal mixing, freshwater discharge, and sediment resuspension. The algorithm developed herein successfully retrieved CDOM concentrations amidst this complex optical environment, reflecting the robustness of the approach in highly variable turbid waters.

During the late monsoon period (particularly September), the lowest CDOM absorption (a_{cdom}^{440}) values were retrieved in the upper and middle Zuari estuary (0.45-0.6 m^{-1}), consistent with historic in-situ depth-averaged measurements (Menon et al., 2011). Slope analyses of CDOM absorption spectra indicate that terrestrial runoff is the dominant source during this period, with intense freshwater discharge diluting seawater and flushing the estuarine system

rapidly (Vijith et al., 2009). Such flushing reduces the residence time of water masses, suppressing microbial activity and in-situ CDOM production. Concurrently, persistent cloud cover during the monsoon reduces solar irradiance, further inhibiting both primary production and photodegradation of CDOM (Guallar and Flos, 2019). Hence, CDOM levels during the monsoon are controlled largely by terrestrial inputs, with minimal in-situ transformation.

The early post-monsoon phase sees CDOM concentrations becoming more spatially confined within the estuary, particularly in the middle Zuari region characterised by fluctuating salinity due to tidal reversal (Vijith et al., 2009). This enhanced mixing results in more homogeneous CDOM distributions (0.08-0.17 m^{-1}), with concomitant increases in Chl-a and TSM suggesting nutrient accumulation that may stimulate microbial degradation and vertical mixing of organic matter (Adhikari et al., 2023). Shallow bathymetry promotes bottom turbulence and sediment resuspension, affecting CDOM patterns. Spectral slope analyses imply increased in-situ CDOM production on the seaward side of the plume relative to riverine sources, though still less than adjacent shelf waters (Adhikari et al., 2023).

A prominent CDOM plume observed at the estuary mouth represents the outflow of trapped estuarine circulation combined with in-situ generated CDOM, extending the riverine influence into coastal waters. Offshore, very low a_{cdom}^{440} values up to 45 km from the mouth indicate significant mixing and dilution of freshwater-derived CDOM (Adhikari et al., 2023).

As discharge declines in late post-monsoon months (December-January), the estuary transitions toward a partially mixed regime, with stratification zones shifting upstream (Qasim and Sen Gupta, 1981; Adhikari et al., 2023). Mixing intensifies throughout the estuary, increasing CDOM concentrations across the domain. Spectral analyses reveal contributions from both degraded terrestrial organic matter and enhanced in-situ production. Elevated Chl-a near stratification maxima reflects increased primary production, accompanied by photodegradation of both phytoplankton biomass and terrestrially derived organics. Reduced flow velocities facilitate vertical mixing and microbial degradation, yielding higher surface CDOM levels. Spatially, plume patterns diminish while more heterogeneous CDOM distributions arise mid-estuary, whereas nearshore waters show narrowing bands of CDOM with distance offshore. Beyond these zones, CDOM concentrations are minimal, reflecting limited export.

During the pre-monsoon season, nearshore CDOM bands contract further as salinity returns to oceanic levels ($\approx$35) and estuarine channels behave as coastal extensions influenced by strong tidal forcing (Shetye et al., 1995). Elevated Chl-a concentrations and frequent algal blooms characterise this season, with increased solar radiation promoting primary production and phytoplankton breakdown (Adhikari et al., 2023; Pednekar et al., 2012). Slope parameters confirm that in-situ CDOM production dominates during this period, explaining the highest

observed a_{cdom}^{440} values driven by phytoplankton degradation within well-mixed waters, with limited export offshore. Overall, CDOM seasonal dynamics in MZE reflect the interplay between hydrodynamics, terrestrial inputs, and biological processes, well captured by the satellite retrievals despite CDOM's lesser role in optical attenuation relative to Chl-a and TSM in this turbid system.

4.4.2 Processes controlling CDOM distribution in CDB

In contrast, the CDB waters are characterised by optical regimes dominated by CDOM, which is the principal light-absorbing constituent (Adhikari et al., 2023, section 3.4.1). CDOM in these estuaries is overwhelmingly allochthonous, sourced mainly from extensive agricultural runoff via the Susquehanna, Delaware, Potomac, and other major rivers (Rochelle-Newall and Fisher, 2002).

A persistent spatial gradient is evident, with a_{cdom}^{440} decreasing from river headwaters toward the bay mouths and offshore waters. This pattern aligns with typical estuarine systems where terrestrial CDOM input dominates (Guo et al., 2007; Das et al., 2017). Tributaries consistently exhibit elevated CDOM concentrations, underscoring the strong influence of land-derived organic matter.

Seasonally, peak CDOM levels correspond to spring snowmelt and increased rainfall, driving elevated river discharge and extensive CDOM advection into estuarine waters (Rochelle-Newall and Fisher, 2002; Cao et al., 2018). During the relatively long residence time of water in Chesapeake Bay (90-180 days; Kemp et al. 2005), photochemical and microbial degradation progressively reduce CDOM concentration, aromaticity, and molecular weight downstream (Cao et al., 2018). Despite marked seasonal variations in phytoplankton biomass, CDOM distribution remains fairly uniform along the estuarine mainstem, reinforcing terrestrial inputs as the dominant source, with downstream transport modulated by hydrodynamic mixing.

Elevated a_{cdom}^{440} near wetland systems, such as Blackwater National Wildlife Refuge, point to peat soil leaching and wetland-derived CDOM contributions. This CDOM fraction is highly photoreactive with a lower spectral slope, making it susceptible to rapid photodegradation (Tzortziou et al., 2008). The biogeochemical cycling of wetland CDOM is dynamic, fluctuating considerably over short timescales due to tidal fluxes, solar irradiance, and precipitation events (Tzortziou et al., 2008, 2011). Although monthly satellite composites capture seasonal trends, higher temporal resolution imagery would be required to resolve diel or tidal variability adequately.

The nearshore-to-offshore decline in CDOM, along with its seasonal reduction in summer, supports the concept of photo-bleaching reducing CDOM concentrations as it is exported

offshore. The absence of a clear latitudinal gradient in this study contrasts with previous observations of a north-south decline (Mannino et al., 2014), which may be attributed to interannual variability or the spatial resolution limits of satellite data.

Collectively, the observed seasonal and spatial CDOM patterns in the CDB have significant implications for coastal carbon cycling, ecosystem productivity, and water quality management. They highlight the importance of terrestrial runoff as a dominant source of CDOM, its transformation during estuarine transit, and the influence of wetland inputs and photochemical processes. These insights inform monitoring strategies and management policies aimed at sustaining the ecological health of these productive estuarine-coastal environments.

4.5 Conclusion

This chapter demonstrates the application of the developed algorithm to retrieve the distribution of CDOM and to assess its seasonal variability in estuarine and coastal waters. The algorithm effectively delineates the spatial distribution of CDOM based on R_{rs} in turbid waters, despite significantly varying OACs dominating the optical interactions.

The algorithm provided an annual distribution of CDOM for the MZE, where Chl-a and TSM consistently dominated the R_{rs} throughout the year. In MZE, the retrieved CDOM maps accurately represented the monthly-averaged extent of the riverine plume, illustrating its seasonal dissipation and the evolving mixing zone between freshwater and seawater as riverine forcing decreased. As the estuary transitioned to a partially mixed system during the post-monsoon months, the algorithm successfully captured the shift in the source of CDOM from land-advected to in-situ generated material.

The algorithm also performed well in mapping CDOM distribution in the CDB, where CDOM plays a significant role in the absorption budget. The spatial extent of high CDOM concentrations at the head of Chesapeake Bay, particularly during the spring months when increased river discharge occurred, was effectively captured. Moreover, the algorithm highlighted carbon export from wetlands along the shores of CDB, offering valuable insights into the contribution of wetland-derived organic carbon to the region's biogeochemistry.

Further application of the developed algorithm on weekly or daily average satellite data would enable more granular tracking of organic matter distribution in estuarine and coastal waters. Such high-frequency monitoring could enhance our understanding of carbon cycling within these ecosystems, providing insights into the dynamics of carbon export, particularly following extreme precipitation events. Additionally, tracking not only CDOM but also particulate OACs and the diffuse attenuation coefficient would contribute to a better estimation of radiant heating rates, which is crucial for understanding the thermal dynamics of coastal waters

and their impact on the ecosystem.

Chapter 5

Bio-optical Complexity of Coastal Waters and their Effect on Radiant Heating Rates

5.1 Introduction

The dynamic variability of optically active constituents (OACs) is a defining characteristic of estuarine and coastal environments, contributing to their complex optical and biogeochemical properties (Menon et al., 2005). Among these OACs, chromophoric dissolved organic matter (CDOM), chlorophyll-a (Chl-a), and total suspended matter (TSM) exhibit spatially and temporally heterogeneous distributions that are shaped by a multitude of physical, chemical, and biological processes. The inherent optical properties (IOPs) such as absorption and scattering coefficients of OACs that interact with sunlight in distinct ways across the visible spectrum. The collective optical response of these constituents defines a specific bio-optical state of the water body, which is far from static but rather dynamically evolving (Smith and Baker, 1981). This bio-optical state results from the intricate interplay of hydrological forcing, biological productivity, and biogeochemical transformations that modulate the concentrations and spectral characteristics of OACs, leading to what is often termed bio-optical complexity.

Bio-optical complexity encompasses the nonlinear interactions between light and the OACs, creating challenges for both observational and modelling approaches (Morel and Antoine, 1994). It significantly governs the availability and transmission of light in the water column, which is a fundamental driver of ecological and physical processes in coastal zones. Light attenuation influences primary production by controlling photosynthetically available radiation (PAR), regulates thermal stratification patterns through differential absorption of solar energy, and affects nutrient cycling by shaping the habitats and activities of microbial communities (Jerlov, 1976; Lewis et al., 1990; Kirk, 1994; Marra et al., 1995; McClain et al., 1996). These processes are tightly coupled, and thus an accurate characterisation of light attenuation

under diverse bio-optical conditions is essential for understanding ecosystem dynamics and heat budgets in coastal waters.

Extensive research has addressed radiant heating rates (RHR) in open ocean environments, advancing our understanding of light penetration and thermal dynamics at regional to global scales (Ohlmann, 2003; Manizza et al., 2005; Lengaigne et al., 2007; Gnanadesikan and Anderson, 2009; Turner et al., 2012; Giddings et al., 2020). However, coastal waters, particularly estuaries and continental shelves, remain underrepresented in global climate models and biogeochemical simulations. This is largely due to the challenges associated with their optical complexity and heterogeneity, which are difficult to parameterise accurately. Many existing models simplify coastal optics by assuming homogeneity or by using empirical parameterisations derived from limited datasets, often failing to capture the spatial and temporal variability of OACs in these environments (Kim et al., 2018). Consequently, such models may inaccurately estimate RHR and associated processes, which can propagate uncertainties into larger-scale climate and ecosystem predictions (Gnanadesikan et al., 2019).

Empirical and mechanistic studies underscore that vertical transmission of solar irradiance (T_r) and consequent heat absorption are strongly influenced by the concentrations and spectral characteristics of key OACs, especially Chl-a and CDOM, alongside environmental factors such as cloud cover, solar zenith angle, and sea surface albedo (Chang and Dickey, 2004). For example, in Arctic coastal regions, increasing CDOM inputs from thawing permafrost and enhanced riverine runoff have been linked to significant reductions in underwater light transmission, with decreases in T_r by as much as 40%, thereby influencing local thermal regimes and biogeochemical cycles (Hill, 2008). In the northwestern Mediterranean, elevated CDOM levels correlate with reduced light penetration depth and stronger surface heating, highlighting how regional bio-optical conditions modulate thermal dynamics (Pérez et al., 2016). Similarly, in estuarine systems such as Tampa Bay and the Laptev Sea, terrestrial CDOM has been found to account for up to 70% of the observed variability in diffuse attenuation coefficients, resulting in measurable increases in energy absorption and heating rates (Branco and Kremer, 2005; Soppa et al., 2019). These examples illustrate the pivotal role of CDOM and overall bio-optical complexity in modulating coastal light environments and heat budgets.

As coastal regions face accelerating anthropogenic pressures and climate change impacts, including alterations in freshwater inflows, increased nutrient loading, and changing organic matter sources, it becomes imperative to better understand how spatio-temporal variability in OACs influences radiant heat distribution and air-sea energy exchange (Fichot et al., 2023;

Menendez and Tzortziou, 2024). Accurate representation of these processes is crucial for predicting ecological responses, managing coastal resources, and improving climate model projections. This chapter aims to quantify the influence of OAC variability on bio-optical complexity and its implications for radiant heating rates in estuarine and coastal waters. We apply advanced remote sensing data, in-situ observations, and radiative transfer modeling to dissect the interactions between OAC distributions, optical properties, and radiant heating.

Section 5.2 provides a comprehensive overview of the datasets, including satellite and field measurements, as well as the computational methods and statistical analyses employed. Section 5.3 presents the spatial and temporal patterns of radiant heating rates derived from these data. In section 5.4, the interpretation of results in context of regional and global coastal bio-optical variability and discuss their broader implications is included. Finally, section 5.5 summarises the key findings and outlines future research directions to enhance the representation of coastal bio-optical complexity in climate and ecosystem models.

5.2 Data and Methodology

5.2.1 Study Area

The analysis of bio-optical complexity and its influence on RHR was conducted using data collected from the coastal waters of the eastern Arabian Sea (EAS). The sampling strategy involved cross-shore transects along the west coast of India, targeting major riverine systems including the Mandovi, Zuari, Kali, Sharavati, Haladi, Netravathi, Valapattanam, Chaliyar, Bharathapuzha, and Periyar during the pre-monsoon and post-monsoon periods. This approach enabled the assessment of seasonal impacts of riverine discharge and the associated transport of OACs on surface reflectance characteristics. Details of these coastal surveys are provided in section 2.1.

The dataset comprises 152 sampling stations, with water depths ranging from 10 m to 200 m, encompassing a gradient from shallow, turbid nearshore zones to comparatively clearer offshore environments. To complement this spatial dataset, a focused case study was conducted using temporally resolved observations from a research cruise onboard ORV $SagarManjusha$ in January 2017. The vessel was anchored near the mouth of the Mandovi Zuari estuarine system (MZE) at a depth of approximately 20 m. The optical and hydrographic measurements were collected at three fixed times, i.e., 1000 h, 1300 h, and 1600 h, each day from 12^{th} and 27^{th} January 2017, providing a high-resolution temporal profile of diurnal variability in bio-optical properties.

5.2.2 Additional IOP parameters: Source of CDOM and spectral particulate backscattering coefficient

The instruments employed during the coastal surveys and the methodology used to estimate the in-situ absorption coefficients of individual OACs are detailed in Section 2.2.

The spectral absorption coefficient of chromophoric dissolved organic matter (a^{λ}_{cdom}) was used as a diagnostic tool to infer its source and transformation state. The slope of the exponential decay of the CDOM absorption spectrum provides insight into changes in molecular weight and aromaticity, often driven by photochemical degradation processes (Helms et al., 2008).

McKnight et al. (2001) introduced a fluorescence-based index to differentiate between microbially and terrestrially derived fulvic acids, using excitation at 370 nm and the emission intensity ratio at 450 nm and 550 nm. Values approaching 1.9 indicate microbially derived sources, whereas values around 1.4 indicate terrestrial origin. Drawing from a similar concept, this study employed an absorption-based index in the visible spectral range, as proposed by Senesi et al. (1989). This metric, termed the CDOM humification ratio (h_{ratio}), serves as a proxy for the degree of humification and is calculated as:

$$h_{ratio} = \frac{a^{465}_{cdom}}{a^{665}_{cdom}} \tag{5.1}$$

This ratio captures the relative absorption at shorter versus longer wavelengths, providing information on the aromatic content and source characteristics of CDOM.

In addition to CDOM absorption, vertical profiles of the total backscattering coefficient at 650 nm (b^{650}_{b}) were obtained using radiometric sensors. The particulate backscattering coefficient at the same wavelength ($b^{650}_{b_p}$) was derived by subtracting the contribution of pure seawater backscattering ($b^{650}_{b_{sw}}$), following the formulation of Twardowski et al. (2007).

To reconstruct the spectral shape of the particulate backscattering coefficient, a power-law model was applied:

$$b^{m}_{b_p}(\lambda) = b_{b_p}(\lambda_0) \times \frac{\lambda}{\lambda_0}^{-\gamma} \tag{5.2}$$

This formulation, initially proposed by Morel and Prieur (1977) and later refined by Neukermans et al. (2012), accounts for the spectral variability in particulate backscattering due to particle size distribution and composition changes. The model was implemented following Step 5 of the QAA (Quasi-Analytical Algorithm) version 6 framework, as described in Table 3.2.

5.2.3 Bio-optical complexity classifaction

The turbid coastal waters of the EAS exhibit a wide range of concentrations and optical properties of OACs, resulting in high spatio-temporal variability in IOPs. The hydrographic conditions, which vary seasonally, modulate the distribution of OACs, and the nonlinear interactions among their IOPs produce corresponding changes in the remote sensing reflectance (R_{rs}) spectra of surface waters. These spectral variations, governed by the principles outlined in equations (3.1–3.3) in Section 3.1, reflect the complex interplay of absorption and scattering by CDOM, Chl-a, and TSM, a phenomenon we refer to as bio-optical complexity.

To investigate the variability in the ratio of hyperspectral reflectance (RHR) across different bio-optical regimes, we categorised the in-situ R_{rs} observations into discrete clusters based on dominant OAC influence. The classification was developed using established spectral absorption signatures of the constituents. A notable dip in R_{rs} at 443 nm is typically indicative of strong Chl-a absorption (Cannizzaro and Carder, 2006), whereas CDOM and TSM exhibit peak absorption at shorter wavelengths (see Figure 3.1). Accordingly, the ratio of $R_{rs}(412)$ to $R_{rs}(443)$ was selected as a diagnostic metric to distinguish Chl-a-dominant waters from those influenced more by CDOM and TSM.

Waters with $R_{rs}^{412} : R_{rs}^{443} > 1.1$ were classified as optically least complex (O_1^T). Based on the inversion of equation 3.1, where $R_{rs} \propto a(\lambda)^{-1}$, this condition implies that the cumulative absorption at 443 nm (by a_{chl}, a_{cdom}, and a_{tsm}) exceeds that at 412 nm, pointing to Chl-a as the dominant absorber. These waters closely resemble Case 1 waters (Morel and Prieur, 1977), though the potential influence of autochthonous CDOM or flocculated detrital TSM cannot be entirely excluded (Carder et al., 1999; Arnone et al., 2006; Matsushita et al., 2012). To account for this variability, a slightly relaxed threshold value of 1.1 was adopted instead of the standard value of 1.

For waters where $R_{rs}^{412} : R_{rs}^{443} \leq 1.1$, additional classification was needed to capture more complex bio-optical regimes. A second index, $R_{rs}^{488} : R_{rs}^{547}$, was introduced to further differentiate among the remaining waters. According to the analytical model by Aiken (1995), cumulative absorption by all OACs typically declines beyond 488 nm. Notably, Chl-a exhibits minimal absorption at 547 nm, while particulate backscattering, particularly by phytoplankton and TSM, peaks in this region (Bricaud et al., 1998).

Therefore, the $R_{rs}^{488} : R_{rs}^{547}$ ratio captures the balance between absorption-dominated and scattering-dominated regimes. The observed values were grouped into three categories: $>$1.2, 0.9–1.2, and $<$0.9, corresponding to bio-optical types O_2^T, O_3^T, and O_4^T, respectively. Type O_4^T represented the most bio-optically complex waters. A regression analysis of the $R_{rs}^{488} : R_{rs}^{547}$

index against the total absorption ratio $a(488) : a(547)$ was conducted separately for each subgroup and for the combined dataset. The subgroups each showed strong correlations ($r^2 > 0.8$), whereas the combined dataset showed a weaker relationship ($r^2 < 0.6$), validating the classification scheme based on spectral median values.

Higher values of the $R_{rs}^{488} : R_{rs}^{547}$ ratio suggest stronger backscattering and lower cumulative absorption at 488 nm relative to 547 nm. This pattern reflects a stronger influence of TSM, since CDOM, a dissolved component, does not contribute to backscattering. Notably, both wavelengths are commonly available on most ocean colour satellite sensors, making this ratio a practical and widely applicable index for remote sensing-based assessments.

5.2.4 Radiant Heating Rate and other atmospheric condition parameters

The data for the underwater light field were used to compute the vertical profiles of spectrally integrated (from 400 nm to 700 nm) net irradiance (E_n). The computations depth z were as follows,

$$E_n(z) = E_u(z) - E_d(z) \tag{5.3}$$

where E_u and E_d are the upwelling and downwelling irradiance spectrally integrated over the visible range.

The RHR was estimated from these profiles following Ohlmann et al. (2000),

$$RHR(z) = \frac{E_n^{0^-} - E_n(z)}{\rho \times c_p \times z} \tag{5.4}$$

where 0^- denotes just below the surface, with ρ & c_p representing the seawater density at that depth z and the specific heat capacity under constant pressure, respectively.

As the goal of the chapter is to compare the spatial and temporal variations of RHR, the atmospheric and the solar insolation conditions were parametrised to analyse the variation of the environment. The solar irradiance index (SI) is of the following form,

$$SI = \frac{E_s}{E_s^{max}} \tag{5.5}$$

where E_s is the spectrally integrated incoming solar irradiance and E_s^{max} is the maximum value of E_s among all the in-situ observations measured during the coastal cruises. While the solar zenith angle may vary based on the study site location, time of observation, and the season, the computed index gives us a parameter to compare the incoming solar light at any location. The index also factors in variation brought about by errant cloud cover, even though all radiometric observations were conducted during cloud-free conditions.

The sea-surface albedo (α_s) which varies based on solar zenith angle, sea-surface roughness, and atmospheric transmittance conditions, was computed as per Ohlmann et al. (2000),

$$\alpha_s = 1 - \frac{E_n^{0^-}}{E_d^{0^+}} \tag{5.6}$$

where, $E_d^{0^+}$ is the incoming solar radiation spectrally integrated over the visible spectrum, extrapolated to just above the sea surface.

Thus, the energy flux reflected back at the sea surface E_{ref} and energy flux transmitted into the water column E_{tr} were computed as per the following,

$$E_{ref} = \alpha_s \times E_d^{0^+} \tag{5.7}$$

$$E_{tr} = (1 - \alpha_s) \times E_d^{0^+} \tag{5.8}$$

The transmittance of the solar energy through the water column was also computed as follows Ohlmann et al. (2000),

$$T_r = \frac{E_n(z)}{E_s} \tag{5.9}$$

The net surface heat flux (Q^0) was computed as follows Bignami et al. (1995) and Fairall et al. (2003),

$$Q^0 = Q^{lw} + Q^{sw} + Q^s + Q^l \tag{5.10}$$

where Q^{lw}, Q^{sw}, Q^s and Q^l are the net longwave, net shortwave, sensible heat flux and latent heat flux, respectively. Q^0 represents the total heat exchange between the atmosphere and ocean, where negative values represent net flux into the ocean.

5.2.5 Statistical analysis

The statistical techniques applied in the analysis of the bio-optical classification and the RHR comparison are listed below.

a. Pearson's correlation coefficient: Pearson's correlation coefficient (r) was often used between two parameters to evaluate the relationship between them. It was given by,

$$r = \frac{n(\sum_{i=1}^n x_i y_i) - (\sum_{i=1}^n x_i)(\sum_{i=1}^n y_i)}{\sqrt{[n(\sum_{i=1}^n x_i^2) - (\sum_{i=1}^n x_i)^2][n(\sum_{i=1}^n y_i^2) - (\sum_{i=1}^n y_i)^2]}} \tag{5.11}$$

where, x and y are the variables being compared.

b. Root mean square error: The root mean square error ($rmse$) is the average error between

the variables,

$$rmse = \sqrt{\frac{\sum_{i=1}^{n}(x_i - y_i)^2}{n}} \tag{5.12}$$

c. Mean percent error: The mean percent error (mpe) is the average error percentage between the variables, computed when the magnitude of the error is not significant.

$$mpe = \frac{1}{n} \times \frac{\sum_{i=1}^{n}(x_i - y_i)}{x_i} \times 100 \tag{5.13}$$

d. Wilcoxon rank-sum test: The nonparametric Wilcoxon rank-sum test was employed at a 1 % significance level to evaluate the null hypothesis that the parameters did not have a similar distribution among the bio-optical complexity classification (Sheskin, 2020). If the p-value was greater than 0.01, the null hypothesis was rejected

e. Kruskal-Wallis test: The bio-optical parameters were compared among each bio-optical complexity classification using the non-parametric Kruskal-Wallis test (Sheskin, 2020) at 5% significance level to evaluate if they had a similar distribution in their classification. If the p-value was greater than 0.05, the null hypothesis was rejected.

5.3 Results

The in-situ dataset was classified into four optical water types (O^T) based on the criteria detailed in Section 5.2.3. This clustering resulted in 72, 44, 15, and 21 sampling stations being categorised as O_1^T, O_2^T, O_3^T, and O_4^T, respectively. The spatial distribution of these O^Ts revealed a distinct pattern. Stations assigned to the least bio-optically complex class, O_1^T, were predominantly located in offshore regions. In contrast, nearshore waters were characterised mainly by O_2^T, while stations in proximity to major river mouths exhibited higher bio-optical complexity, falling into categories O_3^T and O_4^T (Figure 5.1).

The same pattern was evident in Figure 5.2, where deeper water columns were predominantly classified as O_1^T, while bio-optical complexity increased with decreasing depth. The mean depth of O_1^T waters was 104$\pm$55 m (approximately 30 km from the shore), decreasing to a mean depth of 17 m for O_4^T. This trend is consistent with the alignment of transects along river mouths, where the influence of riverine inputs and associated optically active constituents, whether transported from upstream or produced locally, likely contributes to the increasing bio-optical complexity in nearshore environments.

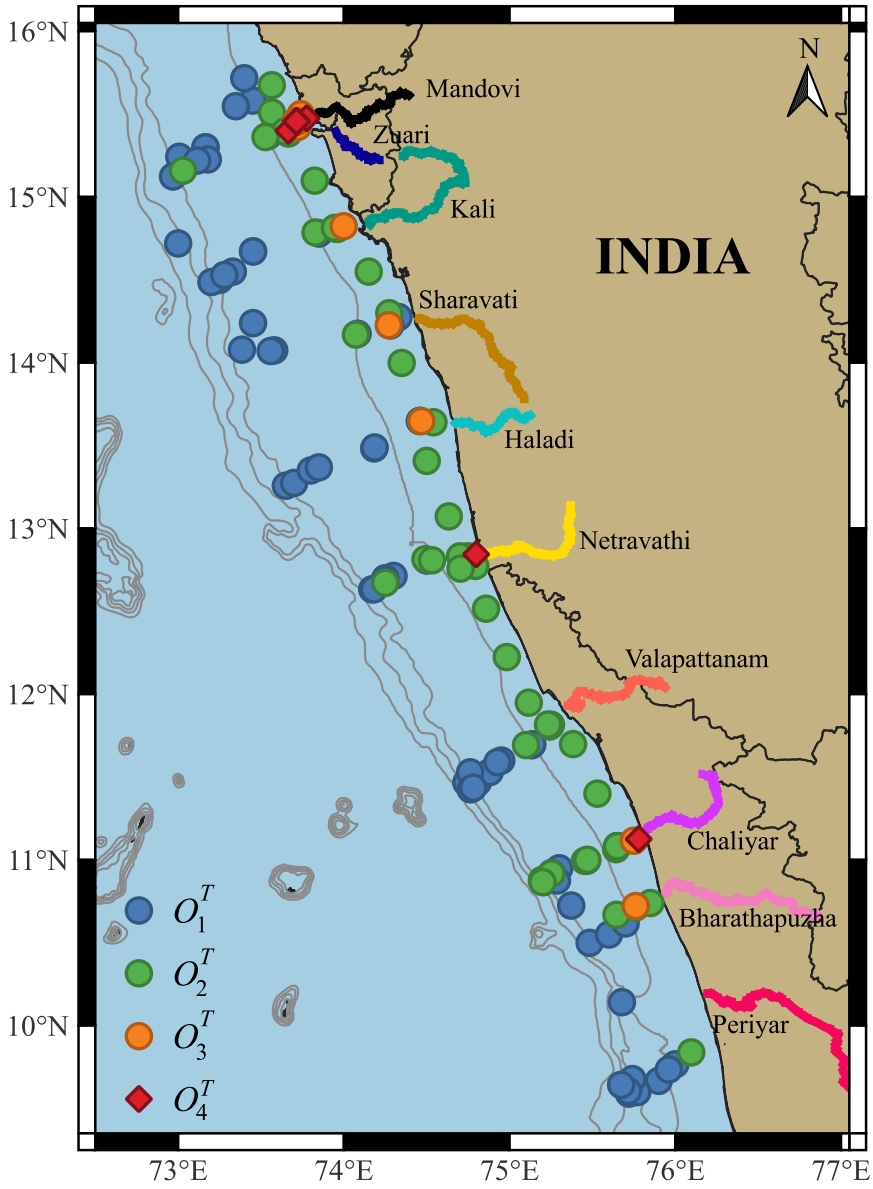

Figure 5.1: The map of EAS indicating the station location of each optical water types O_1^T, O_2^T, O_3^T and O_4^T

5.3.1 Optical Water Types and Spectral Remote Sensing Reflectance Variability

The distribution statistics of the OACs and their IOPs, grouped by optical water types, are summarised in Table 5.1. A consistent increasing trend in the concentrations of chlorophyll-a

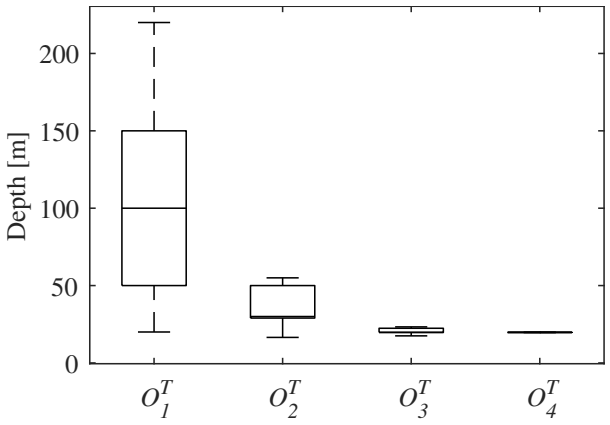

Figure 5.2: The boxplot depicting the depth distribution for each O^T

(c_{chl}) and TSM (c_{tsm}), as well as in their absorption coefficients at 440 nm (a_{chl}^{440} and a_{tsm}^{440}), and the $b_{b_p}^{650}$, was observed from O_1^T to O_4^T. However, the absorption coefficient of CDOM at 440 nm (a_{cdom}^{440}) did not show a clear increasing or decreasing trend across the water types.

Statistical analysis using the Kruskal–Wallis test revealed significant differences ($p<0.05$) among the classified water types for all parameters except a_{cdom}^{440}, for which the null hypothesis could not be rejected. Interestingly, the humification ratio (h_{ratio}) exhibited significant differences across water types, suggesting variations in the source or nature of CDOM even though its bulk absorption did not vary systematically. These results indicate that the bio-optical parameters vary distinctly across the classified water types and contribute differently to light attenuation in the water column.

The role of each OAC in controlling the bio-optical complexity of the water column was inferred from the averaged R_{rs} spectra of the classified water types (Figure 5.3). For O_1^T, the spectral shape of R_{rs} exhibited a gradual decline from 400 nm (0.012 ± 0.0025 sr^{-1}) to 700 nm (0.0008 ± 0.0006 sr^{-1}), with a prominent dip at 440 nm. Given that Chl-a has a primary absorption peak near 443 nm, this dip indicates a significant contribution of Chl-a to the absorption in these waters. Although the c_{chl} values for O_1^T were the lowest among all optical types (Table 5.1), the a_{chl}^{440} was markedly higher compared to the other two OACs.

Ternary plots further substantiate this observation, with Chl-a accounting for an average of 83% of the total absorption by OACs at 440 nm (Figure 5.4a). CDOM emerged as the second-most contributing absorber (13% of the absorption budget), with a_{cdom}^{440} values averaging 0.43 ± 0.42 m^{-1}. CDOM typically exhibits peak absorption in the shorter wavelengths, and this characteristic was evident in the spectral absorption curves (Figure 3.1). The h_{ratio} values

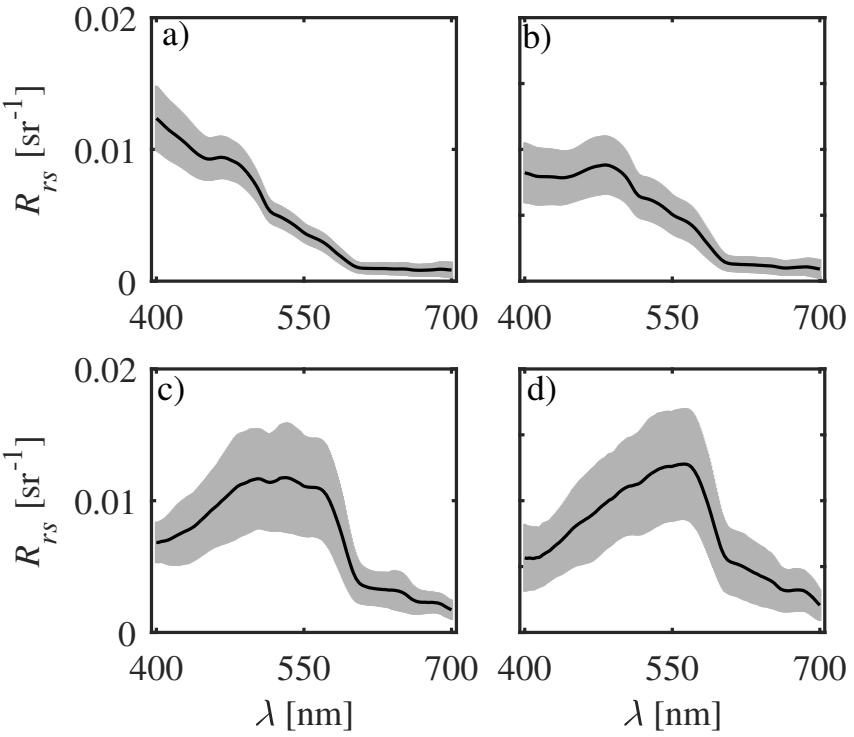

Figure 5.3: The mean spectral R_{rs} (solid line) along with their standard deviation (shaded area) for each O^T; a) O_1^T, b) O_2^T, c) O_3^T & d) O_4^T.

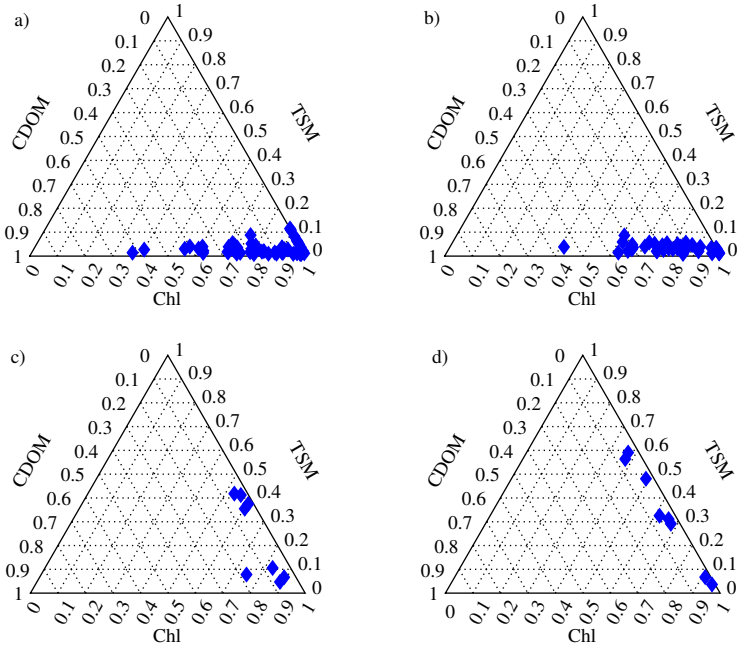

Figure 5.4: The ternary plots representing the contribution of each OAC in the absorption budget at 440 nm for each O^T; a) O_1^T, b) O_2^T, c) O_3^T & d) O_4^T.

of 5.81±3.83 suggest a phytoplanktonic origin of CDOM, likely produced via lysis or photo-exudation processes. While CDOM can reduce R_{rs} in the blue range due to its strong absorption (as per the inversion principle in Equation 3.1), the spectral R_{rs} values between 400-450 nm for O_1^T were the highest among all classified water types. This implies that, despite its presence, CDOM played a relatively minor role in shaping the bio-optical interactions for O_1^T waters.

The influence of TSM in O_1^T was also minimal. The concentrations, c_{tsm}, a_{tsm}^{440}, and $b_{b_p}^{650}$ were extremely low, especially when contrasted with values for O_3^T and O_4^T (Table 5.1). Radiometric estimates of $b_{b_p}^{650}$ showed differences of nearly an order of magnitude between the O_{1-2}^T and O_{3-4}^T groups (Figure 5.5), a trend mirrored by modelled $b_{b_p}^m$ values. The spectral backscattering values ($b_{b_p}^m$) decreased gradually across the visible spectrum, ranging from 0.003±0.0016 m^{-1} at 400 nm to 0.001±0.0007 m^{-1} at 700 nm (Figure 5.6a). However, the agreement between observed and modelled $b_{b_p}^{650}$ was poor for O_1^T ($r < 0.1$), with large root mean square error (0.0015 m^{-1}) and mean percentage error (871%), highlighting the limitations of QAA in estimating backscattering for these waters. Nevertheless, the consistently low values of c_{tsm}, a_{tsm}^{440}, and both measured and modelled b_{b_p} confirm that TSM contributes negligibly to both absorption and scattering in O_1^T.

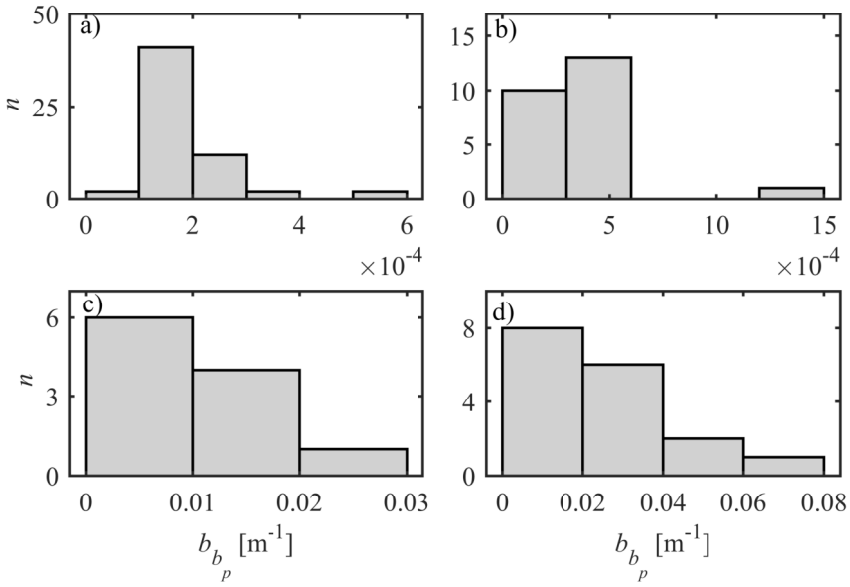

Figure 5.5: The frequency distribution of the radiometer estimated $b_{b_p}^{650}$ for each O^T; a) O_1^T, b) O_2^T, c) O_3^T & d) O_4^T.

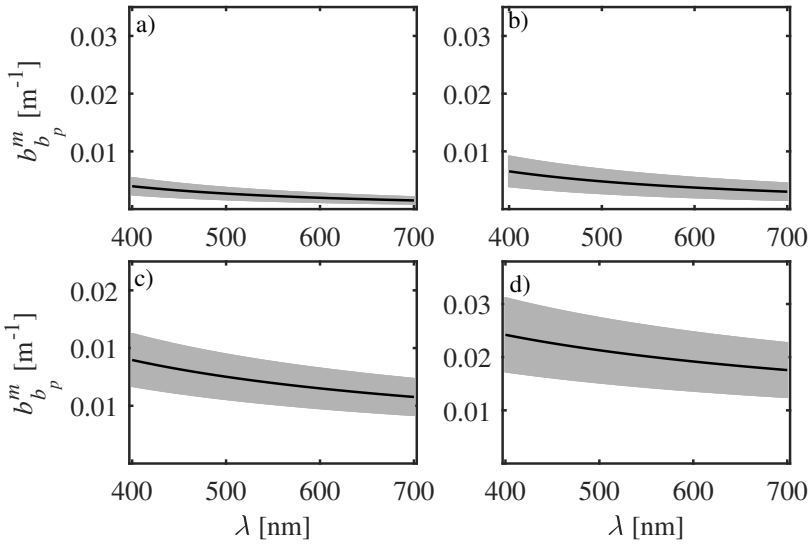

Figure 5.6: The mean particulate backscattering spectra modelled (solid line) and standard deviation (shaded area) for each O^T; a) O_1^T, b) O_2^T, c) O_3^T & d) O_4^T.

For O_2^T, the peak in the R_{rs} spectra shifted towards the 480–490 nm range, with a noticeable decline in reflectance values at the shorter wavelengths (Figure 5.3b). Compared to O_1^T, concentrations of all three optically active constituents, c_{chl}, c_{tsm}, a_{cdom}^{440}, a_{chl}^{440}, and a_{tsm}^{440}, increased (Table 5.1). Notably, the elevated h_{ratio} values suggest enhanced in-situ production of CDOM in these waters. The absolute values of a_{cdom}^{440}, along with its contribution to the overall absorption budget (≈18%; Figure 5.4b), were the highest among all O^Ts, indicating a more prominent influence of CDOM. The increased absorption by all three OACs likely contributed to the reduction in R_{rs} values in the 400-450 nm range.

Although $b_{b_p}^{650}$ values were higher than in O_1^T, the contribution of TSM to total absorption remained below 10%, suggesting that the observed increase in particulate backscattering was primarily driven by a rise in phytoplankton biomass (Table 5.1; Figures 5.5b and 5.4b). These results indicate that Chl-a and CDOM were the dominant contributors to light attenuation via absorption in O_2^T waters.

In contrast, the R_{rs} spectra for O_3^T and O_4^T were characteristic of optically complex and turbid waters (Figure 5.3c-d). For O_3^T, reflectance values decreased markedly in the shorter wavelengths (400–500 nm), with a relatively flat spectral signature (≈0.011±0.0039 sr^{-1}) between 500 and 570 nm. In O_4^T, the spectra displayed a distinct rise from 500 nm (0.01±0.0036 sr^{-1}) to 600 nm (0.012±0.0042 sr^{-1}), with even higher reflectance beyond 600 nm, indicating a shift in optical dominance.

There was a substantial increase in the concentrations of c_{chl}, c_{tsm}, a_{chl}^{440}, and a_{tsm}^{440} in O_{3-4}^T relative to O_{1-2}^T (Table 5.1). The progression from O_3^T to O_4^T revealed further increases from 3.18±1.88 $\mu g\ L^{-1}$, 16.87±13.52 mg L^{-1}, 7.90±4.16 m^{-1}, and 2.23±1.69 m^{-1} to 6.67±2.96 $\mu g\ L^{-1}$, 23.94±11.6 mg L^{-1}, 12.62±11.08 m^{-1}, and 3.34±1.16 m^{-1}, respectively. Similarly, $b_{b_p}^{650}$ values increased from 0.0094±0.0065 m^{-1} in O_3^T to 0.0258±0.0139 m^{-1} in O_4^T, with the distribution shifting towards larger values (Table 5.1, Figures 5.5c-d). This trend was also observed in the modelled backscattering spectra ($b_{b_p}^m$), which maintained similar spectral shapes but exhibited increased magnitudes across O_{3-4}^T (Figure 5.6).

The correlation between observed and modelled $b_{b_p}^{650}$ was poor for O_3^T ($r < 0.1$), but improved significantly for O_4^T ($r \approx 0.82$). However, both cases continued to show high error values (large $rmse$ and mpe), reflecting the limitations of QAA in accurately inverting R_{rs} spectra in optically complex coastal waters. Ternary plots for O_3^T and O_4^T (Figures 5.4c–d) demonstrated minimal CDOM contribution (typically <10%) and a notably increased role of TSM, contributing over 30% in O_4^T. The heightened particulate backscattering values and absorption patterns suggest that both Chl-a and TSM predominantly regulate the bio-optical dynamics in O_{3-4}^T. However, their relative influence varies with the optical type.

For O_4^T, the a_{cdom}^{440} and h_{ratio} values were 0.37±0.1 m^{-1} and 3.65±1.91, respectively. These relatively low h_{ratio} values suggest that the CDOM in O_4^T was largely of terrestrial origin. The geographical proximity of these waters to the river mouth indicates that the observed CDOM (as well as Chl-a and TSM) may have been introduced via riverine discharge. The comparatively reduced magnitude of land-derived CDOM, when contrasted with in-situ generated CDOM in EAS waters, aligns with spatial distribution patterns observed in the CDOM study over the MZE region presented in Chapter 4.

Table 5.1: Statistical summary (mean and standard deviation) of OACs and their associated parameters, classified according to the bio-optical complexity

	O_1^T	O_2^T	O_3^T	O_4^T
Total depth [m]	104±55	44±37	21±5	19±4
c_{chl} [μgL^{-1}]	0.46±0.37	0.64±0.5	3.18±1.88	6.67±2.96
c_{tsm} [mgL^{-1}]	3.08±1.01	3.16±1.34	16.87±13.52	23.94±11.6
a_{cdom}^{440} [m^{-1}]	0.43±0.42	0.54±0.42	0.5±0.29	0.37±0.1
a_{chl}^{440} [m^{-1}]	3.88 ± 2.09	5.57 ± 2.86	7.90 ± 4.16	12.62 ± 11.08
a_{tsm}^{440} [m^{-1}]	0.09 ± 0.07	0.16 ± 0.09	2.23 ± 1.69	3.34 ± 1.16
$b_{b_p}^{650}$ [m^{-1}]	0.00018±0.00008	0.0003±0.0002	0.0094±0.0065	0.0258±0.0139
h_{ratio}	5.81±3.83	8.23±4.42	6.22±4.45	3.65±1.91

5.3.2 Comparison of Radiant Heating Rates

a. SI and α_s: The variability in sampling locations and prevailing meteorological conditions during the observational period precluded a direct one-to-one comparison across the datasets. To address this, the distributions of the solar irradiance index (SI) and the surface wind speed parameter (α_s) were analyzed to support bio-optical classification of the water types. The mean values of SI exhibited minimal variation, ranging narrowly from 0.54 to 0.57 across all optical water types (O^Ts), with corresponding standard deviations between 0.21 and 0.26. This consistency indicates that the intensity of incident solar irradiance during the field measurements was broadly comparable across sites. Supporting this observation, a Kruskal-Wallis non-parametric test at the 5% significance level failed to reject the null hypothesis, confirming no statistically significant differences in the distribution of incident solar energy among the different O^Ts.

Similarly, the distribution of the surface wind speed parameter, α_s, was statistically similar between O_1^T and O_2^T, which showed mean values of 5.58±0.26% and 5.60±0.44%,

respectively. In contrast, α_s values increased for O_3^T and O_4^T, with means of 6.37±0.84% and 6.46±0.92%, respectively. This gradation is consistent with expectations for stations situated closer to the coastline, where enhanced wind-induced surface roughness contributes to higher surface wind speeds (Ohlmann et al., 2000). The computed average reference irradiance values (E_{ref}) also exhibited a gradual increase, from 14.09 Wm^{-2} for O_1^T to 17.09 Wm^{-2} for O_4^T, while their standard deviations remained within comparable ranges, further indicating similar atmospheric conditions across the sampled water types.

Cloud cover can affect not only the intensity of the incoming solar radiation but also its angular distribution and spectral quality, which in turn influence underwater light fields (Ohlmann et al., 2000). The spectrally integrated transmitted irradiance (E_{tr}) averaged approximately 240 Wm^{-2} across all O^Ts, with standard deviations ranging between 96 and 116 Wm^{-2}. Another Kruskal-Wallis test confirmed that these differences in E_{tr} among the O^Ts were not statistically significant. Collectively, these results demonstrate broadly comparable atmospheric forcing conditions during the measurement campaigns, thereby supporting the validity of subsequent bio-optical comparisons across the different water types.

b. Surface k_d^{PAR} and RHR: The cumulative influence of OACs across the bio-optically complex water types was quantitatively assessed using the diffuse attenuation coefficient for downwelling irradiance integrated over the PAR spectral range (k_d^{PAR}). the property vertically averaged over the upper 2 meters of the water column, denoted as $\int_0^2 k_d^{PAR}\, dz$. The measured values exhibited a clear increasing trend with water type complexity, recorded as 0.16 ± 0.06 m^{-1} for O_1^T, 0.18 ± 0.07 m^{-1} for O_2^T, 0.28 ± 0.17 m^{-1} for O_3^T, and 0.47 ± 0.20 m^{-1} for O_4^T.

In parallel, the vertically averaged RHR, integrated over the same depth interval $\int_0^2 RHR\, dz$, demonstrated corresponding values of 0.042 °C hr^{-1}, 0.038 °C hr^{-1}, 0.061 °C hr^{-1}, and 0.145 °C hr^{-1} for O_1^T through O_4^T, respectively. Notably, the differences between O_1^T and O_2^T were minimal, indicating similar bio-optical conditions and light attenuation characteristics for these two water types. However, a pronounced and consistent increase in both the attenuation coefficient and the radiant heating rate was observed progressing from O_2^T to the more optically complex water types O_3^T and O_4^T.

This observed trend strongly implies that the variability in surface radiant heating rates is

intricately linked to the bio-optical complexity of the water column, which in turn is governed by the concentration and composition of OACs. Increased attenuation in more complex water types reduces light penetration, concentrating solar energy absorption nearer to the surface and thus elevating surface heating rates. These findings underscore the importance of accounting for the specific bio-optical characteristics of coastal and estuarine waters in models predicting heat distribution and associated ecological impacts.

Table 5.2: Statistical summary (mean and standard deviation) of the solar irradiance index (SI), surface albedo (α_s), energy transfer through the surface layers and the subsequent RHR and coefficient of diffuse attenuation of downwelling irradiance for surface waters, categorised by optical water type.

	O_1^T	O_2^T	O_3^T	O_4^T
SI	0.54 ± 0.24	0.55 ± 0.22	0.55 ± 0.26	0.57 ± 0.23
α_s [%]	5.58 ± 0.26	5.6 ± 0.44	6.37 ± 0.84	6.46 ± 0.92
E_{ref} [Wm^{-2}]	14.09 ± 6.28	14.59 ± 5.71	15.87 ± 7.04	17.11 ± 7.48
E_{tr} [Wm^{-2}]	240.22 ± 109.72	246.18 ± 99.54	239.2 ± 116.4	246.1 ± 96.71
$\int_0^2 k_d^{PAR}$ [m^{-1}]	0.16 ± 0.06	0.18 ± 0.07	0.28 ± 0.17	0.47 ± 0.2
$\int_0^2 RHR$ [°C hr^{-1}]	0.042 ± 0.0304	0.038 ± 0.024	0.061 ± 0.0492	0.145 ± 0.084

c. Vertical variability of RHR: The vertical variability of RHR further highlighted differences across the classified optical water types. The mean euphotic depths (z^e), defined as the depth where PAR falls to 1% of its surface value, ranged substantially from 69 m in the relatively clear offshore waters (O_1^T) to only 12 m in the most bio-optically complex and turbid waters (O_4^T) (Table 5.3). Despite this marked variation in light penetration depth, the integrated heating of the water column up to z^e, denoted as $\int_0^{z^e} RHR\,dz$, remained remarkably consistent across water types, varying between 0.19 and 0.23 °C hr^{-1} with similar standard deviations.

A Kruskal-Wallis non-parametric test confirmed the lack of statistically significant differences in the integrated heating rates across the optical water types ($p > 0.05$), indicating that the total energy absorbed within the euphotic zone is fairly uniform despite the contrasting bio-optical properties. This implies a compensatory mechanism wherein shallower euphotic depths in turbid waters are offset by higher near-surface absorption rates, resulting in comparable cumulative heating.

However, when considering the fraction of incident solar energy retained within the euphotic depth, a significant difference emerged. Specifically, O_4^T retained, on average, only

about 98% of the incident energy, significantly less than the other water types. Here, the Kruskal-Wallis test rejected the null hypothesis ($p < 0.05$), suggesting enhanced heat losses in the most complex waters. These losses are likely attributable to increased backscattering and absorption by suspended particulate matter near the surface, which redirects or reflects energy out of the water column.

The best-fit first-order exponential profiles for key vertical optical parameters, E_d, $b_{b_p}^{650}$, and k_d^{PAR}, were plotted alongside the estimated vertical profiles of T_r and RHR for each O^T in Figure 5.7. The data exhibited strong correlations between RHR and k_d^{PAR} across all water types, consistent with the conceptual understanding that light attenuation modulates the vertical distribution of heating. An inverse relationship was observed between the magnitude of absorption and transmission, confirming that more absorptive waters exhibit lower transmittance.

Statistical analyses using the Wilcoxon rank-sum test revealed that the vertical profiles of RHR were statistically similar ($p > 0.01$) to those of $b_{b_p}^{650}$, k_d^{PAR}, and T_r in the less complex water types O_1^T and O_2^T. Conversely, in the more bio-optically complex water types O_3^T and O_4^T, these similarities were absent, with p-values falling below 0.01. This divergence suggests that increasing particulate concentrations and optical complexity introduce heterogeneity in vertical light attenuation and heating patterns.

It is important to note that the absence of depth-resolved inherent optical property (IOP) measurements specific to individual optically active constituents (such as CDOM, Chl-a, and TSM) limits the precise attribution of observed vertical variability in RHR and associated optical parameters to particular drivers. Future studies incorporating detailed vertical profiling of IOPs for each constituent will be essential to disentangle these complex interactions.

Table 5.3: Columnar radiant heating rates (RHR) and euphotic depths (z^e) for different optical water types (O_i^T). Values are expressed as mean $\pm$ standard deviation.

	O_1^T	O_2^T	O_3^T	O_4^T
z^e [m]	69 ± 27	33 ± 17	17 ± 5	12 ± 4
$\int_0^{z^e} RHR$ [°C hr^{-1}]	0.225 ± 0.118	0.214 ± 0.096	0.191 ± 0.097	0.21 ± 0.12
% of energy trapped in the euphotic depth	99.79 ± 0.36	99.83 ± 0.39	99.42 ± 0.74	97.98 ± 2.53

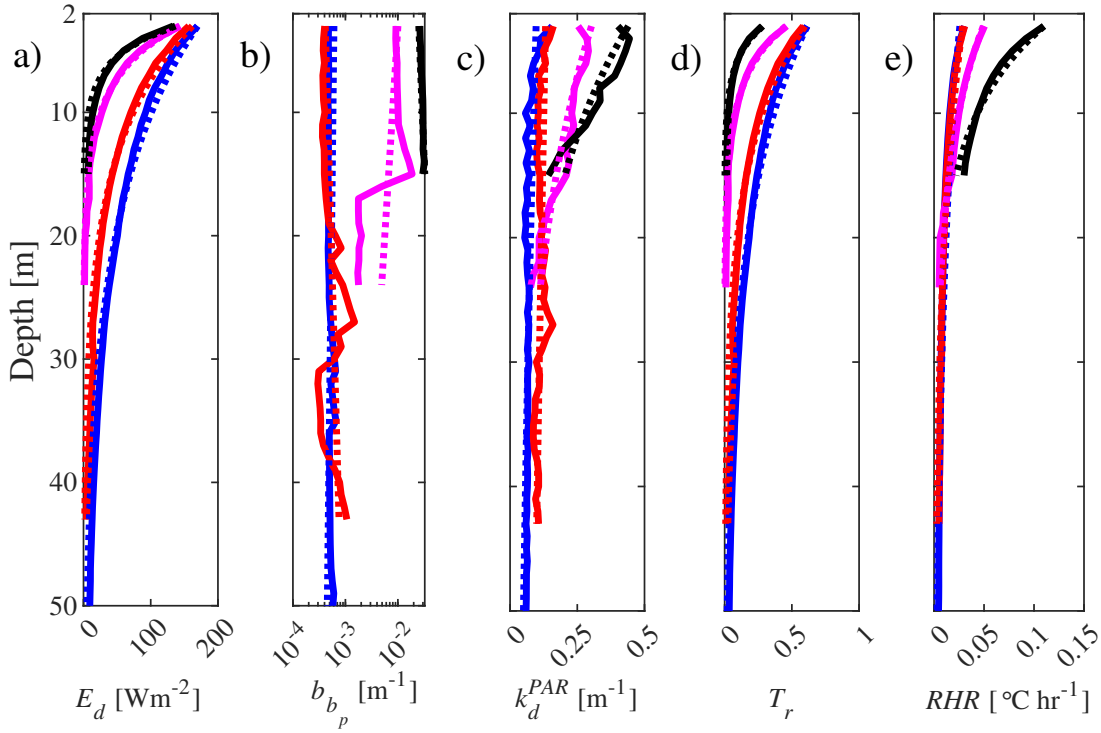

Figure 5.7: The vertical variability of mean (solid line) and best-fit curve (dotted line) of a) downwelling irradiance, b) particulate backscatter, c) diffuse attenuation coefficient of downwelling irradiance, d) transmission, and, e) RHR for the optical classification O_1^T (blue), O_2^T (red), O_3^T (magenta) & O_4^T (black).

5.4 Discussion

5.4.1 Bio-optical Variability Across Water Types

The dataset analysed in this chapter was classified according to the bio-optical influence of OACs within the water column. Such bio-optical complexity is inherently dynamic, shaped by seasonal and diurnal fluctuations in concentrations of constituents such CDOM, Chl-a, and TSM. Despite temporal variability, the clustering of data collected across pre-monsoon and post-monsoon periods revealed a clear spatial trend: bio-optical complexity consistently decreased with increasing distance from the coastline. This spatial gradient reflects the combined influence of terrestrial inputs, biological productivity, and hydrodynamic processes characteristic of the EAS.

The offshore waters were predominantly characterised by the optical water type O_1^T, where light absorption and scattering were primarily controlled by Chl-a and CDOM. This is consistent with previous studies indicating that even highly productive upwelling systems such as the EAS exhibit elevated CDOM concentrations relative to typical open ocean values (Kumar et al., 2000; Nelson and Siegel, 2013). Moving shoreward, water type O_2^T demonstrated further elevated CDOM absorption supplementing the Chl-a signal, while TSM concentrations remained relatively stable. These changes manifested in distinctive spectral features, including the flattening of R_{rs} spectra at wavelengths below 450 nm, indicative of increased absorption by CDOM and other dissolved substances (Kirk, 1994).

The more bio-optically complex water types O_3^T and O_4^T showed pronounced reductions in reflectance within the blue wavelengths due to increased absorption by the collective OAC pool, including particulate matter, which also enhanced backscattering in the green and red wavelengths. The strong attenuation of light at wavelengths beyond 600 nm correlated with increased TSM absorption and particulate backscattering, highlighting the dominant role of suspended sediments in these nearshore environments. This spectral behaviour underpins the fundamental influence of OACs on underwater light fields and emphasises the intricate interplay of absorption and scattering processes governing coastal optical complexity.

While infrared radiation (>700 nm) is absorbed almost completely within the upper few meters of the water column (Mobley, 2022), the visible spectrum remains critically modulated by the relative concentrations and properties of Chl-a, CDOM, and TSM. These constituents directly regulate underwater solar transmission and, consequently, the vertical distribution of radiant heating, with important implications for ecosystem function and physical oceanographic processes.

5.4.2 Estimates of Radiant Heating Rate

The surface layer ($\sim$ top 2 m) radiant heating rate, RHR, varied significantly across the classified optical water types (Table 5.4). The O_1^T in the EAS displayed mean RHR values of 0.042 °C hr^{-1}, which is notably higher, by at least a factor of three, than previously reported open ocean values in the Arabian Sea despite comparable Chl-a levels (Pradhan et al., 2005). This highlights the enhanced heating potential in coastal regimes influenced by elevated CDOM and particulate matter.

Comparative studies in the Bay of Bengal also revealed similar RHR values across diverse water types despite lower Chl-a concentrations, underscoring the importance of CDOM and suspended particles in modulating radiant heating (Parida et al., 2022). Modeling efforts in these regions suggest that even small increases in phytoplankton biomass can induce significant warming at the surface, influencing thermal stratification and biogeochemical cycling.

In Arctic shelf seas such as the Laptev Sea, elevated CDOM concentrations contribute substantially to surface energy attenuation, increasing heating rates by up to 0.6 °C day^{-1} (approximately 0.05 °C hr^{-1}), further supporting the critical role of CDOM absorption in shaping RHR in coastal environments (Soppa et al., 2019). Similarly, observations in temperate coastal waters of New Jersey exhibit RHR values comparable to the most bio-optically complex water types in this study, despite differences in particulate backscattering. These observations emphasise the importance of considering both absorption and scattering properties to accurately characterise heat absorption in coastal systems (Zaneveld et al., 1981).

5.4.3 Implications for the Net Heat Flux and Vertical Structure

The bio-optical variability also manifested in the vertical distribution of RHR. Elevated b_{b_p} and k_d^{PAR} in surface waters intensified heat absorption near the surface but limited energy penetration into deeper layers. The vertical profiles of RHR positively correlated with k_d^{PAR} and inversely correlated with T_r. This resulted in surprisingly high heating rates in O_4^T comparable to those in optically clearer waters with euphotic depths three to five times greater (Table 5.3). Such enhanced surface heating in turbid waters may have profound implications for local thermal stratification and feedbacks to regional climate processes (Soppa et al., 2019).

A focused case study using time-series data from a cruise in January 2017 in the Mandovi-Zuari estuarine region illustrated how bio-optical complexity and variations in constituent absorption influence heat flux to the atmosphere (Table 5.5). Two contrasting days showed significant differences in RHR and optical classifications despite similar incident solar radiation. These shifts were driven by changes in particulate composition and relative contributions of CDOM and Chl-a, which modulated backscattering efficiency and solar transmission, ultimately

impacting surface heating rates.

This analysis highlights the importance of resolving constituent-specific optical properties to understand and predict variability in radiant heating, emphasising the need for comprehensive in-situ measurements alongside remote sensing approaches.

5.4.4 Limitations and Future Directions

While this study provides valuable insights into the role of bio-optical complexity in modulating radiant heating, it is limited by the absence of detailed ecological and physical process data that influence OAC distributions. Events such as algal blooms, upwelling, or frontal dynamics can significantly alter optical properties and heating independently, and these processes were not explicitly considered here. Future work integrating biogeochemical and physical oceanographic measurements will be critical to fully disentangle the drivers of RHR variability in coastal waters.

Furthermore, depth-resolved measurements of inherent optical properties specific to CDOM, Chl-a, and TSM would greatly enhance the ability to attribute vertical heating patterns to individual constituents. Combining such data with high-resolution satellite imagery and advanced bio-optical models promises to improve predictions of heat fluxes and their ecological and climatic consequences in dynamic coastal systems.

5.5 Conclusion

This chapter developed a robust bio-optical complexity classification framework for the coastal EAS, delineating four distinct O^Ts based on the characteristic interactions of OACs influencing R_{rs} spectra. Spectral indices were carefully constructed to isolate wavelength regions most sensitive to IOPs of specific OACs, enabling discrimination among complex coastal water types. Specifically, the ratio $R_{rs}^{412} : R_{rs}^{443}$ effectively differentiated waters dominated by Chl-a absorption from those with significant contributions from other absorbing substances such as CDOM and TSM. Concurrently, the ratio $R_{rs}^{488} : R_{rs}^{547}$ served as an indicator to distinguish absorption-dominated waters from those where scattering processes, often associated with terrigenous particulate matter, were more pronounced.

The classification captured a clear spatial gradient in bio-optical complexity, extending from the relatively simple offshore waters classified as O_1^T, characterised by lower constituent concentrations and clearer optical conditions, to the highly complex nearshore and estuarine zones classified as O_4^T, where elevated concentrations of CDOM, Chl-a, and TSM significantly modulate light attenuation and backscattering. Notably, this spatial distribution pattern of optical types remained consistent across pre-monsoon and post-monsoon seasons, underscoring the

stability of the bio-optical framework despite seasonal forcing and hydrodynamic variability.

Further, this work elucidated how the distribution and optical effects of bio-optical constituents govern RHR within the warm coastal waters of the EAS. Surface-layer RHR showed a pronounced increase moving from offshore to nearshore environments, closely tracking the k_d^{PAR} and reflecting the combined influence of absorption and scattering processes. Remarkably, the mean surface RHR in the most optically complex water type, O_4^T, was approximately an order of magnitude greater than in O_1^T, highlighting the critical role of bio-optical complexity in modulating heat absorption in coastal zones. Moreover, the observed surface heating rates exceeded previously reported values for comparable optical regimes, emphasising the need to consider regional bio-optical variability in heat budget studies.

Despite substantial variation in surface heating rates, the euphotic depth-integrated RHR remained surprisingly uniform across all four optical types. This result points to a compensatory mechanism wherein elevated concentrations of optically active constituents in shallower, nearshore waters enhance localised radiant heating despite concomitant reductions in light penetration depth. Such compensation underscores the importance of accounting for vertical heterogeneity and constituent-specific optical properties when assessing heat fluxes in coastal environments.

In summary, the findings presented herein reinforce the significance of bio-optical feedback in controlling radiant heating patterns within optically complex coastal waters. Incorporating such detailed bio-optical characterisations into global ocean heat budget assessments and coupled climate models is essential for improving predictions of coastal thermal dynamics, with direct implications for ecosystem functioning, stratification, and regional climate variability.

Table 5.4: A comparison with past literature studies detailing the bio-optical conditions of the water and their corresponding radiant heating rates (RHR).

Sr. No.	Study	Location	Water Type	Surface Layer Depth [m]	Surface RHR [°C hr^{-1}]
1	Present Study	Coastal EAS	O_1^T O_2^T O_3^T O_4^T	2	0.042 0.038 0.061 0.145
2	(Soppa et al., 2019)	Laptev Sea Shelf waters	Coastal	2	0.02–0.08
3	(Chang and Dickey, 2004)	New York Bight	Coastal	5	*0.15
4	(Hill, 2008)	Chukchi Shelf - Spring Chukchi Shelf - Summer	Coastal	2	0.085 0.07
5	(Zaneveld et al., 1981)	N/A	Jerlov Ocean Type 1 Jerlov Ocean Type 1	20 10	0.008 0.026
6	(Pradhan et al., 2005)	Arabian Warm Sea Pool	Open Ocean	10	0.015
7	(Parida et al., 2022)	Southern Bay of Bengal	Open Ocean	SST	0.01–0.14
8	(Strutton and Chavez, 2004)	Equatorial Pacific	Open Ocean	SST	0.0028
9	(Siegel et al., 1995)	Western equatorial warm pool of Pacific Ocean	Open Ocean	40	0.0003

Table 5.5: A comparison between O^T, R_{rs} ratios, SI, surface RHR, T_r and ratio percentage of spectrally integrated (over 400-700 nm) specific absorption by CDOM, Chl-a, and TSM to the spectrally integrated cumulative specific absorption by all OAC and estimated backscattering at 650 nm among the stations with similar heat flux using the timeseries data collected in January 2017.

Parameters	Day of 2017			
	12th	14th	15th	16th
Q_0 [W m^{-2}]	-10.15	-6.9	-37.2	-39.2
SI	0.7	0.75	0.68	0.66
O^T	4	1	4	3
$\frac{a_{cdom}}{a_T}$ [%]	26.43	24.19	17.63	29.74
$\frac{a_{chl}}{a_T}$ [%]	60.78	57.88	62.1	53.34
$\frac{a_{tsm}}{a_T}$ [%]	12.79	17.93	20.27	16.92
$b_{b_p}^{650}$ [m^{-1}]	0.0461	0.0199	0.0157	0.0118
$\int_0^2 T_r$ [%]	34.4	49.2	72.6	32.8
$\int_0^2 RHR$ [%]	0.16	0.11	0.02	0.18

Chapter 6

Conclusion

6.1 Summary

This thesis significantly advances the understanding of bio-optical variability in estuarine and coastal waters, with particular emphasis on chromophoric dissolved organic matter (CDOM) and its optical and ecological implications. A novel semi-analytical algorithm was developed to robustly retrieve CDOM absorption coefficients at 440 nm (a_{cdom}^{440}) across a wide range of globally distributed turbid waters. Furthermore, the study comprehensively investigated the influence of all major optically active constituents (OACs) on remote sensing reflectance (R_{rs}) and radiant heating rates (RHR) in the coastal waters of the eastern Arabian Sea.

The key findings of the work are summarised as follows,

a. A novel three-wavelength semi-analytical algorithm was formulated and rigorously validated against diverse optical water types worldwide. The index is structured to directly capture CDOM absorption variation at $\lambda_1 = 412$ nm, with a differential term between λ_1 and $\lambda_2 = 490$ nm that effectively compensates for absorption contributions from Chl-a, TSM, and pure seawater. The third wavelength ($\lambda_3 = 560$ nm) normalises the index, selected to minimise interference from particulate attenuation, thereby isolating the CDOM signal in the R_{rs} spectra. The final algorithm was,

$$a_{cdom}^{440} = -0.01368x^2 + 0.102x + 0.02295, \quad x = \left(\frac{1}{R_{rs}^{412}} - \frac{1}{R_{rs}^{490}}\right) \times R_{rs}^{560}$$

b. The algorithm was developed and tested using a comprehensive global dataset spanning highly turbid estuarine and coastal waters, encompassing a_{cdom}^{440} values from 0.0056 to 1.1843 m^{-1} and diffuse attenuation coefficients k_d^{490} from 0.019 to 3.39 m^{-1}. This dataset

represented conditions where CDOM contributed between 5% and 95% of the total absorption by OACs. Regional evaluations in the Gulf of Mexico (GoM), Chesapeake and Delaware Bays (CDB), and Mandovi-Zuari Estuarine network (MZE) showed average CDOM contributions of 86%, 45%, and 18%, respectively, demonstrating the algorithm's broad applicability across variable bio-optical conditions.

c. The developed algorithm consistently outperformed existing CDOM retrieval methods, including multiple linear regression, machine learning techniques, and established semi-analytical algorithms, across global and regional datasets. While machine learning and regression models exhibited reduced accuracy outside their training domains, and traditional algorithms struggled in optically complex waters dominated by Chl-a and TSM, the proposed method maintained superior accuracy, robustness, and generalisation.

d. Satellite validation using Ocean and Land Colour Instrument (OLCI) and Moderate Resolution Imaging Spectroradiometer (MODIS) datasets further confirmed the algorithm's efficacy, surpassing competing methods in accuracy and stability for retrieving a_{cdom}^{440} across diverse coastal environments.

e. For the first time, this thesis presents an annual, monthly-averaged spatial distribution of CDOM in the MZE and CDB estuarine-coastal systems derived entirely from satellite remote sensing. These maps align well with historical in-situ observations and capture key hydrodynamic processes, such as freshwater plume formation, estuarine mixing regimes, and seasonal in-situ CDOM production associated with phytoplankton degradation.

f. A novel bio-optical classification scheme was introduced for coastal waters of the EAS, identifying four optical water types (O_1^T through O_4^T) spanning a gradient from offshore oligotrophic to nearshore highly turbid, CDOM-rich conditions. This classification was temporally stable across seasons, being dictated primarily by constituent interactions rather than seasonal forcing.

g. The study quantified the influence of bio-optical constituents on surface RHR, demonstrating that the most optically complex waters experienced surface RHR values an order of magnitude greater (0.14 °C hr^{-1}) than the least complex waters. Despite variability in euphotic depths, the total radiant heating integrated over the water column remained similar across the optical types, highlighting a compensatory mechanism of enhanced absorption in shallower, more turbid waters.

h. Finally, the thesis underscores the importance of integrating bio-optical feedback, especially in turbid coastal zones, into global ocean heat budget models and climate projections, due to their potential influence on local atmospheric dynamics and coastal ecosystem functioning.

6.2 Significance of the Study

The semi-analytical algorithm developed in this thesis represents a significant advancement for remote sensing of CDOM in optically complex, turbid coastal waters, where traditional methods often fail. By effectively disentangling CDOM signals from interfering absorption by phytoplankton and suspended sediments, this method enables more accurate mapping of dissolved organic matter dynamics critical to understanding carbon cycling, nutrient fluxes, and ecosystem health in estuarine and coastal systems.

Such improved retrieval capabilities have direct societal implications, particularly in regions like the Arabian Sea, where the increasing frequency of harmful algal blooms, hypoxia, and organic pollution threatens fisheries and coastal livelihoods. The ability to monitor CDOM more precisely also opens avenues for early warning systems for waterborne diseases linked to organic pollution, such as cholera, enhancing public health responses.

Moreover, the framework established here lays a foundation for integrating CDOM monitoring with other bio-optical parameters such as chlorophyll and suspended particulate matter, facilitating holistic ecosystem modelling. Such integrated approaches are essential for accurately simulating light penetration, heat budgets, and biogeochemical processes in coastal waters, which in turn inform climate change projections and coastal management strategies.

6.3 Future Scope

Building on the outcomes of this thesis, several promising directions emerge for future research,

- Extension to Hyperspectral Remote Sensing: The algorithm could be adapted for hyperspectral satellite sensors (e.g., PRISMA, EnMAP) offering finer spectral resolution. This may enhance discrimination of CDOM from other OACs and enable retrieval of additional dissolved organic matter optical properties.

- Temporal Resolution and Event Monitoring: Employing higher temporal resolution satellite data or geostationary platforms could enable tracking of episodic events such as monsoonal floods, algal blooms, or pollution discharges with improved temporal fidelity.

- Incorporation of 3D Optical Properties: Vertical profiling of OACs and light fields via autonomous platforms (e.g., gliders, floats) combined with remote sensing could improve understanding of vertical heterogeneity in CDOM and its effects on radiative heating.
- Impact Assessment under Climate Change Scenarios: Using the algorithm to evaluate how climate-driven shifts in freshwater input, organic matter loading, and temperature affect bio-optical states and coastal heat budgets could inform adaptive management strategies.
- Development of Operational Monitoring Systems: Translating this research into operational frameworks for real-time monitoring of coastal water quality and organic pollution to assist regulatory agencies and resource managers.

In conclusion, the tools and insights developed in this thesis provide a critical step toward more comprehensive and accurate monitoring of dissolved organic matter and bio-optical complexity in estuarine and coastal environments, with wide-ranging implications for marine ecology, climate science, and coastal resource management.

Bibliography

Adhikari, A. and Menon, H. B. (2022). A bio-optical numerical approach for remote retrieval of total suspended matter from turbid waters. *Journal of the Indian Society of Remote Sensing*, 50(9):1773–1786.

Adhikari, A., Menon, H. B., and Lotliker, A. (2023). Coupling of hydrography and bio-optical constituents in a shallow optically complex region using ten years of in-situ data. *ISPRS Journal of Photogrammetry and Remote Sensing*, 202:499–511.

Aiken, J. (1995). The seawifs czcs type pigment algorithm. nasa tech memo 104566. Technical report, NASA Goddard Space Flight Center.

Arnone, R., Loisel, H., Carder, K., Boss, E., Maritorena, S., and Lee, Z. (2006). Examples of iop applications. In Lee, Z.-P., editor, *Remote Sensing of Inherent Optical Properties: Fundamentals, Tests of Algorithms, and Applications*, volume 5 of *Reports of the International Ocean-Colour Coordinating Group*, pages 103–108. IOCCG, Dartmouth, Canada.

Arrigo, K. R. and Brown, C. W. (1996). Impact of chromophoric dissolved organic matter on uv inhibition of primary productivity in the sea. *Marine Ecology Progress Series*, 140:207–216.

Ashphaq, M., K., Srivastava, P., and Mitra, D. (2023). Preliminary examination of influence of chlorophyll, total suspended material, and turbidity on satellite derived-bathymetry estimation in coastal turbid water. *Regional Studies in Marine Science*, 62:102920.

Aurin, D., Mannino, A., and Franz, B. (2013). Spatially resolving ocean color and sediment dispersion in river plumes, coastal systems, and continental shelf waters. *Remote Sensing of Environment*, 137:212–225.

Aurin, D., Mannino, A., and Lary, D. J. (2018). Remote sensing of cdom, cdom spectral slope, and dissolved organic carbon in the global ocean. *Applied Sciences (Switzerland)*, 8.

Babichenko, S., Leeben, A., Poryvkina, L., van der Wagt, R., and de Vos, F. (2000). Fluorescent screening of phytoplankton and organic compounds in sea water. *Journal of Environmental Monitoring*, 2:378–383.

Bai, Y., Pan, D., Cai, W. J., He, X., Wang, D., Tao, B., and Zhu, Q. (2013). Remote sensing of salinity from satellite-derived cdom in the changjiang river dominated east china sea. *Journal of Geophysical Research: Oceans*, 118:227–243.

Bélanger, S., Babin, M., and Tremblay, J.-É. (2013). Increasing cloudiness in arctic damps the increase in phytoplankton primary production due to sea ice receding. *Biogeosciences*, 10(6):4087–4101.

Bignami, F., Marullo, S., Santoleri, R., and Schiano, M. E. (1995). Longwave radiation budget in the mediterranean sea. *Journal of Geophysical Research*, 100:2501–2514.

Binding, C. E. and Bowers, D. G. (2003). Measuring the salinity of the clyde sea from remotely sensed ocean colour. *Estuarine, Coastal and Shelf Science*, 57:605–611.

Blondeau-Patissier, D., Gower, J. F., Dekker, A. G., Phinn, S. R., and Brando, V. E. (2014). A review of ocean color remote sensing methods and statistical techniques for the detection, mapping and analysis of phytoplankton blooms in coastal and open oceans. *Progress in Oceanography*, 123:123–144.

Blough, N. V. and Del Vecchio, R. (2002). Chromophoric DOM in the coastal environment. In Hansell, D. A. and Carlson, C. A., editors, *Biogeochemistry of Marine Dissolved Organic Matter*, pages 509–546. Academic Press, San Diego.

Bowers, D. G. and Binding, C. E. (2006). The optical properties of mineral suspended particles: A review and synthesis. *Estuarine, Coastal and Shelf Science*, 67:219–230.

Bracher, A., Bouman, H. A., Brewin, R. J. W., Bricaud, A., Brotas, V., Ciotti, A. M., Clementson, L., Devred, E., Di Cicco, A., Dutkiewicz, S., Hardman-Mountford, N. J., Hickman, A. E., Hieronymi, M., Hirata, T., Losa, S. N., Mouw, C. B., Organelli, E., Raitsos, D. E., Uitz, J., Vogt, M., and Wolanin, A. (2017). Obtaining phytoplankton diversity from ocean color: A scientific roadmap for future development. *Frontiers in Marine Science*, 4.

Branco, A. B. and Kremer, J. N. (2005). The relative importance of chlorophyll and colored dissolved organic matter (cdom) to the prediction of the diffuse attenuation coefficient in shallow estuaries. *Estuaries*, 28:643–652.

Brando, V. and Dekker, A. (2003). Satellite hyperspectral remote sensing for estimating estuarine and coastal water quality. *IEEE Transactions on Geoscience and Remote Sensing*, 41(6):1378–1387.

Brando, V. E., Lovell, J. L., King, E. A., Boadle, D., Scott, R., and Schroeder, T. (2016). The potential of autonomous ship-borne hyperspectral radiometers for the validation of ocean color radiometry data. *Remote Sensing*, 8(2):150.

Bricaud, A., Babin, M., Morel, A., and Claustre, H. (1995). Variability in the chlorophyll-specific absorption coefficients of natural phytoplankton: Analysis and parameterization. *Journal of Geophysical Research*, 100:13321.

Bricaud, A., Morel, A., Babin, M., Allali, K., and Claustre, H. (1998). Variations of light absorption by suspended particles with chlorophyll a concentration in oceanic (case 1) waters: Analysis and implications for bio-optical models. *Journal of Geophysical Research: Oceans*, 103:31033–31044.

Bricaud, A., Morel, A., and Prieur, L. (1981). Absorption by dissolved organic matter of the sea (yellow substance) in the uv and visible domains. *Limnology and Oceanography*, 26:43–53.

Briggs, M. A., Day-Lewis, F. D., Dehkordy, F. M. P., Hampton, T., Zarnetske, J. P., Scruggs, C. R., Singha, K., Harvey, J. W., and Lane, J. W. (2018). Direct observations of hydrologic exchange occurring with less-mobile porosity and the development of anoxic microzones in sandy lakebed sediments. *Water Resources Research*, 54(7):4714–4729.

Campanelli, A., Pascucci, S., Betti, M., Grilli, F., Marini, M., Pignatti, S., and Guicciardi, S. (2017). An empirical ocean colour algorithm for estimating the contribution of coloured dissolved organic matter in north-central western adriatic sea. *Remote Sensing*, 9.

Cannizzaro, J. P. and Carder, K. L. (2006). Estimating chlorophyll a concentrations from remote-sensing reflectance in optically shallow waters. *Remote Sensing of Environment*, 101:13–24.

Cao, F., Tzortziou, M., Hu, C., Mannino, A., Fichot, C. G., Vecchio, R. D., Najjar, R. G., and Novak, M. (2018). Remote sensing retrievals of colored dissolved organic matter and dissolved organic carbon dynamics in north american estuaries and their margins. *Remote Sensing of Environment*, 205:151–165.

Carder, K. L., Chen, F. R., Lee, Z. P., Hawes, S. K., and Kamykowski, D. (1999). Semianalytic moderate-resolution imaging spectrometer algorithms for chlorophyll a and absorption with bio-optical domains based on nitrate-depletion temperatures. *Journal of Geophysical Research: Oceans*, 104:5403–5421.

Castillo, C. E. D. and Miller, R. L. (2008). On the use of ocean color remote sensing to measure the transport of dissolved organic carbon by the mississippi river plume. *Remote Sensing of Environment*, 112:836–844.

Chang, G. C. and Dickey, T. D. (2004). Coastal ocean optical influences on solar transmission and radiant heating rate. *Journal of Geophysical Research: Oceans*, 109(C1).

Chen, J., He, X., Zhou, B., and Pan, D. (2017a). Deriving colored dissolved organic matter absorption coefficient from ocean color with a neural quasi-analytical algorithm. *Journal of Geophysical Research: Oceans*, 122(11):8543–8556.

Chen, J., Zhu, W., Tian, Y. Q., Yu, Q., Zheng, Y., and Huang, L. (2017b). Remote estimation of colored dissolved organic matter and chlorophyll-a in lake huron using sentinel-2 measurements. *Journal of Applied Remote Sensing*, 11:1.

Coble, P. G. (2007). Marine optical biogeochemistry: The chemistry of ocean color. *Chemical Reviews*, 107(2):402–418.

Das, S., Das, I., Giri, S., Chanda, A., Maity, S., Lotliker, A. A., Kumar, T. S., Akhand, A., and Hazra, S. (2017). Chromophoric dissolved organic matter (cdom) variability over the continental shelf of the northern bay of bengal. *Oceanologia*, 59:271–282.

de Souza Machado, A. A., Spencer, K., Kloas, W., Toffolon, M., and Zarfl, C. (2016). Metal fate and effects in estuaries: A review and conceptual model for better understanding of toxicity. *Science of The Total Environment*, 541:268–281.

D'Sa, E. J. and DiMarco, S. F. (2009). Seasonal variability and controls on chromophoric dissolved organic matter in a large river-dominated coastal margin. *Limnology and Oceanography*, 54(6):2233–2242.

D'sa, E. J., Miller, R. L., and Castillo, C. D. (2006). Bio-optical properties and ocean color algorithms for coastal waters influenced by the mississippi river during a cold front. *Applied Optics*, 45.

Fairall, C. W., Bradley, E. F., Hare, J. E., Grachev, A. A., and Edson, J. B. (2003). Bulk parameterization of air-sea fluxes: Updates and verification for the coare algorithm. *Journal of Climate*, 16.

Fasching, C., Behounek, B., Singer, G. A., and Battin, T. J. (2014). Microbial degradation of terrigenous dissolved organic matter and potential consequences for carbon cycling in brown-water streams. *Scientific Reports*, 4.

Fichot, C. G. and Benner, R. (2012). The spectral slope coefficient of chromophoric dissolved organic matter (s275–295) as a tracer of terrigenous dissolved organic carbon in river-influenced ocean margins. *Limnology and Oceanography*, 57(5):1453–1466.

Fichot, C. G., Tzortziou, M., and Mannino, A. (2023). Remote sensing of dissolved organic carbon (doc) stocks, fluxes and transformations along the land-ocean aquatic continuum: advances, challenges, and opportunities. *Earth-Science Reviews*, 242.

Franz, B., Werdell, J., Meister, G., Bailey, S., Eplee, R., Feldman, G., Kwiatkowska, E., Mcclain, C., Patt, F., and Thomas, D. (2005). The continuity of ocean color measurements from seawifs to modis. *Proc. SPIE Int. Soc. Opt. Eng.*, 5882.

Gao, M., Zhai, P.-W., Franz, B. A., Knobelspiesse, K., Ibrahim, A., Cairns, B., Craig, S. E., Fu, G., Hasekamp, O., Hu, Y., and Werdell, P. J. (2020). Inversion of multiangular polarimetric measurements from the acepol campaign: an application of improving aerosol property and hyperspectral ocean color retrievals. *Atmospheric Measurement Techniques*, 13(7):3939–3956.

Garver, S. A. and Siegel, D. A. (1997). Inherent optical property inversion of ocean color spectra and its biogeochemical interpretation: 1. time series from the sargasso sea. *Journal of Geophysical Research: Oceans*, 102:18607–18625.

Giddings, J., Matthews, A. J., Klingaman, N. P., Heywood, K. J., Joshi, M., and Webber, B. G. (2020). The effect of seasonally and spatially varying chlorophyll on bay of bengal surface ocean properties and the south asian monsoon. *Weather and Climate Dynamics*, 1:635–655.

Gilerson, A., Gitelson, A., Zhou, J., Gurlin, D., Moses, W., Ioannou, I., and Ahmed, S. (2010). Algorithms for remote estimation of chlorophyll-a in coastal and inland waters using red and near infrared bands. *Optics Express*, 18(23):24109–24125.

Gitelson, A. A., Dall'Olmo, G., Moses, W., Rundquist, D. C., Barrow, T., Fisher, T. R., Gurlin, D., and Holz, J. (2008). A simple semi-analytical model for remote estimation of chlorophyll-a in turbid waters: Validation. *Remote Sensing of Environment*, 112(9):3582–3593.

Gnanadesikan, A. and Anderson, W. G. (2009). Ocean water clarity and the ocean general circulation in a coupled climate model. *Journal of Physical Oceanography*, 39:314–332.

Gnanadesikan, A., Kim, G. E., and Pradal, M. A. S. (2019). Impact of colored dissolved materials on the annual cycle of sea surface temperature: Potential implications for extreme ocean temperatures. *Geophysical Research Letters*, 46:861–869.

Gobler, C. J. (2020). Climate change and harmful algal blooms: Insights and perspective. *Harmful Algae*, 91:101731. Climate change and harmful algal blooms.

Gokul, E. A., Raitsos, D. E., Gittings, J. A., Alkawri, A., and Hoteit, I. (2019). Remotely sensing harmful algal blooms in the red sea. *PLoS one*, 14(4):e0215463.

Green, S. A. and Blough, N. V. (1994). Optical absorption and fluorescence properties of chromophoric dissolved organic matter in natural waters. *Limnology and Oceanography*, 39:1903–1916.

Guallar, C. and Flos, J. (2019). Linking phytoplankton primary production and chromophoric dissolved organic matter in the sea. *Progress in Oceanography*, 176:102116.

Guo, W., Stedmon, C. A., Han, Y., Wu, F., Yu, X., and Hu, M. (2007). The conservative and non-conservative behavior of chromophoric dissolved organic matter in chinese estuarine waters. *Marine Chemistry*, 107:357–366.

Helms, J. R., Stubbins, A., Ritchie, J. D., Minor, E. C., Kieber, D. J., and Mopper, K. (2008). Absorption spectral slopes and slope ratios as indicators of molecular weight, source, and photobleaching of chromophoric dissolved organic matter. *Limnology and Oceanography*, 53:955–969.

Hill, V. J. (2008). Impacts of chromophoric dissolved organic material on surface ocean heating in the chukchi sea. *Journal of Geophysical Research: Oceans*, 113(C7).

Hoge, F. E. and Lyon, P. E. (1996). Satellite retrieval of inherent optical properties by linear matrix inversion of oceanic radiance models: An analysis of model and radiance measurement errors. *Journal of Geophysical Research: Oceans*, 101:16631–16648.

Hong, B. and Shen, J. (2013). Linking dynamics of transport timescale and variations of hypoxia in the chesapeake bay. *Journal of Geophysical Research: Oceans*, 118(11):6017–6029.

Hu, C., Montgomery, E. T., Schmitt, R. W., and Muller-Karger, F. E. (2004). The dispersal of the amazon and orinoco river water in the tropical atlantic and caribbean sea: Observation from space and s-palace floats. *Deep-Sea Research Part II: Topical Studies in Oceanography*, 51:1151–1171.

IOCCG (2000). *Remote Sensing of Ocean Colour in Coastal, and Other Optically-Complex, Waters*, volume No. 3 of *Reports of the International Ocean Colour Coordinating Group*. IOCCG, Dartmouth, Canada.

IOCCG (2006). *Remote Sensing of Inherent Optical Properties: Fundamentals, Tests of Algorithms, and Applications*, volume No. 5 of *Reports of the International Ocean Colour Coordinating Group*. IOCCG, Dartmouth, Canada.

IOCCG (2020). *Synergy between Ocean Colour and Biogeochemical/Ecosystem Models*, volume No. 19 of *Reports of the International Ocean Colour Coordinating Group*. IOCCG, Dartmouth, Canada.

Jafar-Sidik, M., Gohin, F., Bowers, D., Howarth, J., and Hull, T. (2017). The relationship between suspended particulate matter and turbidity at a mooring station in a coastal environment: consequences for satellite-derived products. *Oceanologia*, 59(3):365–378.

Jerlov, N. G. (1976). *Colour of the Sea*, volume 14, pages 163–172. Elsevier.

Joshi, I. D., D'Sa, E. J., Osburn, C. L., Bianchi, T. S., Ko, D. S., Oviedo-Vargas, D., Arellano, A. R., and Ward, N. D. (2017). Assessing chromophoric dissolved organic matter (cdom) distribution, stocks, and fluxes in apalachicola bay using combined field, viirs ocean color, and model observations. *Remote Sensing of Environment*, 191:359–372.

Jutla, A. S., Akanda, A. S., and Islam, S. (2013). A framework for predicting endemic cholera using satellite derived environmental determinants. *Environmental Modelling & Software*, 47:148–158.

Kemp, W. M., Boynton, W. R., Adolf, J. E., Boesch, D. F., Boicourt, W. C., Brush, G., Cornwell, J. C., Fisher, T. R., Glibert, P. M., Hagy, J. D., Harding, L. W., Houde, E. D., Kimmel, D. G., Miller, W. D., Newell, R. I. E., Roman, M. R., Smith, E. M., and Stevenson, J. C. (2005). Eutrophication of chesapeake bay: historical trends and ecological interactions. *Marine Ecology Progress Series*, 303:1–29.

Kim, G. E., Gnanadesikan, A., Castillo, C. E. D., and Pradal, M. A. (2018). Upper ocean cooling in a coupled climate model due to light attenuation by yellowing materials. *Geophysical Research Letters*, 45:6134–6140.

Kirk, J. T. . (1994). Characteristics of the light field in highly turbid waters: A monte carlo study. *Limnology and Oceanography*, 39(3):702–706.

Klein, K. P., Lantuit, H., Heim, B., Fell, F., Doxaran, D., and Irrgang, A. M. (2019). Long-term high-resolution sediment and sea surface temperature spatial patterns in arctic nearshore waters retrieved using 30-year landsat archive imagery. *Remote Sensing*, 11(23):2791.

Kowalczuk, P. (1999). Seasonal variability of yellow substance absorption in the surface layer of the baltic sea. *Journal of Geophysical Research: Oceans*, 104(C12):30047–30058.

Kumar, S. P., Madhupratap, M., Kumar, M. D., Gauns, M., Muraleedharan, P. M., Sarma, V. V. S. S., and Souza, S. N. D. (2000). Physical control of primary productivity on a seasonal scale in central and eastern arabian sea. *Journal of Earth Science System*, 109:433–441.

Kutser, T. (2009). Passive optical remote sensing of cyanobacteria and other intense phytoplankton blooms in coastal and inland waters. *International Journal of Remote Sensing*, 30(17):4401–4425.

Lee, Z., Carder, K. L., and Arnone, R. A. (2002). Deriving inherent optical properties from water color: a multiband quasi-analytical algorithm for optically deep waters. *Applied Optics*, 41:5755–5772.

Lee, Z.-P., Du, K.-P., and Arnone, R. (2005). A model for the diffuse attenuation coefficient of downwelling irradiance. *Journal of Geophysical Research: Oceans*, 110(C2).

Lengaigne, M., Menkes, C., Aumont, O., Gorgues, T., Bopp, L., André, J. M., and Madec, G. (2007). Influence of the oceanic biology on the tropical pacific climate in a coupled general circulation model. *Climate Dynamics*, 28:503–516.

Lewis, M. R., Carr, M.-E., Feldman, G. C., Esaias, W., and McClain, C. (1990). Influence of penetrating solar radiation on the heat budget of the equatorial pacific ocean. *Nature*, 347:543.

Li, Z., Zhang, F., Shi, J., Chan, N. W., Tan, M. L., Kung, H. T., Liu, C., Cheng, C., Cai, Y., Wang, W., and Li, X. (2023). Remote sensing for chromophoric dissolved organic matter

(cdom) monitoring research 2003–2022: A bibliometric analysis based on the web of science core database. *Marine Pollution Bulletin*, 196:115653.

Loisel, H., Vantrepotte, V., Dessailly, D., and Mériaux, X. (2014). Assessment of the colored dissolved organic matter in coastal waters from ocean color remote sensing. *Optics Express*, 32:13109–13124.

Lotliker, A. A., Baliarsingh, S. K., Sahu, K. C., and Kumar, T. S. (2015). Performance of semianalytical algorithm and associated inherent optical properties in coastal waters of north western bay of bengal. *Journal of the Indian Society of Remote Sensing*, 43:143–149.

Mabit, R., Araújo, C. A., Singh, R. K., and Bélanger, S. (2022). Empirical remote sensing algorithms to retrieve spm and cdom in québec coastal waters. *Frontiers in Remote Sensing*, 3.

Manizza, M., Quéré, C. L., Watson, A. J., and Buitenhuis, E. T. (2005). Bio-optical feedbacks among phytoplankton, upper ocean physics and sea-ice in a global model. *Geophysical Research Letters*, 32:1–4.

Mannino, A., Novak, M. G., Hooker, S. B., Hyde, K., and Aurin, D. (2014). Algorithm development and validation of cdom properties for estuarine and continental shelf waters along the northeastern u.s. coast. *Remote Sensing of Environment*, 152:576–602.

Mannino, A., Russ, M. E., and Hooker, S. B. (2008). Algorithm development and validation for satellite-derived distributions of doc and cdom in the u.s. middle atlantic bight. *Journal of Geophysical Research: Oceans*, 113.

Maritorena, S. and Siegel, D. A. (2005). Consistent merging of satellite ocean color data sets using a bio-optical model. *Remote Sensing of Environment*, 94:429–440.

Maritorena, S., Siegel, D. A., and Peterson, A. R. (2002). Optimization of a semianalytical ocean color model for global-scale applications. *Applied Optics*, 41:2705–2714.

Marra, J., Langdon, C., and Knudson, C. A. (1995). Primary production, water column changes, and the demise of a phaeocystis bloom at the marine light-mixed layers site (59°n, 21°w) in the northeast atlantic ocean. *Journal of Geophysical Research*, 100:6633–6643.

Massicotte, P., Amon, R. M. W., Antoine, D., Archambault, P., Balzano, S., Bélanger, S., Benner, R., Boeuf, D., Bricaud, A., Bruyant, F., Chaillou, G., Chami, M., Charrière, B., Chen,

J., Claustre, H., Coupel, P., Delsaut, N., Doxaran, D., Ehn, J., Fichot, C., Forget, M.-H., Fu, P., Gagnon, J., Garcia, N., Gasser, B., Ghiglione, J.-F., Gorsky, G., Gosselin, M., Gourvil, P., Gratton, Y., Guillot, P., Heipieper, H. J., Heussner, S., Hooker, S. B., Huot, Y., Jeanthon, C., Jeffrey, W., Joux, F., Kawamura, K., Lansard, B., Leymarie, E., Link, H., Lovejoy, C., Marec, C., Marie, D., Martin, J., Martín, J., Massé, G., Matsuoka, A., McKague, V., Mignot, A., Miller, W. L., Miquel, J.-C., Mucci, A., Ono, K., Ortega-Retuerta, E., Panagiotopoulos, C., Papakyriakou, T., Picheral, M., Prieur, L., Raimbault, P., Ras, J., Reynolds, R. A., Rochon, A., Rontani, J.-F., Schmechtig, C., Schmidt, S., Sempéré, R., Shen, Y., Song, G., Stramski, D., Tachibana, E., Thirouard, A., Tolosa, I., Tremblay, J.-E., Vaïtilingom, M., Vaulot, D., Vaultier, F., Volkman, J. K., Xie, H., Zheng, G., and Babin, M. (2021). The malina oceanographic expedition: how do changes in ice cover, permafrost and uv radiation impact biodiversity and biogeochemical fluxes in the arctic ocean? *Earth System Science Data*, 13(4):1561–1592.

Matsuoka, A., Hooker, S. B., Bricaud, A., Gentili, B., and Babin, M. (2013). Estimating absorption coefficients of colored dissolved organic matter (cdom) using a semi-analytical algorithm for southern beaufort sea waters: Application to deriving concentrations of dissolved organic carbon from space. *Biogeosciences*, 10:917–927.

Matsuoka, A., Huot, Y., Shimada, K., Saitoh, S. I., and Babin, M. (2007). Bio-optical characteristics of the western arctic ocean: Implications for ocean color algorithms. *Canadian Journal of Remote Sensing*, 33:503–518.

Matsushita, B., Yang, W., Chang, P., Yang, F., and Fukushima, T. (2012). A simple method for distinguishing global case-1 and case-2 waters using seawifs measurements. *ISPRS journal of photogrammetry and remote sensing*, 69:74–87.

Matthews, M. W. (2011). A current review of empirical procedures of remote sensing in inland and near-coastal transitional waters. *International Journal of Remote Sensing*, 32:6855–6899.

McClain, C. R., Arrigo, K., Tai, K.-S., and Turk, D. (1996). Observations and simulations of physical and biological processes at ocean weather station p1951_1980. *Journal of Geophysical Research*, 101:3697–3614.

McKnight, D. M., Boyer, E. W., Westerhoff, P. K., Doran, P. T., Kulbe, T., and Andersen, D. T. (2001). Spectrofluorometric characterization of dissolved organic matter for indication of precursor organic material and aromaticity. *Limnology and Oceanography*, 46:38–48.

Menendez, A. and Tzortziou, M. (2024). Driving factors of colored dissolved organic matter dynamics across a complex urbanized estuary. *Science of the Total Environment*, 921.

Menon, H. B. (2004). Calibration of an optical equation to analyse the atmospheric turbidity and water quality of an estuarine environment. *Journal of the Indian Society of Remote Sensing*, 32:287–300.

Menon, H. B. and Adhikari, A. (2018). Remote sensing of chlorophyll-a in case ii waters: A novel approach with improved accuracy over widely implemented turbid water indices. *Journal of Geophysical Research: Oceans*, 123(11):8138–8158.

Menon, H. B., Lotliker, A., and Nayak, S. R. (2005). Pre-monsoon bio-optical properties in estuarine, coastal and lakshadweep waters. *Estuarine, Coastal and Shelf Science*, 63:211–223.

Menon, H. B., Sangekar, N. P., Lotliker, A. A., and Vethamony, P. (2011). Dynamics of chromophoric dissolved organic matter in mandovi and zuari estuaries - a study through in situ and satellite data. *ISPRS Journal of Photogrammetry and Remote Sensing*, 66:545–552.

Metri, S. M. and Singh, K. (2010). Study of rainfall features over goa state during southwest monsoon season. *MAUSAM*, 61:155–162.

Mobley, C. D. (2022). *The Oceanic Optics Book*. International Ocean Colour Coordinating Group (IOCCG), 1 edition.

Mobley, C. D., Stramski, D., Bissett, W. P., and Boss, E. (2004). Optical modeling of ocean waters: Is the case 1 - case 2 classification still useful? *Oceanography*, 17(2):60–67.

Moran, M. A. and Miller, W. L. (2007). Resourceful heterotrophs make the most of light in the coastal ocean. *Nature Reviews Microbiology*, 5:792–800.

Morel, A. and Antoine, D. (1994). Heating rate within the upper ocean in relation to its bio–optical state. *Journal of Physical Oceanography*, 24(7):1652–1665.

Morel, A. and Prieur, L. (1977). Analysis of variations in ocean color. *Limnology and Oceanography*, 22:709–722.

Mouw, C. B., Greb, S., Aurin, D., DiGiacomo, P. M., Lee, Z., Twardowski, M., Binding, C., Hu, C., Ma, R., Moore, T., Moses, W., and Craig, S. E. (2015). Aquatic color radiometry remote sensing of coastal and inland waters: Challenges and recommendations for future satellite missions. *Remote Sensing of Environment*, 160:15–30.

Najah, A. and Al-Shehhi, M. R. (2021). Performance of the ocean color algorithms: Qaa, gsm, and giop in inland and coastal waters. *Remote Sensing in Earth Systems Sciences*, 4:235–248.

Nechad, B., Ruddick, K., and Park, Y. (2010). Calibration and validation of a generic multi-sensor algorithm for mapping of total suspended matter in turbid waters. *Remote Sensing of Environment*, 114(4):854–866.

Nelson, N. B. and Siegel, D. A. (2013). The global distribution and dynamics of chromophoric dissolved organic matter. *Annual Review of Marine Science*, 5:447–476.

Neukermans, G., Loisel, H., Mériaux, X., Astoreca, R., and McKee, D. (2012). In situ variability of mass-specific beam attenuation and backscattering of marine particles with respect to particle size, density, and composition. *Limnology and Oceanography*, 57:124–144.

Odermatt, D., Gitelson, A., Brando, V. E., and Schaepman, M. (2012). Review of constituent retrieval in optically deep and complex waters from satellite imagery. *Remote Sensing of Environment*, 118:116–126.

Ohlmann, J. C. (2003). Ocean radiant heating in climate models. *Journal of Climate*, 16:1337–1351.

Ohlmann, J. C., Siegel, D. A., and Mobley, C. D. (2000). Ocean radiant heating. part i: Optical influences. *Journal of Physical Oceanography*, pages 1833–1848.

Pahlevan, N., Smith, B., Binding, C., Gurlin, D., Li, L., Bresciani, M., and Giardino, C. (2021). Hyperspectral retrievals of phytoplankton absorption and chlorophyll-a in inland and nearshore coastal waters. *Remote Sensing of Environment*, 253:112200.

Palacios, S. L., Peterson, T. D., and Kudela, R. M. (2009). Development of synthetic salinity from remote sensing for the columbia river plume. *Journal of Geophysical Research: Oceans*, 114.

Parida, C., Lotliker, A. A., Roy, R., and Vinayachandran, P. N. (2022). Radiant heating rate associated with chlorophyll dynamics in upper ocean of southern bay of bengal: A case study during bay of bengal boundary layer experiment. *Deep-Sea Research Part II: Topical Studies in Oceanography*, 196.

Pednekar, S. M., Matondkar, S. G. P., and Kerkar, V. (2012). Spatiotemporal distribution of harmful algal flora in the tropical estuarine complex of goa, india. *The Scientific World Journal*, 2012:596276.

Pérez, G. L., Galí, M., Royer, S.-J., Sarmento, H., Gasol, J. M., Marrasé, C., and Simó, R. (2016). Bio-optical characterization of offshore nw mediterranean waters: Cdom contribution to the absorption budget and diffuse attenuation of downwelling irradiance. *Deep Sea Research Part I: Oceanographic Research Papers*, 114:111–127.

Piccini, C., Conde, D., Pernthaler, J., and Sommaruga, R. (2009). Alteration of chromophoric dissolved organic matter by solar uv radiation causes rapid changes in bacterial community composition. *Photochemical and Photobiological Sciences*, 8:1321–1328.

Pope, R. M. and Fry, E. S. (1997). Absorption spectrum 380-700 nm of pure water. ii. integrating cavity measurements. *Applied Optics*, 36:8710–8723.

Pradhan, Y., Mohan, M., Sengupta, D., and Nayak, S. (2005). Radiant heating rates and surface biology during the arabian sea monsoon experiment. *Journal of Geophysics and Engineering*, 2:16–22.

Qasim, S. and Sen Gupta, R. (1981). Environmental characteristics of the mandovi-zuari estuarine system in goa. *Estuarine, Coastal and Shelf Science*, 13(5):557–578.

Reddy, S. K. K., Gupta, H., and Reddy, D. V. (2019). Dissolved inorganic carbon export by mountainous tropical rivers of the western ghats, india. *Chemical Geology*, 530.

Rochelle-Newall, E. J. and Fisher, T. R. (2002). Chromophoric dissolved organic matter and dissolved organic carbon in chesapeake bay. *Marine Chemistry*, 77:23.

Roesler, C. S., Perry, M. J., and Carder, K. L. (1989). Modeling in situ phytoplankton absorption from total absorption spectra in productive inland marine waters. *Limnology and Oceanography*, 34:1510–1523.

Ruddick, K. G., De Cauwer, V., Park, Y.-J., and Moore, G. (2006). Seaborne measurements of near infrared water-leaving reflectance: The similarity spectrum for turbid waters. *Limnology and Oceanography*, 51(2):1167–1179.

Ruescas, A. B., Hieronymi, M., Mateo-Garcia, G., Koponen, S., Kallio, K., and Camps-Valls, G. (2018). Machine learning regression approaches for colored dissolved organic matter (cdom) retrieval with s2-msi and s3-olci simulated data. *Remote Sensing*, 10:786.

Sathyendranath, S., Brewin, R. J., Brockmann, C., Brotas, V., Calton, B., Chuprin, A., Cipollini, P., Couto, A. B., Dingle, J., Doerffer, R., Donlon, C., Dowell, M., Farman, A., Grant, M.,

Groom, S., Horseman, A., Jackson, T., Krasemann, H., Lavender, S., Martinez-Vicente, V., Mazeran, C., Mélin, F., Moore, T. S., Müller, D., Regner, P., Roy, S., Steele, C. J., Steinmetz, F., Swinton, J., Taberner, M., Thompson, A., Valente, A., Zühlke, M., Brando, V. E., Feng, H., Feldman, G., Franz, B. A., Frouin, R., Gould, R. W., Hooker, S. B., Kahru, M., Kratzer, S., Mitchell, B. G., Muller-Karger, F. E., Sosik, H. M., Voss, K. J., Werdell, J., and Platt, T. (2019). An ocean-colour time series for use in climate studies: The experience of the ocean-colour climate change initiative (oc-cci). *Sensors*, 19(19).

Sathyendranath, S., Brewin, R. J., Jackson, T., Mélin, F., and Platt, T. (2017). Ocean-colour products for climate-change studies: What are their ideal characteristics? *Remote Sensing of Environment*, 203:125–138. Earth Observation of Essential Climate Variables.

Schaeffer, B. A., Sinclair, G. A., Lehrter, J. C., Murrell, M. C., Kurtz, J. C., Gould, R. W., and Yates, D. F. (2011). An analysis of diffuse light attenuation in the northern gulf of mexico hypoxic zone using the seawifs satellite data record. *Remote Sensing of Environment*, 115:3748–3757.

Senesi, N., Miano, T., Provenzano, M., and Brunetti, G. (1989). Spectroscopic and compositional comparative characterization of i.h.s.s. reference and standard fulvic and humic acids of various origin. *The Science of the Total Environment*, 81:143–156.

Shanmugam, P., Varunan, T., Jaiganesh, S. N. N., Sahay, A., and Chauhan, P. (2016). Optical assessment of colored dissolved organic matter and its related parameters in dynamic coastal water systems. *Estuarine, Coastal and Shelf Science*, 175:126–145.

Sharp, J. H., Yoshiyama, K., Parker, A. E., Schwartz, M. C., Curless, S. E., Beauregard, A. Y., Ossolinski, J. E., and Davis, A. R. (2009). A biogeochemical view of estuarine eutrophication: Seasonal and spatial trends and correlations in the delaware estuary. *Estuaries and Coasts*, 32:1023–1043.

Sheskin, D. J. (2020). *Handbook of Parametric and Nonparametric Statistical Procedures*. Chapman and Hall/CRC, 5 edition.

Shetye, S. R., Gouveia, A. D., Singbal, S. Y., Naik, C. G., Sundar, D., Michael, G. S., and Nampoothiri, G. (1995). Propagation of tides in the mandovi-zuari estuarine network. 104:667–682.

Shetye, S. R., Shankar, D., Neetu, S., Suprit, K., Michael, G. S., and Chandramohan, P. (2007). *The environment that conditions the Mandovi and Zuari estuaries*, pages 3–27. National Institute of Oceanography.

Shi, W. and Wang, M. (2010). Characterization of global ocean turbidity from moderate resolution imaging spectroradiometer ocean color observations. *Journal of Geophysical Research: Oceans*, 115:C11022.

Siegel, D. A., Ohlmann, J. C., Washburn, L., Bidigare, R. R., Nosse, C. T., Fields, E., and Zhou, Y. (1995). Solar radiation, phytoplankton pigments and the radiant heating of the equatorial pacific warm pool. *Journal of Geophysical Research*, 100:4885–4891.

Smith, R. C. and Baker, K. S. (1981). Optical properties of the clearest natural waters (200-800 nm). *Applied Optics*, 20:177–184.

Sonak, S., Patil, K., and Devi, P. (2018). Causes, human health impacts and control of harmful algal blooms: A comprehensive review. *Environmental Pollution and Protection*, 3:40–55.

Soppa, M. A., Pefanis, V., Hellmann, S., Losa, S. N., Hölemann, J., Martynov, F., Heim, B., Janout, M. A., Dinter, T., Rozanov, V., and Bracher, A. (2019). Assessing the influence of water constituents on the radiative heating of laptev sea shelf waters. *Frontiers in Marine Science*, 6.

Spencer, R. G., Bolton, L., and Baker, A. (2007). Freeze/thaw and ph effects on freshwater dissolved organic matter fluorescence and absorbance properties from a number of uk locations. *Water Research*, 41(13):2941–2950.

Stedmon, C., Markager, S., and Kaas, H. (2000). Optical properties and signatures of chromophoric dissolved organic matter (cdom) in danish coastal waters. *Estuarine, Coastal and Shelf Science*, 51(2):267–278.

Stedmon, C. A. and Markager, S. (2005). Tracing the production and degradation of autochthonous fractions of dissolved organic matter by fluorescence analysis. *Limnology and Oceanography*, 50(5):1415–1426.

Stramski, D., Reynolds, R. A., Kahru, M., and Mitchell, B. G. (1999). Estimation of particulate organic carbon in the ocean from satellite remote sensing. *Science*, 285(5425):239–242.

Strutton, P. G. and Chavez, F. P. (2004). Biological heating in the equatorial pacific: Observed variability and potential for real-time calculation. *Journal of Climate*, 17:1097.

Sun, X., Zhang, Y., Zhang, Y., Shi, K., Zhou, Y., and Li, N. (2021). Machine learning algorithms for chromophoric dissolved organic matter (cdom) estimation based on landsat 8 images. *Remote Sensing*, 13:3560.

Suzuki, R. and Ishimaru, T. (1990). An improved method for the determination of phytoplankton chlorophyll using n, n-dimethylformamide*. *Journal of the Oceanographical Society of Japan*, 46:190–194.

Tedetti, M. and Sempéré, R. (2006). Penetration of ultraviolet radiation in the marine environment. a review. *Photochemistry and Photobiology*, 82(2):389–397.

Tehrani, N. C., D'Sa, E. J., Osburn, C. L., Bianchi, T. S., and Schaeffer, B. A. (2013). Chromophoric dissolved organic matter and dissolved organic carbon from sea-viewing wide field-of-view sensor (seawifs), moderate resolution imaging spectroradiometer (modis) and meris sensors: Case study for the northern gulf of mexico. *Remote Sensing*, 5:1439–1464.

Tiwari, S. P. and Shanmugam, P. (2011). An optical model for the remote sensing of coloured dissolved organic matter in coastal/ocean waters. *Estuarine, Coastal and Shelf Science*, 93:396–402.

Topp, S. N., Pavelsky, T. M., Jensen, D., Simard, M., and Ross, M. R. (2020). Research trends in the use of remote sensing for inland water quality science: Moving towards multidisciplinary applications. *Water (Switzerland)*, 12:169.

Turner, A. G., Joshi, M., Robertson, E. S., and Woolnough, S. J. (2012). The effect of arabian sea optical properties on sst biases and the south asian summer monsoon in a coupled gcm. *Climate Dynamics*, 39:811–826.

Twardowski, M. S., Boss, E., Sullivan, J. M., and Donaghay, P. L. (2004). Modeling the spectral shape of absorption by chromophoric dissolved organic matter. *Marine Chemistry*, 89:69–88.

Twardowski, M. S., Claustre, H., Freeman, S. A., Stramski, D., and Huot, Y. (2007). Optical backscattering properties of the "clearest" natural waters. *Biogeosciences*, 4(6):1041–1058.

Tzortziou, M., Neale, P. J., Megonigal, J. P., Pow, C. L., and Butterworth, M. (2011). Spatial gradients in dissolved carbon due to tidal marsh outwelling into a chesapeake bay estuary. *Marine Ecology Progress Series*, 426:41–56.

Tzortziou, M., Neale, P. J., Osburn, C. L., Megonigal, J. P., Maie, N., and Jaffé, R. (2008). Tidal marshes as a source of optically and chemically distinctive colored dissolved organic matter in the chesapeake bay. *Limnology and Oceanography*, 53:148–159.

Uudeberg, K., Ansko, I., Põru, G., Ansper, A., and Reinart, A. (2019). Using optical water types to monitor changes in optically complex inland and coastal waters. *Remote Sensing*, 11.

Valente, A., Sathyendranath, S., Brotas, V., Groom, S., Grant, M., Taberner, M., Antoine, D., Arnone, R., Balch, W. M., Barker, K., Barlow, R., Bélanger, S., Berthon, J.-F., Beşiktepe, Ş., Brando, V., Canuti, E., Chavez, F., Claustre, H., Crout, R., Frouin, R., García-Soto, C., Gibb, S. W., Gould, R., Hooker, S., Kahru, M., Klein, H., Kratzer, S., Loisel, H., McKee, D., Mitchell, B. G., Moisan, T., Muller-Karger, F., O'Dowd, L., Ondrusek, M., Poulton, A. J., Repecaud, M., Smyth, T., Sosik, H. M., Twardowski, M., Voss, K., Werdell, J., Wernand, M., and Zibordi, G. (2016). A compilation of global bio-optical in situ data for ocean-colour satellite applications. *Earth System Science Data*, 8(1):235–252.

Vecchio, R. D. and Subramaniam, A. (2004). Influence of the amazon river on the surface optical properties of the western tropical north atlantic ocean. *Journal of Geophysical Research: Oceans*, 109.

Vijith, V., Shetye, S., Baetens, K., Luyten, P., and Michael, G. (2016). Residual estuarine circulation in the mandovi, a monsoonal estuary: A three-dimensional model study. *Estuarine, Coastal and Shelf Science*, 173:79–92.

Vijith, V., Sundar, D., and Shetye, S. (2009). Time-dependence of salinity in monsoonal estuaries. *Estuarine, Coastal and Shelf Science*, 85(4):601–608.

Volta, C., Ho, D. T., Maher, D. T., Wanninkhof, R., Friederich, G., Castillo, C. D., and Dulai, H. (2020). Seasonal variations in dissolved carbon inventory and fluxes in a mangrove-dominated estuary. *Global Biogeochemical Cycles*, 34(12):e2019GB006515.

Wane, M., Lyzenga, D. R., and Klemas, V. V. (1996). Measurement of optical properties in the delaware estuary. *Journal of Coastal Research*, 12:211–228.

Werdell, P. J. and Bailey, S. W. (2005). An improved in-situ bio-optical data set for ocean color algorithm development and satellite data product validation. *Remote Sensing of Environment*, 98:122–140.

Werdell, P. J., McKinna, L. I., Boss, E., Ackleson, S. G., Craig, S. E., Gregg, W. W., Lee, Z., Maritorena, S., Roesler, C. S., Rousseaux, C. S., Stramski, D., Sullivan, J. M., Twardowski, M. S., Tzortziou, M., and Zhang, X. (2018). An overview of approaches and challenges for retrieving marine inherent optical properties from ocean color remote sensing. *Progress in Oceanography*, 160:186–212.

Zaneveld, J. R. V., Kitchen, J. C., and Pak, H. (1981). The influence of optical water type on the heating rate of a constant depth mixed layer. *Journal of Geophysical Research: Oceans*, 86(C7):6426–6428.

Zhao, J., Cao, W., Wang, G., Yang, D., Yang, Y., Sun, Z., Zhou, W., and Liang, S. (2009). The variations in optical properties of cdom throughout an algal bloom event. *Estuarine, Coastal and Shelf Science*, 82:225–232.

Zhao, J., Cao, W., Xu, Z., Ai, B., Yang, Y., Jin, G., Wang, G., Zhou, W., Chen, Y., Chen, H., and Sun, Z. (2018). Estimating cdom concentration in highly turbid estuarine coastal waters. *Journal of Geophysical Research: Oceans*, 123:5856–5873.